



UNIVERSITÀ DI PISA

Dipartimento di Fisica *E. Fermi*
Corso di Laurea Magistrale in Fisica

TESI DI LAUREA MAGISTRALE IN FISICA

Performance study of the SVD detector of Belle II and future upgrades

CANDIDATO
Ludovico Massaccesi

RELATORE
Prof. Francesco Forti

Anno Accademico 2020/2021

Abstract

SuperKEKB is a B factory: an asymmetric e^+e^- collider designed to operate at a centre-of-mass energy of 10.58 GeV, corresponding to the peak of the $\Upsilon(4S)$ vector meson resonance, which decays to a $B\bar{B}$ pair over 96% of the times. The asymmetry between the beam energies (7 GeV for e^- , 4 GeV for e^+) results in a boosted centre of mass in the laboratory frame, necessary to study time-dependent phenomena, such as certain CP asymmetries and decay rates.

Belle II is a general-purpose particle detector located at the interaction point of SuperKEKB and managed by an international collaboration; while its predecessors (BaBar and Belle) focused mainly on the CP violation in the B system, Belle II will also concentrate on the precision measurement of the decays of bottom and charmed mesons, and τ leptons, and on the search for rare or forbidden processes that may provide evidence of effects of physics beyond the Standard Model. Belle II is expected to collect 50 ab^{-1} , about 50 times more than BaBar and Belle, in several years of operation, allowing to enhance the precision of Standard Model parameters measurements, and to improve the sensitivity to possible effects from New Physics.

The Vertex Detector (VXD), which is the innermost part of Belle II, is designed specifically to accurately reconstruct the four-momenta and vertices of all the charged particles in the event. It is made of two subdetectors: the PiXel Detector (PXD), with DEPFET-technology sensors in the two innermost layers, and the Silicon Vertex Detector (SVD), with double-sided silicon strip sensors in the four outermost layers.

This thesis presents a study of the radiation damage in the SVD sensors, and discusses a possible upgraded detector, based on monolithic CMOS pixel sensors, for operation at high luminosity, on which physics benchmarking of some key channels has been performed.

SVD silicon sensors can be damaged in different ways by the radiation field generated by SuperKEKB: the bulk displacement damage can alter the effective doping concentration, changing the depletion voltage, and can also increase the bulk-generated leakage current, which contributes to the noise; surface damage can lead to larger sensor capacitance and surface-generated leakage current, both resulting in increased noise.

Algorithms to consistently monitor changes of these parameters in all of the sensors were developed; in order to study their evolution with increasing radiation damage, a method to estimate the dose in the sensors was also developed, exploiting the good correlation between SVD data and dose rates in dedicated diamond radiation sensors, which are located close to the innermost SVD sensors. SVD sensor occupancy can provide an accurate measurement of the dose by using the average deposited energy per hit (a parameter than can be easily estimated from data); however, the occupancy measurement is only possible when SVD data is being recorded, which is not always the case (for instance, data is not recorded during beam injection), leading to undetected dose. To account for the situations where SVD is exposed to radiation but not recording data,

the measurements from the diamond sensors, which are always active and recording, were used: these sensor measurements show a good correlation with SVD occupancy. Several sources of bias were studied; the largest one, introduced by the trigger, was removed thanks to the introduction, in March 2021, of a new random trigger line: this resulted in an estimate smaller by a factor ~ 3 with respect to the one from the previous study, based on the same premises. An accurate measurement of the absorbed dose is necessary to compare the observed changes in sensor parameters to the expectations, and to extrapolate the effects of radiation damage in the future; this, in turn, is needed to plan detector operations and upgrades.

An upgrade of the VXD is under study, with the goal of improving detector performance while maintaining robust operation as SuperKEKB increases its luminosity and, consequently, its backgrounds and radiation: although the presently expected background level at design luminosity is acceptable, higher safety margins would be desirable to account for the large uncertainty on these extrapolations. This thesis focuses on one of the proposals, which consists in the replacement of the whole VXD with a new vertex detector, VTX, made of five layers of Depleted Monolithic Active Pixel Sensors (DMAPS) based on a commercial CMOS technology. The all-pixel design with smaller pixels, together with the reduced material budget due to on-sensor readout electronics, should improve the detector resolution; the smaller sensor element area and short integration time should improve background tolerance by reducing the average occupancy; the possibility to implement on-chip sparsification should reduce the necessary readout bandwidth and, together with the fact that a single type of sensor is used, simplify integration and operations.

This thesis presents a benchmark study of the projected VTX performance, aimed at detector layout optimisation. A Monte Carlo simulation of $B^0 \rightarrow D^* \mu \nu \rightarrow (D^0 \pi) \mu \nu$ events, with the D^0 decaying either $\rightarrow K \pi$ or $\rightarrow K \pi \pi \pi$ and complete of beam-induced background, is performed both with the current VXD and with VTX; thanks to the Belle II Analysis Software Framework (BASF2), an accurate, not parametrised simulation of the events and of the detector response is possible. From the reconstruction of the simulated events, which is performed as it would be on experimental data, key detector parameters, which impact the results of physics analyses, are extracted: track finding efficiency, impact parameter resolution, event reconstruction efficiency, vertex position resolution, and flight length resolution. The comparison of VXD and VTX results shows that VTX would improve track finding efficiency by $\sim 10\%$, with a large improvement for tracks with low transverse momentum (under $100 \text{ MeV}/c$); this results in a B^0 reconstruction efficiency (for the selected channel) improved by up to $\sim 70\%$. Also, the resolution of impact parameters, vertex position and D^0 flight length is improved by $\sim 20\%$.

A good flight length resolution is a key element for analyses of time-dependent phenomena, such as neutral meson mixing and CP violation; also, the impact parameters and vertex resolution is instrumental for the rejection of background tracks. For these reasons, VTX can be expected to have a substantial positive impact on analyses results.

Contents

| | |
|---|-----------|
| Abstract | i |
| Introduction | v |
| 1 Physics at Belle II | 1 |
| 1.1 The Standard Model | 1 |
| 1.2 Belle II physics program | 7 |
| 2 SuperKEKB and Belle II | 10 |
| 2.1 B-factory experiments | 10 |
| 2.2 The SuperKEKB accelerator | 11 |
| 2.2.1 Beam-induced background | 13 |
| 2.3 The Belle II detector | 17 |
| 2.3.1 PXD | 18 |
| 2.3.2 SVD | 21 |
| 2.3.3 CDC | 21 |
| 2.3.4 TOP | 22 |
| 2.3.5 ARICH | 23 |
| 2.3.6 ECL | 24 |
| 2.3.7 KLM | 25 |
| 2.3.8 Trigger system | 27 |
| 2.3.9 Software framework | 29 |
| 3 SVD and future upgrades | 30 |
| 3.1 Detailed description of SVD | 30 |
| 3.1.1 Sensors | 31 |
| 3.1.2 Geometry and layout | 35 |
| 3.1.3 Diamond radiation detectors and beam-abort system | 35 |
| 3.1.4 Environmental monitoring | 36 |
| 3.2 Proposed VXD upgrade: VTX | 37 |
| 3.2.1 The upgraded sensors | 38 |
| 3.2.2 The proposed layouts | 39 |
| 3.3 VXD and VTX simulation | 39 |
| 3.4 Tracking with VXD and VTX | 42 |
| 4 Radiation damage in SVD | 45 |
| 4.1 Radiation damage in semiconductor detectors | 45 |
| 4.1.1 Bulk damage mechanisms | 45 |
| 4.1.2 Surface damage mechanisms | 48 |

| | | |
|----------|---|-----------|
| 4.1.3 | Radiation damage in SVD | 49 |
| 4.2 | Estimating the dose in SVD | 49 |
| 4.2.1 | Dose estimate from data using cluster charge | 50 |
| 4.2.2 | Correlation between dose and occupancy in SVD | 52 |
| 4.2.3 | SVD dose estimate from diamond dose | 53 |
| 4.2.4 | Results | 56 |
| 4.3 | Radiation damage effects on SVD | 59 |
| 4.3.1 | Depletion voltage | 59 |
| 4.3.2 | Noise | 61 |
| 4.3.3 | Leakage current | 63 |
| 4.4 | Background effects outlook | 67 |
| 5 | Upgrade benchmark study | 69 |
| 5.1 | Channel choice and characteristics | 69 |
| 5.2 | Event generation and simulation | 71 |
| 5.3 | Event reconstruction | 71 |
| 5.4 | Results | 74 |
| 5.4.1 | Tracking efficiency | 75 |
| 5.4.2 | Reconstruction efficiency | 76 |
| 5.4.3 | Impact parameters resolution | 77 |
| 5.4.4 | Vertex and flight length resolution | 81 |
| 6 | Conclusions | 84 |
| | Bibliography | 86 |

Introduction

Although the Standard Model of particle physics (SM) is able to predict the interactions between particles with great precision, and is supported by a tremendous body of experimental evidence, it cannot be regarded as a complete theory, as it does not provide the answer to many fundamental questions. Even if the Higgs mass-generating mechanism is well understood, the fermion masses remain free parameters of the model, and the reason behind their observed hierarchy is unknown. Moreover, the observation of neutrino oscillations proved that they have non-zero masses, but it is not clear whether the Higgs mechanism can account for them; even if it could, it does not provide a reason for their tiny scale. The matter-antimatter asymmetry observed in the universe, i.e. the tiny amount of antimatter found with respect to the amount of matter, could be explained by CP violation; however, the SM introduces, through the single phase of the CKM matrix, an amount of CP violation that is insufficient to explain the cosmological asymmetry, which therefore requires an explanation beyond the SM. Also, astrophysical observations of galaxies and other structures in the universe require the presence of additional gravitational attraction, which must be provided by “invisible” massive particles with minimal interactions with ordinary matter, referred to as dark matter; as none of these particles was observed yet, they are not present in the framework of the SM. Finally, the SM does not include any description of gravity.

Besides the lack of answers for these fundamental questions, several discrepancies or tensions between SM predictions and experimental results have been observed, which may be evidence of New Physics (NP). It is therefore considered likely that the SM is actually a low-energy approximation of a more fundamental theory.

Belle II is a next-generation B-factory experiment. B factories are asymmetric electron-positron colliders designed to produce $B\bar{B}$ pairs: this is achieved by tuning the collision energy to the peak of the $\Upsilon(4S)$ resonance, which almost always decays to a $B\bar{B}$ pair. The asymmetry between the beam energies allows the collision centre of mass to be boosted in the laboratory frame, which is necessary to study time-dependent phenomena. Belle II works at the intensity frontier, with the main goals of searching for NP in the flavour sector, and improving precision measurements of SM parameters. The Belle II research program, following up and expanding those of the previous B-factory experiments (Belle and BaBar), will be in competition with and complementary to that of the LHCb experiment. The Belle II data taking began in March 2019.

Reconstructing charged particle tracks with high efficiency, and decay vertices with good resolution, is a key element of physics analyses. The Belle II vertex detector (VXD), made of the innermost pixel detector (PXD) and the outermost silicon vertex detector (SVD), is designed specifically for these tasks. This thesis presents a study of the damage that SVD undergoes due to the radiation field of the SuperKEKB collider, and the development of the tools required to reliably monitor the dose. Although sensor radiation damage is not expected to cause significant performance deterioration, high luminosity

operation of the accelerator will significantly increase occupancy, making the operation of the current detector marginal. Therefore, an upgrade of the VXD is under study, with the goal of improving detector performance while maintaining robust operation as SuperKEKB increases its luminosity and, consequently, its backgrounds: although the presently expected background level at design luminosity is acceptable, higher safety margins would be desirable to account for the large uncertainty on these extrapolations. This thesis focuses on one of the proposals, which consists in the replacement of the whole VXD with a new vertex detector, VTX, made of five layers of Depleted Monolithic Active Pixel Sensors (DMAPS) based on a commercial CMOS technology. The all-pixel design with smaller pixels, together with the reduced material budget due to on-sensor readout electronics, should improve the detector resolution; the smaller sensor element area and short integration time should improve background tolerance by reducing the average occupancy; the possibility to implement on-chip sparsification should reduce the necessary readout bandwidth and, together with the fact that a single type of sensor is used, simplify integration and operations. This thesis presents a benchmark study of the projected VTX performance, aimed at detector layout optimisation.

Chapter 1 describes the particle physics context in which Belle II takes place: the SM and its shortcomings are briefly introduced, and the physics research program of Belle II is outlined.

Chapter 2 introduces the experiment itself. First the SuperKEKB collider, in which Belle II is located, is described, with a particular focus on its beam-induced backgrounds. Then, an overview of the Belle II detector is provided; some space is given to the trigger system and the software framework as well, as they play a key role throughout the thesis work.

Chapter 3 provides a more in-depth description of the SVD, and also introduces the “VTX” upgrade proposal for the vertex detector. An accurate simulation of the detector is of fundamental importance for the comparison of theoretical predictions and experimental results, but also for the optimization of upgrade designs: the Belle II software framework has a dedicated section for this, which is outlined in this chapter with particular focus on the SVD and VTX. Finally, the VTX design brings major changes to the track finding and reconstruction algorithm, hence a brief summary of them is given.

Chapter 4 presents a study of the radiation damage that SVD undergoes and its possible impact on detector performance. The radiation field of SuperKEKB can damage silicon detectors in different ways, that are described in the chapter, with particular focus on the effects that are expected to have the largest impact on SVD sensors. A method for estimating the dose absorbed by SVD is presented: the dose cannot be estimated from detector data because SuperKEKB may be active without the data being recorded, hence the measurements from dedicated, continuously-recording radiation sensors must be used; several sources of bias have been studied and addressed, and are presented in the text. Tools for automatically monitoring these biases in the future have been developed. Also, tools to consistently monitor changes in radiation-sensitive parameters of the SVD sensors, which may have an impact on performance, have been developed. The evolution of these parameters with increasing doses is presented; such a study allows to extrapolate the effects of radiation damage in the future, which is fundamental for planning detector operations and upgrades.

Chapter 5 presents a study of the projected performance of VTX, compared to that of the VXD. This benchmark is performed by simulating $B^0 \rightarrow (D^0\pi)_{D^*}\mu\nu$ events, with $D^0 \rightarrow K\pi, K\pi\pi\pi$, which are used in several analyses of the charm research program

(e.g. D^0 lifetime measurements). The events, complete of beam-induced background, are simulated in and reconstructed by the two detectors, the VXD and VTX: a description of these procedures is given in the text. By comparing the reconstructed candidates with the particles produced by the Monte Carlo simulation, key variables for the detector performance are measured: track reconstruction efficiency, impact parameters resolution, B^0 reconstruction efficiency, D^0 vertices position and flight length resolution. A comparison between VXD and VTX is presented, providing information on the improvements that can be expected from the upgrade.

spin and follow the Bose-Einstein statistics. In the SM, the fundamental matter fields are made of fermions, which are divided in quarks and leptons and grouped in three generations; each generation includes a doublet of particles. The interactions between the fermions are mediated by vector (spin-1) gauge bosons, while the scalar (spin-0) Higgs boson is introduced to explain the origin of the masses of the particles.

Fermions Before describing fermions and their interaction, it is important to note that fermion fields can be divided in two orthogonal components with opposite *chirality*, called the left-handed and right-handed components. These names come from the fact that, for massless particles, chirality eigenstates coincide with helicity eigenstates (i.e. states with defined spin along the momentum direction); for massive particles, however, chirality eigenstates are a linear combination of helicity eigenstates, and only coincide with these at first-order ultrarelativistic approximation. The importance of chirality lies in the fact that only left-handed states are sensitive to the weak interaction; the electromagnetic and strong interactions, instead, completely ignore chirality.

Leptons are sensitive to electromagnetic and weak interactions; each generation is a doublet made of a charged lepton (e, μ, τ), with charge $-e$, and a neutral lepton or neutrino. Because of their neutrality, neutrinos can only interact weakly and, consequently, right-handed neutrinos cannot interact at all (their existence itself is questioned). A lepton family number $L_{e,\mu,\tau}$ is associated to each generation: this quantum number, and consequently the leptonic flavour, is conserved by all interactions; however, the mass eigenstates of neutrinos are not flavour eigenstates, thus allowing neutrino mixing (i.e. change of flavour during propagation) and, therefore, lepton flavour violation (LFV). Each lepton has an associated anti-lepton with the same mass and opposite quantum numbers.

Quarks are sensitive to electromagnetic, weak and strong interactions; each generation is a doublet made of an up-type quark (u, c, t), with charge $+\frac{2}{3}e$, and a down-type quark (d, s, b), with charge $-\frac{1}{3}e$. Each of the six quarks has its own flavour, a quantum number which is conserved by all but weak interactions. Each quark has an associated anti-quark with the same mass and opposite quantum numbers. Quarks also have an additional quantum number called colour, which is connected to strong interaction. Unlike leptons, it is not possible to observe isolated quarks: this is due to the phenomenon of confinement, which can be derived from the theory of strong interactions, and implies that only colour singlets can be observed. The simplest and most common colour singlets are mesons (made of a quark and an anti-quark) and baryons (made of three quarks).

A mass hierarchy is present amongst fermions, and is reflected by the organization in generations.

Bosons As already mentioned, the vector bosons are responsible of the interactions between fermions; in particular:

- the photon γ is the massless mediator of electromagnetic interactions;
- the W^\pm bosons are the massive mediators of charged current (CC) weak interactions;
- the Z^0 boson is the massive mediator of neutral current (NC) weak interactions;
- the eight gluons g are the massless mediators of strong interactions.

The scalar Higgs boson, instead, is not an interaction mediator, but is responsible of the mass-generating mechanism, as explained in the following paragraphs.

Gauge theory The SM is a quantum gauge theory based on the gauge group $SU(3)_C \otimes SU(2)_L \otimes U(1)_Y$, where C indicates the colour, L the left chiral component, and Y the hypercharge.

The $SU(3)_C$ gauge group comes from the description of strong interactions by quantum chromodynamics (QCD), which introduces the vector boson field of gluons G_μ^A , where $A = 1, \dots, 8$.

The $SU(2)_L \otimes U(1)_Y$ gauge group comes from the unified description of electromagnetic and weak interactions by the electroweak (EW) theory; this introduces the vector boson fields B_μ , related to $U(1)_Y$, and W_μ^α , where $\alpha = 1, 2, 3$, related to $SU(2)_L$. With spontaneous symmetry breaking $SU(2)_L \otimes U(1)_Y \rightarrow U(1)_{EM}$, and, after diagonalising the mass terms, the fields of the photon, A_μ , and of the weak interaction bosons, W_μ^\pm and Z_μ , become explicit. While the W_μ^\pm and Z_μ fields have explicit mass terms, the A_μ field does not due to the residual $U(1)_{EM}$ symmetry.

The spontaneous breaking of the gauge symmetry is made possible by the introduction of the Higgs doublet ϕ , which induces a potential $V(\phi^\dagger\phi)$ with a ground state that is not invariant under the symmetry. This is called the Higgs mechanism, and also allows to explain the masses of the fermions as originating from interactions with the Higgs field.

Lagrangian The SM Lagrangian can be divided in five different terms [2].

$$\mathcal{L} = \mathcal{L}_{\text{kin}} + \mathcal{L}_{\text{EW}} + \mathcal{L}_{\text{QCD}} + \mathcal{L}_{\text{H}} + \mathcal{L}_{\text{Yuk}}$$

\mathcal{L}_{kin} is the kinetic term of the gauge bosons, and also includes the self-interaction terms of the weak and strong interaction bosons; the kinetic term of the fermions, instead, is included within the couplings.

$$\mathcal{L}_{\text{kin}} = -\frac{1}{4}B_{\mu\nu}B^{\mu\nu} - \frac{1}{8}W_{\mu\nu}^\alpha W^{\mu\nu}_\alpha - \frac{1}{2}G_{\mu\nu}^A G^{\mu\nu}_A$$

\mathcal{L}_{EW} includes the kinetic term of the fermions ($i\partial_\mu$) and the electroweak terms of $U(1)_Y$ (with its field, B_μ , and its generator, the weak hypercharge Y_W) and $SU(2)_L$ (with its fields, W_μ^α , and its generators, the Pauli matrices τ^α). The index f loops over all of the fermions. The coupling constants g' and g are associated with B_μ and W_μ^α , respectively.

$$\mathcal{L}_{\text{EW}} = \bar{\psi}_f \gamma^\mu \left(i\partial_\mu - \frac{1}{2}g'Y_W B_\mu - \frac{1}{2}g\tau_\alpha W_\mu^\alpha \right) \psi_f$$

\mathcal{L}_{QCD} is the quark-gluon interaction term, where g_S is the strong coupling constant, f loops over the six quarks and i, j are the colour indices.

$$\mathcal{L}_{\text{QCD}} = -\bar{\psi}_{f,i} \gamma^\mu g_S G_\mu^A T_{A,ij} \psi_{f,j}$$

\mathcal{L}_{H} includes the the kinetic term of the Higgs boson, its interactions with the electroweak gauge bosons, and, through its potential $V(\phi^\dagger\phi)$, its mass term and self-interaction. Y_ϕ is the weak hypercharge of the ϕ field, and v is its vacuum expectation

value.

$$\mathcal{L}_H = \frac{1}{2} \left| \left(\partial_\mu - \frac{1}{2} g' Y_\phi B_\mu - \frac{1}{2} g \tau_\alpha W_\mu^\alpha \right) \phi \right|^2 - V(\phi^\dagger \phi)$$

$$V(\phi^\dagger \phi) = \frac{m_h^2}{2v^2} \left(\phi^\dagger \phi - \frac{v^2}{2} \right)^2$$

\mathcal{L}_{Yuk} includes the Higgs-fermion interactions (comprising the mass terms of the fermions). λ_i are the Yukawa coupling constants of the Higgs to the leptons, while Λ_{ij} and Λ'_{ij} are the Yukawa coupling matrices of the Higgs to the down-type and up-type quarks, respectively; i and j loop over the fermion generations.

$$\mathcal{L}_{\text{Yuk}} = -\lambda_i (\bar{\nu}_L^i, \bar{e}_L^i) \phi e_R^i - \Lambda_{ij} (\bar{u}_L^i, \bar{d}_L^i) \phi d_R^j - \Lambda'_{ij} (-\bar{d}_L^i, \bar{u}_L^i) \phi u_R^j + h.c., \quad \phi = \begin{pmatrix} \phi^+ \\ \phi^0 \end{pmatrix}$$

The Λ and Λ' matrices introduce a mixing between quarks, allowing flavour-changing transitions between an up-type quark and a down-type quark via CC weak interactions. The CKM matrix, which can be obtained from Λ and Λ' , describes this mechanism, as explained in the following paragraph.

CKM matrix The flavour-changing transitions between quarks are possible through CC weak interactions. Nicola Cabibbo first explained this by introducing the eigenstates (d', s') of the weak interactions as a linear combinations of the mass eigenstates (d, s) [3]; this can be expressed through a mixing matrix with a single parameter, the Cabibbo angle $\theta_C \approx 0.23$ [4].

$$\begin{pmatrix} d' \\ s' \end{pmatrix} = \begin{pmatrix} \cos \theta_C & \sin \theta_C \\ -\sin \theta_C & \cos \theta_C \end{pmatrix} \begin{pmatrix} d \\ s \end{pmatrix} \quad (1.1)$$

The Cabibbo theory explains flavour-changing transitions if only two generations are considered. The Cabibbo-Kobayashi-Maskawa (CKM) mixing matrix provides the extension to three generations; it has four free real parameters: three angles θ_{ij} and a complex phase δ [5].

$$V_{ij} = \begin{pmatrix} V_{ud} & V_{us} & V_{ub} \\ V_{cd} & V_{cs} & V_{cb} \\ V_{td} & V_{ts} & V_{tb} \end{pmatrix} =$$

$$= \begin{pmatrix} c_{12}c_{13} & s_{12}c_{13} & s_{13}e^{i\delta} \\ -s_{12}c_{13} - c_{12}s_{13}s_{23}e^{i\delta} & c_{12}c_{13} - s_{12}s_{13}s_{23}e^{i\delta} & c_{13}s_{23} \\ s_{12}s_{23} - c_{12}s_{13}c_{23}e^{i\delta} & -c_{12}s_{23} - s_{12}s_{13}c_{23}e^{i\delta} & c_{13}c_{23} \end{pmatrix} \quad (1.2)$$

The above is the standard parametrization of the CKM matrix, where $c_{ij} = \cos \theta_{ij}$ and $s_{ij} = \sin \theta_{ij}$. The complex phase δ is responsible for the CP violation.

The Wolfenstein parametrization, which approximates the CKM matrix as a function of the A, λ, ρ, η parameters, is shown here.

$$V = \begin{pmatrix} 1 - \frac{1}{2}\lambda^2 & \lambda & A\lambda^3(\rho - i\eta) \\ -\lambda & 1 - \frac{1}{2}\lambda^2 & A\lambda^2 \\ A\lambda^3(1 - \rho - i\eta) & -A\lambda^2 & 1 \end{pmatrix} + o(\lambda^4) \quad (1.3)$$

This parametrization highlights how transitions between quarks of the same generation are favoured (diagonal terms are close to 1), while transitions between different generations are suppressed (off-diagonal terms are powers of the small parameter $\lambda = \sin \theta_C$). In this parametrization η (which is related to δ) is responsible for the CP violation.

The CKM matrix is unitary ($V_{ij}V_{ik}^* = \delta_{jk}$); this defines nine relations between its elements, for example:

- $V_{ud}V_{ud}^* + V_{us}V_{us}^* + V_{ub}V_{ub}^* = 1$, which means that the probability of the transition of u to any down-type quark is 1;
- $V_{ud}V_{ub}^* + V_{cd}V_{cb}^* + V_{td}V_{tb}^* = 0$, which means that no transition between the d quark and the b quark is possible at tree level.

The relations of the latter kind can be represented through unitarity triangles, such as the one shown in fig. 1.2. The most recent experimental limits for this unitarity triangle are shown in fig. 1.3.

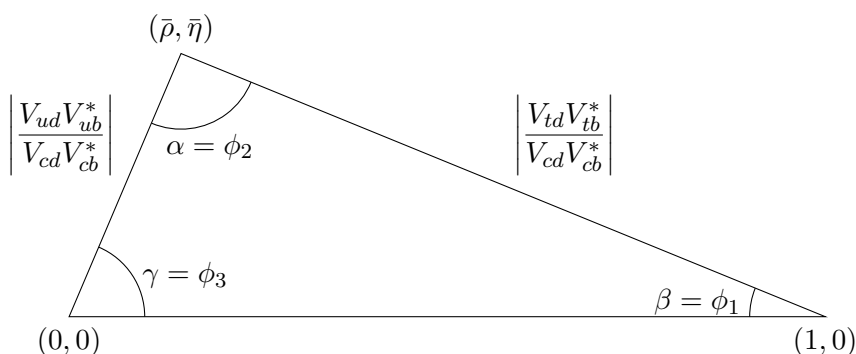


Figure 1.2: The unitarity triangle representing $V_{ud}V_{ub}^* + V_{cd}V_{cb}^* + V_{td}V_{tb}^* = 0$. Its sides are normalized to $V_{cd}V_{cb}^*$. Its angles are determined by the relations $\alpha = \arg \frac{V_{ud}V_{ub}^*}{V_{td}V_{tb}^*}$, $\beta = \arg \frac{V_{td}V_{tb}^*}{V_{cd}V_{cb}^*}$, $\gamma = \arg \frac{V_{cd}V_{cb}^*}{V_{ud}V_{ub}^*}$.

CP violation Flavoured neutral mesons (K^0 , D^0 , ...) are distinguished from their antiparticles only by the flavour quantum number, which is not conserved by weak interaction. This means that both the meson M^0 and the anti-meson \bar{M}^0 can be coupled (weakly) to a single state I , resulting in a chain of transitions

$$M^0 \rightarrow I \rightarrow \bar{M}^0 \rightarrow I \rightarrow M^0 \rightarrow \dots$$

this phenomenon is known as mixing. When the mixing process leads to mass eigenstates that are not flavour eigenstates, flavour oscillations occur.

In the SM, CP violation is introduced by the δ phase of the CKM matrix; there are three classes of phenomenons in which it manifests.

- Direct violation in the decay: when the probability of $M^0 \rightarrow f$ is different from the probability of $\bar{M}^0 \rightarrow \bar{f}$. It is independent from mixing and can occur also in charged mesons.
- Violation in the mixing: when the probability of $M^0 \rightarrow \bar{M}^0$ is different from the probability of $\bar{M}^0 \rightarrow M^0$.

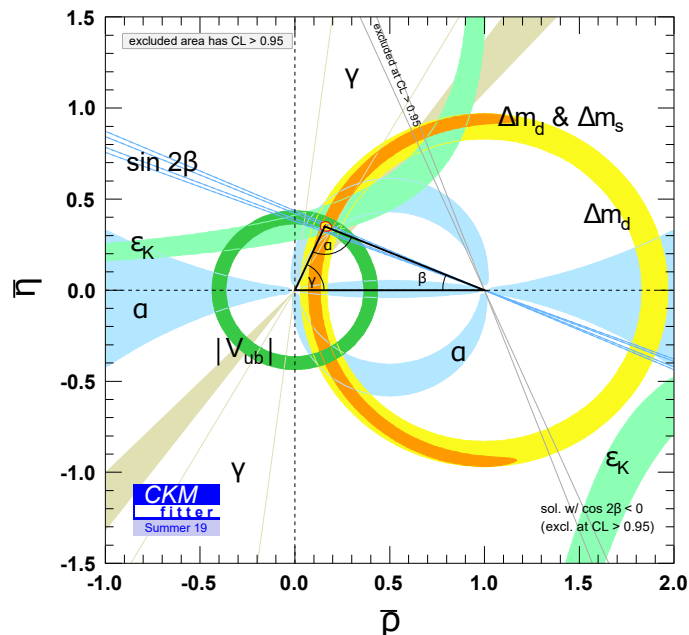


Figure 1.3: Constraints on the CKM matrix parameters in the $(\bar{\theta}, \bar{\rho})$ plane obtained from all experimental measurements [6].

- Violation in the interference between mixing and decay amplitudes: when a final state f is accessible to both M^0 and \bar{M}^0 , it can be accessed both by direct decay $M^0 \rightarrow f$ and through mixing $M^0 \rightarrow \bar{M}^0 \rightarrow f$.

All three types of CP violation have been established experimentally in many transitions, showing a very good agreement with the CKM interpretation [4].

Open questions In spite of the great success of the SM in explaining a broad spectrum of phenomena, many fundamental questions remain open:

- the reason for having three generations of elementary fermions for both leptons and quarks;
- the reason for the mass hierarchy, i.e. the large differences in mass between generations;
- the masses of the neutrinos: in principle one could add a mass term similar to that of the charged leptons (i.e. $-\lambda'_i(-\bar{e}_L^i, \bar{\nu}_L^i)\phi\nu_R^i$) to the SM Lagrangian, but it is not clear whether this would provide the correct explanation;
- the matter-antimatter asymmetry in the universe: the CP violation in the quark sector is not large enough to explain the observed dominance of matter over anti-matter, hence other sources of CP asymmetry must exist;
- the diagonal hierarchy of the CKM matrix: since it is not required by the SM, it may indicate the presence of a flavour symmetry (or another mechanism), which

is unbroken at higher energy scale; in fact, the neutrino mixing matrix (the PMNS matrix) has a completely different, unexplained structure;

- the existence and nature of dark matter.

The SM is probably an effective low-energy approximation of a more fundamental theory. Given the high accuracy with which it describes known phenomena, a large part of the high-energy physics experimental program is devoted to the precision measurement of many processes, with the goal of detecting discrepancies from the SM that may point to physics Beyond the Standard Model (BSM) or New Physics (NP).

1.2 Belle II physics program

Belle II will allow to access a large number of observables that can be used to search for NP in flavour transitions both in the quark and in the lepton sectors. This section gives an overview of the main goals of the experiment, summarising some of the measurements that are planned or ongoing [1].

In the past, many fundamental discoveries were made in the quark sector, suggesting that further examination of it can provide new information. In order to exploit the high precision that Belle II can provide, thanks to the clean environment of e^+e^- collisions and the excellent detector resolution, the experiment will mainly focus on processes with small theoretical uncertainties, for which the comparison to SM predictions has a higher chance of revealing discrepancies that may be interpreted as an indication of NP. Yet, the quark sector program is very broad; the main goals are outlined here, but a detailed discussion is beyond the scope of this thesis.

- Study processes that occur at loop level in the SM, but may have tree-level contributions in NP, e.g. flavour-changing neutral currents (FCNCs), neutral meson mixing, CP violation. Decays of down-type quarks (i.e. s and b) are the most promising for these searches, because their SM CKM couplings are greatly suppressed, hence naturally providing a good sensitivity to NP. Yet, there are conceivable NP models with a non-standard dynamic that favours, e.g., FCNC transitions in the up-type sector; in the search for such processes the c quark is of fundamental importance, as it is the only up-type quark that can be observed to decay weakly (the t has such a large decay width that it decays strongly before hadronising). Thanks to its particle identification performance, vertex resolution and neutral particles reconstruction capabilities, Belle II will play a key role in the search for evidence of such non-standard dynamics.
- Search for NP by discrepancies (with respect to the SM) in phases, CP asymmetries, inclusive decay processes, rare leptonic decays and absolute branching ratios (BRs). For instance, differences between B^0 and \bar{B}^0 decay rates will be searched for via measurements of time-dependent CP violation in penguin $b \rightarrow s, d$ transitions, such as the $B \rightarrow \phi K^0$ and $B \rightarrow \eta' K^0$ decays. Also, large amounts of CP violation were observed in the time-integrated rates of charmless hadronic B decays (e.g. $B \rightarrow K\pi$ and $B \rightarrow K\pi\pi$) by experiments such as Belle, BaBar and LHCb; Belle II will provide information that may help understanding the mechanism at the origin of such effects.
- Search for new invisible particles, such as dark matter candidates and axion-like particles, via missing energy in decays. Belle II has a unique sensitivity to missing

energy at the MeV and GeV scale thanks to the clean collision environment, the completely-known initial state (collision energy, centre-of-mass boost, etc.), and the near-hermeticity of the detector.

- Measure CP violation in D^0 mixing: this is negligible in the SM, providing a high sensitivity to NP effects. Belle II has an improved D^0 proper time resolution with respect to BaBar and Belle, and the higher resolution is expected to improve background rejection. The LHCb experiment has provided extremely precise measurements in this sector by looking for decays with charged particles in the final state; Belle II will be complementary to it by looking for D^0 s decaying in neutrals, thanks to its neutral particle reconstruction capabilities. In addition, the cleaner environment and excellent charged particle reconstruction capabilities will allow Belle II to compete with LHCb.
- Measure CKM observables with improved precision. For instance, Belle II will be able to provide measurements of $|V_{ub}|$ and $|V_{cb}|$ by studying B decays; the higher statistics will already allow to improve the precision with respect to currently available measurements. As for the charm program, studies of leptonic and semileptonic decays of charm mesons, where the electroweak portion of the interaction is well understood, can provide measurements of products of a CKM matrix element and a form factor, e.g. $|V_{cd}|f_D$ or $|V_{cs}|f_{D_s}$. The form factors can now be calculated with good precision using lattice QCD (LQCD), allowing to perform three different measurements:
 - form factor measurements by assuming CKM matrix elements values, allowing to test LQCD predictions;
 - CKM matrix elements measurements by assuming form factor values;
 - measurements of ratios of BRs where CKM matrix elements cancel out, allowing to test LQCD predictions in an unbiased manner.
- Study QCD at the low-energy regime by studying exotic quarkonia states that are not predicted by the conventional meson interpretation. New particles can be produced near resonance either by adjusting the collision energy, or by exploiting initial-state radiation to obtain a continuum of centre-of-mass energies. For this purpose, Belle II will take some “off-resonance” runs, with a collision energy different from the peak of the $\Upsilon(4S)$ resonance.
- Search for lepton flavour universality violation in semileptonic B decays, for instance by measuring $\mathcal{R}(D^*) = \text{BR}(\bar{B} \rightarrow D^* \tau^- \bar{\nu}_\tau) / \text{BR}(\bar{B} \rightarrow D^* \ell^- \bar{\nu}_\tau)$, where ℓ is either e or μ . Current experimental results for this ratio show a discrepancy with respect to the SM prediction: since Belle II is expected to be able to measure it with high accuracy, this may become a powerful test for NP.

As B-factory experiments also produce large samples of $\tau^+ \tau^-$ pairs, several measurements in the τ sector are also planned; the main goals are outlined here.

- Search for lepton flavour violation in τ decays. The sensitivity of these searches will be improved by orders of magnitude with respect to Belle and BaBar, thanks to the much higher statistics, but also to the improved resolution and the higher trigger and reconstruction efficiencies.

- Search for CP violation in τ decays by cross section measurements and angular observables.
- Search for charged Higgs-like couplings to the τ lepton, again by cross section and angular observables measurements.

In all of the aforementioned studies, detector performance and resolution play a key role, as they are necessary to reach maximum measurement precision. In particular, many of these measurements require the accurate determination of the decay vertex of B , D or τ particles, for which the vertex detector plays a crucial role.

Chapter 2

SuperKEKB and Belle II

This chapter describes the main features of the experiment: the SuperKEKB collider and the Belle II detector. First, a general introduction to B-factory experiments is given; then, SuperKEKB is described; afterwards, beam-induced background sources are presented; finally, an overview of the Belle II detector is given, also featuring some general information about the software framework used.

2.1 B-factory experiments

A B-factory is an electron-positron collider tuned to produce B meson pairs: the most efficient way to achieve this is to tune the collision energy to the $\Upsilon(4S)$ resonance, which is the lightest strong resonance with enough mass to decay in b -flavoured mesons. Indeed $m_{\Upsilon(4S)} \approx 10.58 \text{ GeV}/c^2$ while $2m_B \approx 10.56 \text{ GeV}/c^2$, and the branching fraction (BF) for $\Upsilon(4S) \rightarrow B\bar{B}$ is $\approx 96\%$ (with $\rightarrow B^0\bar{B}^0$ and $\rightarrow B^+B^-$ having almost equal probability).

Electron-positron colliders have many advantages that can be leveraged in analyses of different kinds:

- they have much cleaner events than hadronic machines, and higher trigger efficiencies, making them ideal for studying rare or forbidden processes;
- the average track multiplicity is low (the typical event has 11 charged tracks [7]), leading to low detector occupancy and high reconstruction efficiency for B , D and τ , with low trigger bias;
- the recorded luminosity can be determined by measuring Bhabha scattering, allowing to measure absolute (besides relative) BFs;
- the precise knowledge of the centre-of-mass (CM) energy, coupled with an excellent detector hermeticity, allows performing missing-mass analyses, where the existence of new, undetected particles is inferred from energy/momentum conservation;
- the initial state quantum numbers are known, and the B^0 s are produced in a coherent quantum state, allowing interference studies to be performed;
- all of the above allow to reduce systematic uncertainties, while the fact that there are usually many control samples available for background study allow to estimate said uncertainties accurately.

The two B mesons resulting from the decay of the $\Upsilon(4S)$ are entangled and, since the $\Upsilon(4S)$ is unflavoured, this implies that the flavour of one B can be inferred by the knowledge of the flavour of the other one. Since the B mesons are produced with small momenta (the Q -value of the decay is only ≈ 20 MeV, resulting in CM-frame momenta $p_B^* \approx 300$ MeV/ c), energy-asymmetric collisions become necessary in measurements that require the knowledge of the decay time (e.g. time-dependent CP violation), as the boost in the CM frame would produce decay lengths that are insufficient to precisely measure the decay time. The first-generation B-factory experiments, BaBar at PEP II and Belle at KEKB, had a centre-of-mass boost $\beta\gamma$ of 0.56 and 0.43, respectively, and collected a total of 424 fb^{-1} and 711 fb^{-1} in the years 1999–2008, leading to an extremely rich set of publications [8].

B-factories are not only efficient at producing B meson pairs: for instance, they are also able to generate a similar number of τ pairs, allowing many analyses in the τ sector. The production cross sections are summarized in tab. 2.1.

| $e^+e^- \rightarrow$ | σ [nb] | $e^+e^- \rightarrow$ | σ [nb] |
|----------------------|-------------------|----------------------|-----------------------|
| $u\bar{u}$ | 1.61 | e^+e^- | 300 ± 3 |
| $d\bar{d}$ | 0.40 | $\mu^+\mu^-$ | 1.148 |
| $s\bar{s}$ | 0.38 | $\tau^+\tau^-$ | 0.919 |
| $c\bar{c}$ | 1.30 | $\nu\bar{\nu}$ | 0.25×10^{-3} |
| $\Upsilon(4S)$ | 1.110 ± 0.008 | | |

Table 2.1: Total production cross sections at $\sqrt{s} = 10.58$ GeV [1]. The one for Bhabha scattering ($\rightarrow e^+e^-$) is computed for $E_e^* > 0.15$ GeV and $10^\circ < \theta_e^* < 170^\circ$, which is roughly the acceptance of Belle II.

2.2 The SuperKEKB accelerator

SuperKEKB is an energy-asymmetric electron-positron collider located at the KEK laboratory in Tsukuba, Japan. It was built by upgrading the KEKB collider, where the Belle experiment took place; it has a design luminosity of $8 \times 10^{35} \text{ cm}^{-2}\text{s}^{-1}$, 40 times higher than that achieved by KEKB, and a goal to integrate a total of 50 ab^{-1} .

As shown in fig. 2.1, SuperKEKB consists of a 7 GeV electron ring (the high-energy ring, HER), a 4 GeV positron ring (the low-energy ring, LER), and an injector linear accelerator (LINAC) with with a 1.1 GeV positron damping ring (DR). The extremely high luminosity required significant upgrades to the HER, LER and final-focus system of KEKB, and also to the LINAC and DR as low-emittance injection and high-current beams are necessary [9].

If we use the subscript $+$ for positrons and $-$ for electrons, we can express the luminosity L of a collider as

$$L \approx \frac{\gamma_{\pm}}{2er_e} \left(1 + \frac{\sigma_y^*}{\sigma_x^*} \right) \frac{I_{\pm} \xi_{y\pm}}{\beta_y^*}, \quad \xi_{y\pm} \propto \frac{N_{\mp} \beta_y^*}{\sigma_x \sigma_y} \quad (2.1)$$

where γ is the Lorentz factor, $\sigma_{x,y}^*$ and β_y^* are the beam sizes and vertical beta function at the interaction point (assumed equal for the two beams), and I is the beam current. The beam-beam parameter ξ_y models the focusing force that a bunch undergoes from the electromagnetic field of the opposite bunch, and depends on the number of particles N in the latter [10].

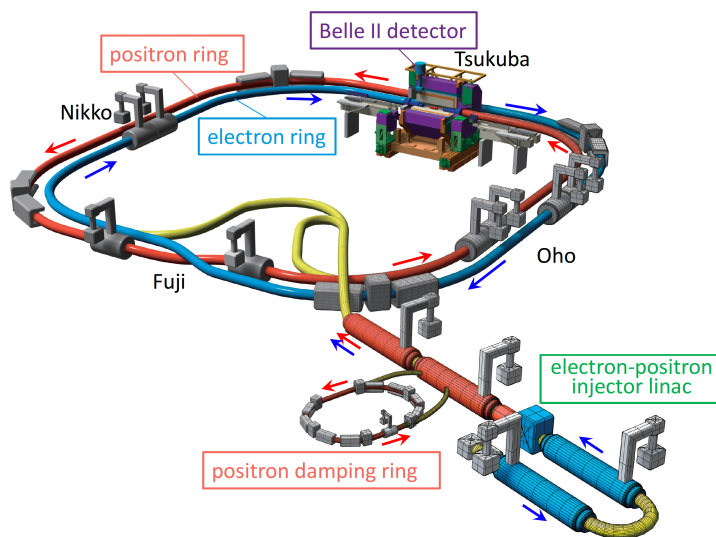


Figure 2.1: Schematic view of SuperKEKB.

For practical reasons (e.g. hardware feasibility and operating costs) it is not possible to increase the beam currents I by more than a small factor; achieving ξ_y values much higher than those of previous colliders is similarly impractical.

Thus, decreasing β_y^* by a large factor was pursued for the upgrade of KEKB. This was achieved by employing the *nano-beam* scheme, initially developed for the SuperB project [11]: the vertical beam size is reduced to $\sigma_y = 60$ nm by squeezing β_y^* to 0.3 mm (about 20 times smaller than at KEKB). This, however, increases non-linear beam-beam interactions, leading to smaller beam lifetimes and other instabilities. Also, the transverse beam size is kept at minimum only over a short distance (order of β_y^*): since the bunch length ($\sigma_z \approx 5$ mm) is greater than that, the actual luminosity is smaller: this is known as hourglass effect.

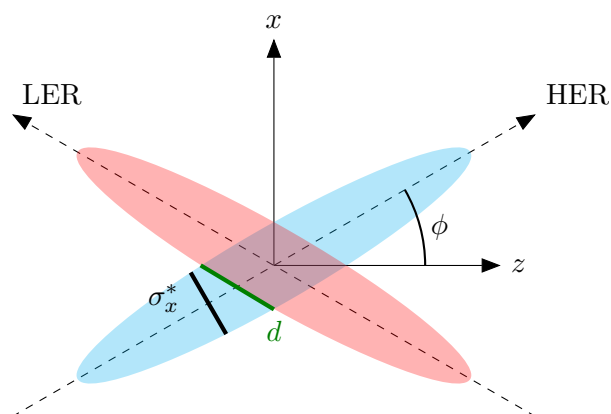


Figure 2.2: Representation of the interaction between two bunches in the *nano-beam* scheme (pictorial and not to scale). The effective bunch length d is given by the overlap region, and is related to the horizontal beam size σ_x^* and the horizontal half crossing angle ϕ by the relation $\sigma_x^* = d \sin(2\phi)$.

To eliminate the hourglass effect, the effective bunch length (see d in fig. 2.2) must be

kept smaller than β_y^* : this was achieved by using extremely small horizontal emittances and beta functions at the interaction point (resulting in $\sigma_x^* \approx 10 \mu\text{m}$, 8 times smaller than at KEKB) and by increasing the half crossing angle ($\phi = 41.5 \text{ mrad}$, 4 times larger than at KEKB).

All these modifications resulted in a smaller boost of the CM frame ($\beta\gamma = 0.28$, 1.5 times smaller than at KEKB), which reduces the average flight distance of B mesons from about $200 \mu\text{m}$ to about $130 \mu\text{m}$. This is compensated by the improvements in the innermost pixel tracking detector, in particular by the fact that the smaller beam pipe (radius reduced to 10 mm , 1.5 times smaller than that of KEKB) allows to place the innermost layer at about half the distance with respect to Belle, resulting in an improvement of impact parameter resolution of a factor ≈ 2 .

The smaller boost is actually advantageous for missing-mass analyses, as it contributes positively to the detector's hermeticity.

Finally, the smaller beam lifetimes, together with the higher design currents, are the main reason behind the injection system upgrade.

Some of the main parameters of SuperKEKB are shown (and compared to those of KEKB) in tab. 2.2. It can be noted that many of the achieved parameters are still far from the design values, but this is not surprising since SuperKEKB is a very challenging machine operating in a regime that was never explored before. Reaching full luminosity will require several years and the full understanding and control of many subtle effects in the accelerator.

| | KEKB Achieved | SuperKEKB Design | SuperKEKB Achieved |
|---|------------------|---------------------|-----------------------|
| Energy (LER/HER) [GeV] | 3.5/8 | | 4/7 |
| Lorentz boost $\beta\gamma$ | 0.43 | | 0.28 |
| Crossing angle 2ϕ [mrad] | 22 | | 83 |
| Current (LER/HER) [A] | 1.6/1.2 | 3.6/2.6 | 0.85/0.82 |
| σ_x^* (LER/HER) [μm] | 80 | 10/11 | 18/17 |
| σ_y^* (LER/HER) [nm] | 1100 | 48/62 | 230 |
| β_x^* (LER/HER) [mm] | 1200 | 32/25 | 80/60 |
| β_y^* (LER/HER) [mm] | 5.9 | 0.27/0.30 | 1/1 |
| ε_x (LER/HER) [nm] | 24/18 | 3.2/4.6 | 4/4.6 |
| ε_y (LER/HER) [pm] | 240/180 | 8.6/13 | 60/45 |
| Luminosity [$10^{34} \text{ cm}^{-2}\text{s}^{-1}$] | 2.1 | 80 | 3.1 |

Table 2.2: Summary table of some of the main parameters of SuperKEKB, compared to those of KEKB [10, 12, 13].

2.2.1 Beam-induced background

The higher performance of SuperKEKB with respect to KEKB, achieved with higher beam currents and smaller beam size at the interaction point (IP), implies higher beam-induced background in the Belle II detector. Properly estimating, mitigating and monitoring this background is critical to the success of the experiment.

In this section, the main sources of beam-induced backgrounds are described. They can be classified in two categories: single-beam sources, which are due to the beam interacting with itself and its environment, and luminosity-dependent or beam-beam

sources, which are due to the interaction of the two beams. Also the injection process is responsible for part of the background, and deserves a category of its own [14].

Additionally, there are occasional events when the beams become unstable, leading to large beam losses that cause a large radiation dose to be absorbed by the detector in a short period of time. These beam losses are also a source of background, but most of all they are a source of radiation damage because of the radiation spikes [15]. Section 3.1.3 describes the system adopted to monitor beam losses and mitigate their effects on the detector.

Single-beam backgrounds

Touschek scattering It is an intra-bunch process where the Coulomb scattering of two particles in the same bunch changes the particle's momenta: one particle ends up with an energy higher than nominal, the other, with an energy lower than nominal. These particles are lost when, after propagating along the ring, they hit the inner wall of the beam pipe; if this happens close enough to the IP, the resulting shower might reach the detector.

The Touschek scattering rate in SuperKEKB can be approximated by using the following formula to scale the values measured with KEKB

$$R \propto \frac{N_b I_b^2}{\sigma_y E^3} \quad (2.2)$$

where N_b is the number of bunches, I_b is the bunch current and E is the beam energy. From this, a rate ≈ 20 times higher than at KEKB can be expected.

Touschek scattering is mitigated by using movable metal-head collimators in the beam pipe, and metal shields around the detector.

Beam-gas scattering It is the scattering of beam particles on residual gas molecules in the beam pipe; it happens via two processes: Coulomb scattering, which changes the direction of the beam particles, and *bremsstrahlung* scattering, which reduces the energy of the beam particle. These particles are lost, like those that undergo Touschek scattering, when they hit the inner wall of the beam pipe after propagating along the ring.

The beam-gas scattering rate is approximately $\propto IP$, where I is the beam current and P is the pressure inside the beam pipe. Since the pressure is similar to that at KEKB, the rate is expected to increase by a factor ≈ 2 at nominal luminosity.

Beam-gas scattering is mitigated by using collimators and metal shields, like for Touschek scattering.

Synchrotron radiation The rate of this background is $\propto E^2 B^2$, where E is the beam energy and B is the intensity of the magnetic field: this makes the HER beam the main source of this type of background. The energy spectrum of synchrotron radiation (SR) photons ranges in the order of 1 keV to 10 keV.

KEKB employed a shared final-focus quadrupole (QCS) magnet for both incoming and outgoing beams: since the beams could not be on the axis of the shared magnet, they underwent a larger B on average, yielding additional SR. SuperKEKB, instead, uses separate QCS magnets for the two beams, which end up nearly on the axis of the magnetic field, thus reducing SR.

SR is mitigated by the ridge structures and the gold coating of the inner wall of the beryllium beam pipe inside of the detector region.

Luminosity-dependent backgrounds

Radiative Bhabha scattering Photons produced in radiative Bhabha scattering ($e^+e^- \rightarrow e^+e^-\gamma$) events propagate along the beam axis and interact with the iron of the accelerator magnets: here they cause a large production of low-energy gamma rays and neutrons, which constitute the main background sources for the outermost parts of the detector. Since this background is proportional to the luminosity, it is expected to increase by a large factor with respect to KEKB.

After the process, the energies of both electron and positron decrease. With KEKB's shared QCS magnet, the scattered particles were over-bent and hit the iron of the magnets, producing showers; this is not the case in SuperKEKB, thanks to the separate QCS magnets, except for the small fraction of the particles that undergo a large energy loss. Still, with the nominal luminosity being ≈ 40 times higher, this rate is not negligible, and might be the main source of background in some of the subdetectors.

Radiative Bhabha background is mitigated by heavy material shielding inside the detector volume.

Two-photon process This background is constituted by the low-momentum electron-positron pairs produced in the two-photon process $e^+e^- \rightarrow e^+e^-e^+e^-$, shown in fig. 2.3. Such particles can spiral in the magnetic field of the solenoid and produce multiple hits, particularly in the innermost layers of the tracking detectors.

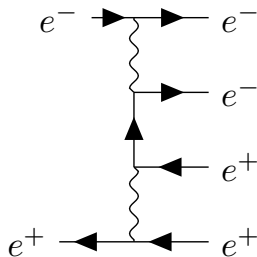


Figure 2.3: The Feynman diagram of the two-photon process.

Additionally, the primary beam particles that produced the pair may lose a large amount of energy and can be lost by hitting the beam pipe, like it happens for radiative Bhabha background.

The two-photon background could be mitigated by a larger magnetic field, but this is not straightforward to implement with the Belle II magnet, and may have other detrimental effects on tracking at low momentum.

Injection background

Similarly to KEKB, SuperKEKB uses a “continuous” (*top-up*) injection scheme [10, 16], where electrons and positrons are injected atop the circulating beams in order to prevent the currents from dropping: this is necessary to maintain constant luminosity despite the short beam lifetimes (≈ 600 s). The injection scheme is sketched in fig. 2.4:

- the circulating beam is steered by a kicker close to the wall of the injection septum magnet: this happens in the horizontal plane, which has larger acceptance;
- the injected beam is steered by the septum magnet on an orbit close to that of the circulating beam: a finite gap between the two inevitably remains, due to the thickness of the septum magnet wall;
- another kicker steers the circulating beam back to its nominal orbit, together with the injected beam; the latter, however, remains shifted by a finite amount;
- the injected beam circulates along the ring and performs betatron oscillations, which are progressively damped by SR losses and by the bunch-by-bunch feedback system of the machine.

The transverse damping time is ≈ 50 ms for both rings, corresponding to about 5000 revolutions; the bunch-by-bunch feedback system plays a crucial role by reducing this time, as the maximum repetition rate of the injection is 25 Hz.

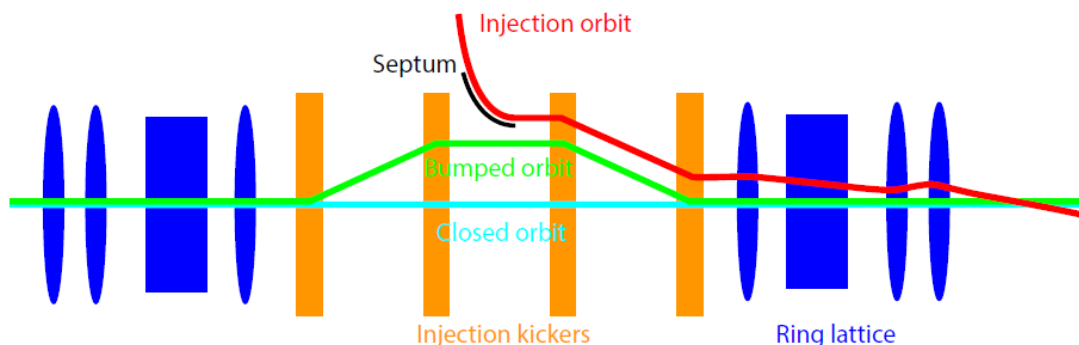


Figure 2.4: Schematic of the injection scheme. Taken from [16].

While the damping occurs, the injected bunch produces a higher background: mainly SR, which is the main damping mechanism, but injected particles that are too much off of the nominal orbit may hit the beam pipe as well. Especially in the first few ms after the injection, much higher background rates and occupancies are observed in the detector as the injected bunch passes by the IP: the large number of hits prevents an accurate reconstruction of these events, making them useless for analyses, while also possibly saturating the readout bandwidth of some subdetectors. Therefore, an “injection veto” is applied to the trigger to prevent these events from being recorded or even just read out; the timing of the veto signal is chosen empirically by looking at the distribution of the detector occupancy vs the time since last injection.

The injection operation is automatically triggered when the beam current drops below a certain threshold, typically $\sim 99\%$ of the intended value, and automatically stops when the intended value is reached again; the two beams perform the injection independently. Since the injected bunch passes by the detector every $10\ \mu\text{s}$ (one revolution period), the injection veto is a $\sim 2\ \mu\text{s}$ long signal repeated every $10\ \mu\text{s}$ until the damping is completed (i.e. for 4 ms to 20 ms, depending on injection conditions); the timing parameters for the injection veto are adjusted during the runs to minimise the dead time, which typically ranges from 1% to 5%, based on the background rates observed.

2.3 The Belle II detector

The upgrade of KEKB to SuperKEKB required also a substantial upgrade of the detector: higher event rate ($\times 50$ at design luminosity) and background ($\approx \times 20$) pose a challenge for the detector's performance and require higher rate capabilities and radiation tolerance.

The upgrade design was dictated by physics requirements, with the goal of obtaining equal or better performance than Belle at KEKB [1]:

- large acceptance and high efficiency for B meson decays, necessary to maximise the statistics;
- good momentum and energy resolutions, vital to separate small signals from background;
- excellent vertex resolution, required by several analyses (D^0 lifetime measurement, time-dependent CP violation, etc.);
- efficient and clean particle identification for hadrons, necessary to reduce combinatorial background;
- low material budget, necessary to reduce uncertainties on momentum and tracking parameters (from multiple Coulomb scattering) and on photon energy;
- offset with respect to the IP and asymmetric layout, to exploit the asymmetric energy of the collisions and the resulting boost of the CM frame.

The structure of the detector and its subdetectors (from innermost to outermost) are briefly outlined here; the following sections describe each component in more detail. Starting from the beam line, one finds:

- The *vertex detector* (VXD), immediately outside the beam pipe, composed of:
 - the *pixel detector* (PXD), which is the innermost subdetector and is mainly used to improve vertex resolution;
 - the *silicon vertex detector* (SVD), used for tracking/vertexing and also for particle identification (from dE/dx information).
- The *central drift chamber* (CDC), the main tracking device of the experiment, also used for particle identification (from ionization energy loss information).
- Two Cherenkov-effect-based subdetectors for particle identification:
 - the *time-of-propagation* detector (TOP), which covers the barrel part, and exploits the measurement of the time of propagation of Cherenkov photons, together with two-dimensional spatial information, to reconstruct Cherenkov rings;
 - the *aerogel ring-imaging Cherenkov* detector (ARICH), which covers the forward endcap, and is used to measure particle velocities from the Cherenkov angle of the emitted photons.
- The *electromagnetic calorimeter* (ECL), used for measuring energy and angle of neutral particles (particularly photons), as well as electrons.

- The superconducting solenoid generating the 1.5 T longitudinal magnetic field, necessary for tracking.
- The K_L^0/μ detector (KLM), realised by instrumenting the return yoke of the magnet, used to detect and identify these long-lived, highly-penetrating particles.

Some of the material and components from Belle were reused, e.g. the mechanical structure, the solenoid and its return yoke, the resistive plate chambers (RPCs) used in KLM, the CsI(Tl) crystals used in ECL.

The coordinate system of the Belle II detector, a cylindrical system with the z axis along the electron beam, is shown in fig. 2.5, while a top-view schematic is shown in fig. 2.6.

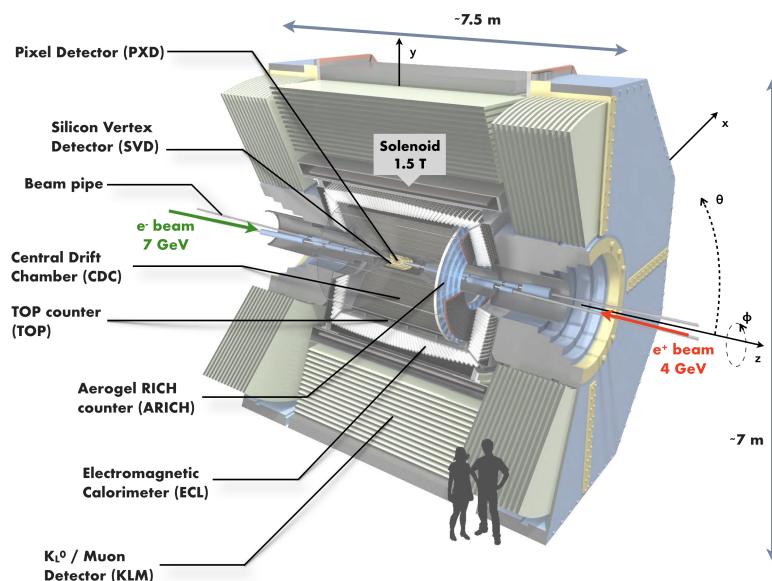


Figure 2.5: A 3D view of the Belle II detector, with the coordinate system shown: the z axis is the bisector of the beams and is directed forwards (like the CM frame boost); the y axis is directed upwards; the x axis is horizontal and directed away from the accelerator's centre; the origin is the nominal IP; the polar angle θ is zero on the positive z semi-axis, while the azimuthal angle ϕ is zero on the positive x semi-axis. Image taken from [17].

2.3.1 PXD

Thanks to the reduced beam pipe radius (1 cm instead of 1.5 cm), the innermost layers of the VXD can be placed closer to the interaction point (IP), which is advantageous for vertex resolution. However, this fact, with the higher beam background, leads to higher occupancy (fraction of channels hit during an event): for this reason pixel sensors were chosen over strip sensors, as they have many more readout channels and, thus, much smaller occupancy.

PXD sensors are based on the depleted field effect transistor (DEPFET) technology, realised with very thin ($< 100 \mu\text{m}$) sensors, allowing to minimise multiple scattering, thus improving the tracking resolution for low-momentum particles. A schematic of a DEPFET is shown in fig. 2.7. When a charged particle crosses the depleted bulk, it

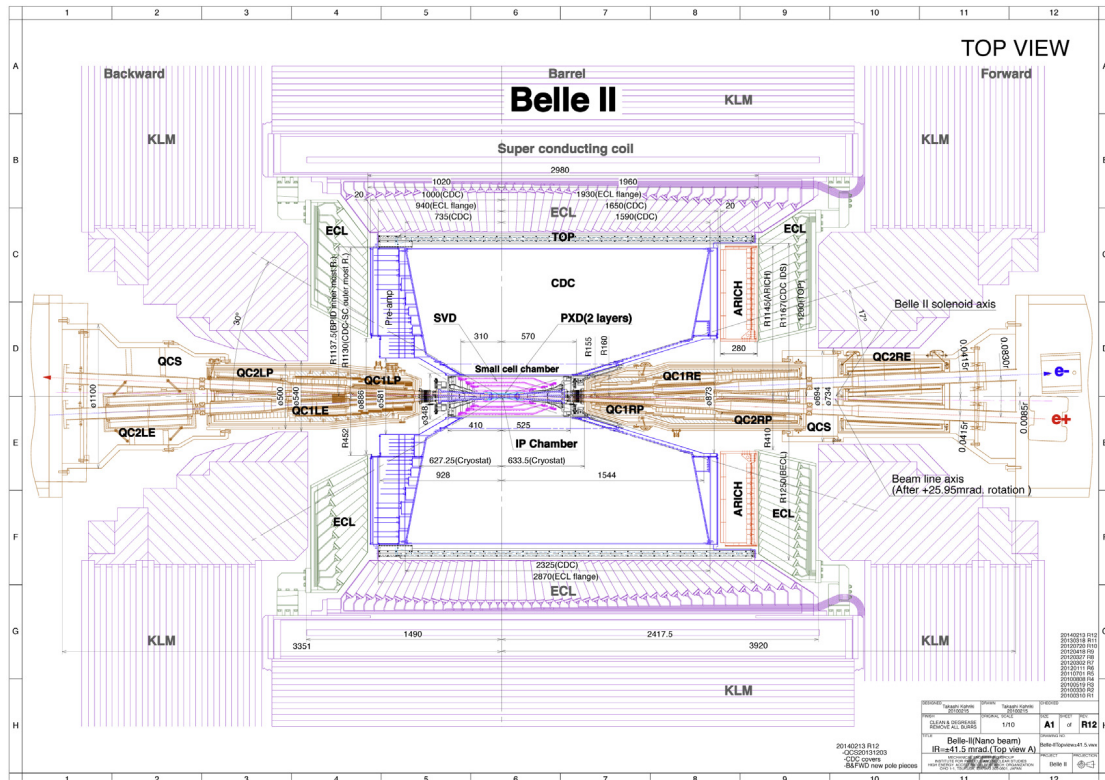


Figure 2.6: Top-view cross-section schematic of the Belle II detector.

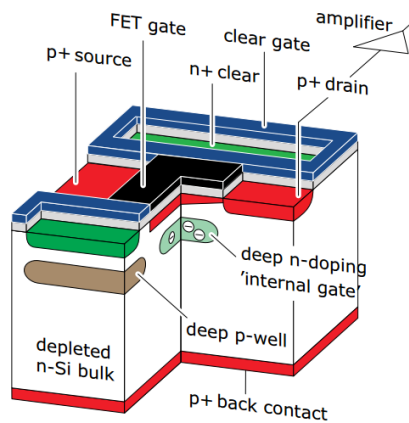


Figure 2.7: Schematic of the DEPFET-based pixels of PXD.

generates electron-hole pairs, and the electrons drift, in the electrical field generated by the bias voltage, to *internal gate* where they are collected. The current circulating through the FET (from the *drain*, connected to the amplifier, to the *source*) is modulated by the voltage on the *gate*: a voltage needs to be applied to the gate in order to have a current; however, since the internal gate is capacitively coupled to the gate, the current also depends on the accumulated charge. The accumulated charge remains in the internal gate until removed by applying a positive voltage to the *clear gate*. The fact that the reading has to be “turned on” by applying a voltage to the gate allows to use a single amplifier to read a column of pixels, one at a time, or multiple amplifiers to read columns of pixels, one row at a time; this readout scheme is called *rolling shutter*, and is the one used by PXD.

PXD is made of two layers (L12); each layer is made of several planar *ladders*; each ladder is made of a support structure hosting two sensors and their readout electronics, which is outside of the acceptance region and in thermal contact with the support structure. Air cooling of the support structure is sufficient as the pixels use little current, while active cooling based on a CO₂ evaporative system is necessary for the readout electronics.

The readout takes $\approx 20 \mu\text{s}$, therefore multiple events may overlap. Also, since all hits are integrated during these $20 \mu\text{s}$, the only way to apply the injection veto to PXD hits is to turn off the bias voltage while the injected bunch passes by the detector (“gated mode”); when turning back on, however, the sensors need some time to reach stable conditions, thus introducing a dead time; the optimization of the gated mode is still in progress. PXD is not used for finding tracks, but only to improve the resolution of the tracks found by CDC and SVD [18].

Detailed information about the layers is summarised in tab. 2.3, while the layout is shown in fig. 2.8.

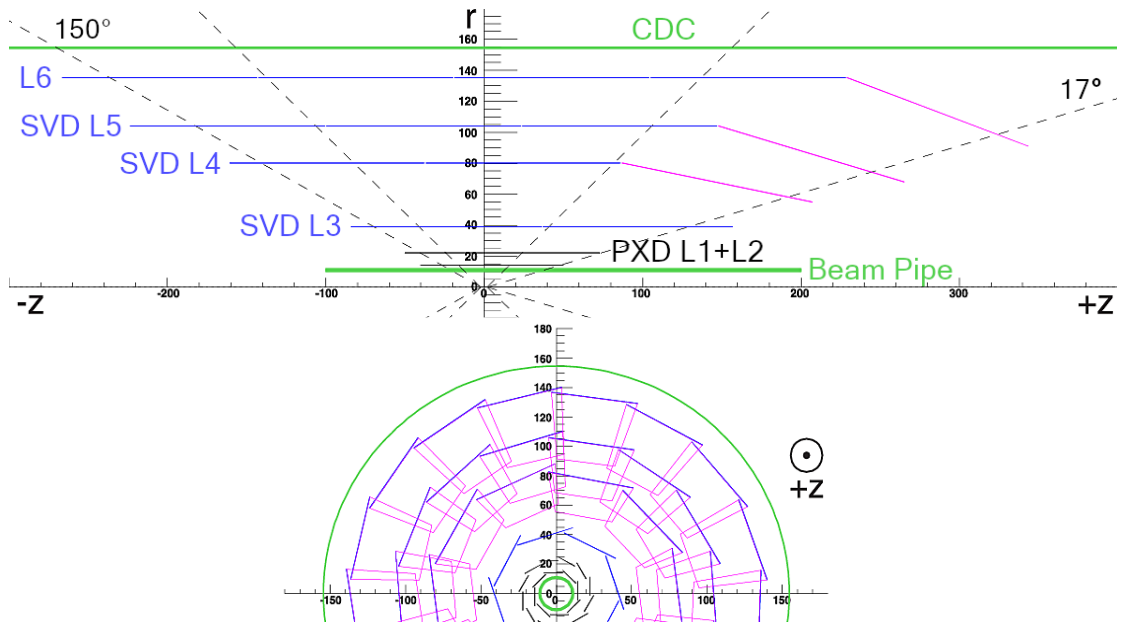


Figure 2.8: Schematic side view (above) and front view (below) of the VXD.

| | PX D | | SVD | | | |
|--------------------------------|------------------|-------|-----------|---------------|--------|--------|
| | L1 | L2 | L3 | L4 | L5 | L6 |
| Radius [mm] | 14 | 22 | 39 | 80 | 104 | 135 |
| N. ladders | 8 | 12 | 7 | 10 | 12 | 16 |
| N. sensors/ladder | 2 | 2 | 2 | 2 + 1* | 3 + 1* | 4 + 1* |
| N. sensors | 16 | 24 | 14 | 30 | 48 | 80 |
| ϕ pitch [μm] | 50 | 50 | 50 | 75, 75 to 50* | | |
| z pitch [μm] | 60 | 80 | 160 | 240 | | |
| Thickness [μm] | 75 | | 320 | 320, 300* | | |
| Mat. budget [X_0] | 0.19% | | 0.70% | 0.70% | | |
| N. channels/sensor | 768 \times 250 | | 768 + 768 | 768 + 512 | | |
| N. channels | 3 M | 4.6 M | 22 k | 38 k | 61 k | 102 k |

Table 2.3: Summary table of the main features of the VXD layers. Fields with an * are relative to the trapezoidal, slanted sensors of SVD. For SVD, the readout pitch is indicated; on both sides, a floating strip is present between two readout strips.

2.3.2 SVD

The Belle II SVD design is based on that of the Belle vertex detector. Since a lower particle background rate than in the PXD is expected, double-sided silicon strip detectors (DSSD) are used, like in the Belle vertex detector, instead of pixel sensors, allowing to achieve similar vertex-detection performance with a much smaller number of readout channels.

To cope with the high particle rate due to beam-induced background, a readout chip with a fast shaping time of $\mathcal{O}(50\text{ ns})$ was chosen: the APV25 [19], originally developed for the CMS tracker. To minimise its noise, the APV25 input capacitance must be kept at minimum: for this reason, the APV25 hybrids are mounted directly on the DSSD; this, and the subsequent necessity for cooling pipes on the sensors, contributes to the material budget ($0.7\%X_0$ per layer, with the sensors contributing only for $0.32\%X_0$).

SVD is made of four layers (L3456); each layer is made of several *ladders*; each ladder is made of a support structure hosting 2 to 5 sensors with their readout chips and their cooling pipes. The radial coverage is almost twice that of the Belle SVD2: this improves tracking, but requires a larger surface to be covered. This is partly compensated in L456 ladders by using a trapezoidal sensor at the forward end, which is tilted towards the beam pipe axis, thus covering the whole θ range with a smaller sensitive area; this gives SVD a lantern-like shape.

SVD is used both to find tracks on its own, and to improve the resolution of the tracks found by CDC. Moreover, it is able to accurately reconstruct the vertices of particles that decay outside the volume of PXD, such as K_S^0 . Finally, it provides dE/dx information, used for particle identification [7].

Some information about the layers is summarised in tab. 2.3, while the layout is shown in fig. 2.8. Since this thesis strongly focuses on SVD, a much more detailed description of it is given in section 3.1.

2.3.3 CDC

The Belle II CDC design is largely based on that of the Belle CDC: the main characteristics and differences are shown in tab. 2.4.

| | Belle | Belle II |
|---|---|----------|
| Inner cylinder radius mm | 77 | 170 |
| Outer cylinder radius mm | 880 | 1130 |
| Number of layers | 50 | 56 |
| Number of sense wires | 8.4 k | 14.3 k |
| Diameter of sense wires [μm] | | 30 |
| Gas mixture | He 50%, C ₂ H ₆ 50% | |

Table 2.4: Main features of the Belle II CDC, compared to those of the Belle CDC [18].

The readout electronics has been upgraded: on the backward end plate are frontend boards capable of discriminating hits and measuring both signal charge and drift time. These are faster than Belle’s, a necessary measure to counter the increased background. The forward end plate is used for HV cables.

The CDC has 56 layers of sense wires, grouped in 9 *superlayers* with 6 layers each (except for the innermost one, which has 8 layers). As shown in fig. 2.9, axial superlayers, with cables $\parallel z$, are alternated to “stereo” superlayers, with cable tilted by $\mathcal{O}(50\text{ mrad})$ to provide z information. The aluminum field wires are placed between the sense wires.

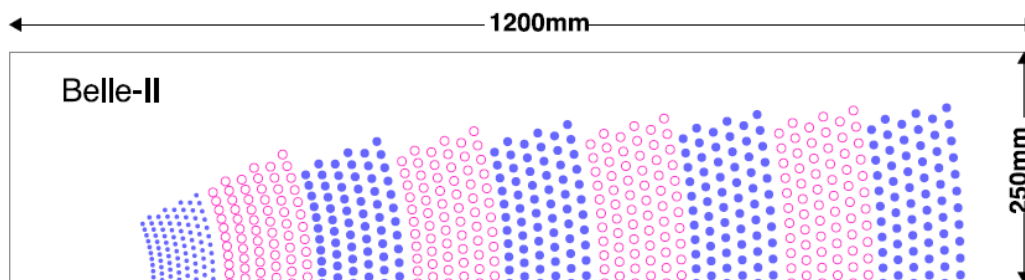


Figure 2.9: Schematic view of the CDC drift cells. Blue filled dots are used for axial wires, pink empty ones for stereo wires, making the subdivision in superlayers evident. Taken from [20].

The CDC plays three important roles: it reconstructs three-dimensional charged tracks and measures their momenta; it provides dE/dx information for particle identification, which is particularly useful for low-momentum particles that cannot reach the outer particle identification subdetectors; it provides reliable and efficient charged-tracks based trigger signals, which exploit the three-dimensional track information to suppress background without sacrificing physics events.

Like PXD and SVD, CDC has an angular acceptance of 17° to 150° . The spatial resolution is $\approx 100\ \mu\text{m}$ on the individual hit, while the timing resolution is $\approx 1\ \text{ns}$.

2.3.4 TOP

The TOP detector is composed of 16 modules that cover the barrel surface between the outer CDC wall and the ECL support frame (θ range from 31° to 128°). Each module is made of a $2.4\ \text{m} \times 45\ \text{cm} \times 2\ \text{cm}$ quartz bar that acts as Cherenkov radiator, with a focusing spherical mirror at one end, and an expansion prism at the other. On the large end of the expansion prisms is an array of micro-channel plate photomultipliers (MCP-PMTs). This is shown in fig. 2.10.

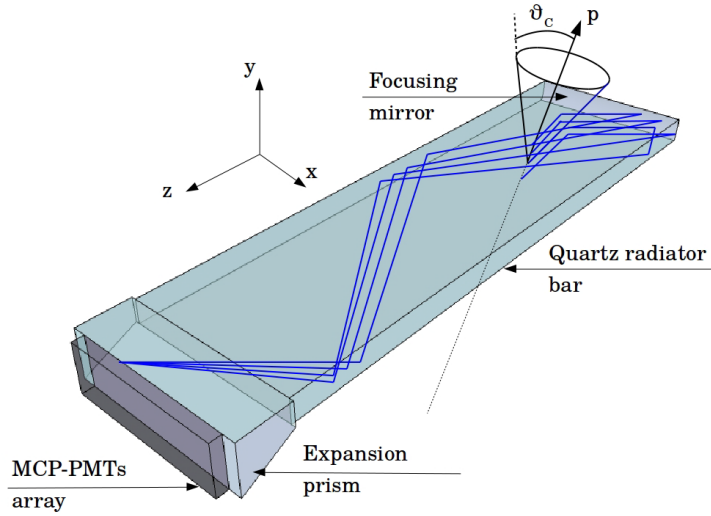


Figure 2.10: Schematic view of a TOP counter.

Particles crossing the quartz bar produce Cherenkov photons at an angle θ_C with respect to the direction of the particle. These photons propagate to the MCP-PMTs via total internal reflection, which conserves the ring image produced by θ_C ; the expansion prism is used to expand this image. The MCP-PMTs are able to reconstruct three-dimensional images of the rings using the (x, y) spatial coordinates of the array (resolution of $\mathcal{O}(1 \text{ mm})$) and the photon timing information (resolution of $\mathcal{O}(0.1 \text{ ns})$).

The main task of the TOP detector is to improve the K/π separation up to $3.5 \text{ GeV}/c$ of momentum.

2.3.5 ARICH

The ARICH disc covers the forward endcap in the θ range from 14° to 30° (inner radius 87 cm, outer radius 228 cm). It is made of a 2 cm thick aerogel Cherenkov radiator and an array of photodetectors, separated by a 20 cm thick expansion volume for the Cherenkov rings, as shown in fig. 2.11.

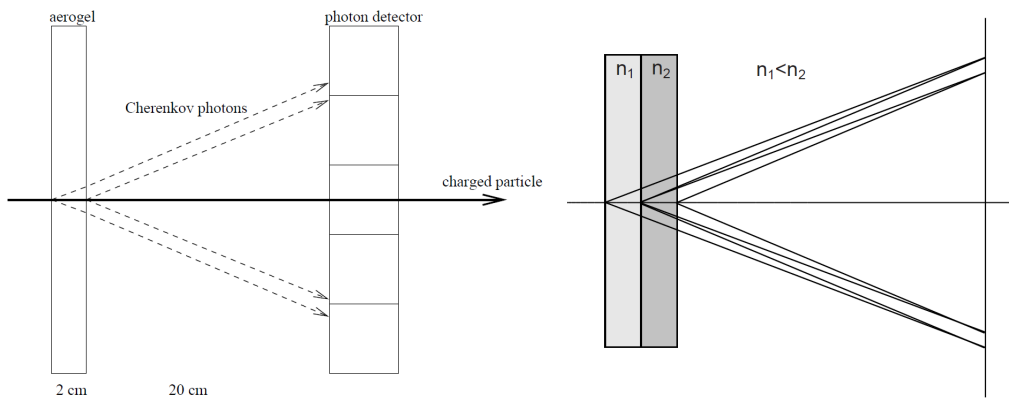


Figure 2.11: Schematic view of the ARICH (left). Focusing configuration of the ARICH radiator (right).

The Cherenkov radiator is made of two layers of aerogel with slightly different refractive indices ($n_1 = 1.046$ and $n_2 = 1.056$): this allows to focus Cherenkov photons on the photodetectors (fig. 2.11), while the larger thickness increases the photon yield, thus improving the resolution of the Cherenkov angle θ_C .

The photodetectors are based on the hybrid avalanche photodetector (HAPD) technology: on one end of a vacuum tube is a photocathode, where photons generate electrons through photoelectric effect; on the other end, at a potential difference of $\mathcal{O}(10\text{ kV})$, is a 12×12 grid of avalanche photodiodes (APDs). The electric field and the photodiodes provide the required gain factor. Each APD is $4.9\text{ mm} \times 4.9\text{ mm}$. There are 540 HAPDs arranged in 9 concentric rings [18].

The ARICH is designed to improve K/π separation up to $4\text{ GeV}/c$ of momentum, and $e/\mu/\pi$ separation under $1\text{ GeV}/c$ by directly reconstructing Cherenkov rings from the two-dimensional information of the HAPDs [20].

2.3.6 ECL

About $1/3$ of the B meson decays produce photons in the range from 20 MeV to 4 GeV , thus an ECL with high resolution and efficiency is necessary. The Belle II ECL reuses the CsI(Tl) crystals of the Belle ECL, but with a major upgrade of the readout electronics.

CsI(Tl) crystals emit about 5000 photons per MeV, with a noise level of 200 keV and a decay constant of $1.3\text{ }\mu\text{s}$. The crystals have many different shapes, with an average cross section of $6\text{ cm} \times 6\text{ cm}$ and a thickness of 30 cm ($16.1X_0$). The lateral size is comparable to the Moliere radius, and the thickness prevents significant energy loss for photons up to several GeV.

Two photodiodes, with a sensitive area of $1\text{ cm} \times 2\text{ cm}$ each, are glued to the back of each crystal. The two outputs are shaped with different time constants: $0.2\text{ }\mu\text{s}$, used to generate trigger signals, and $0.5\text{ }\mu\text{s}$, used to extract amplitude and time information through waveform sampling.

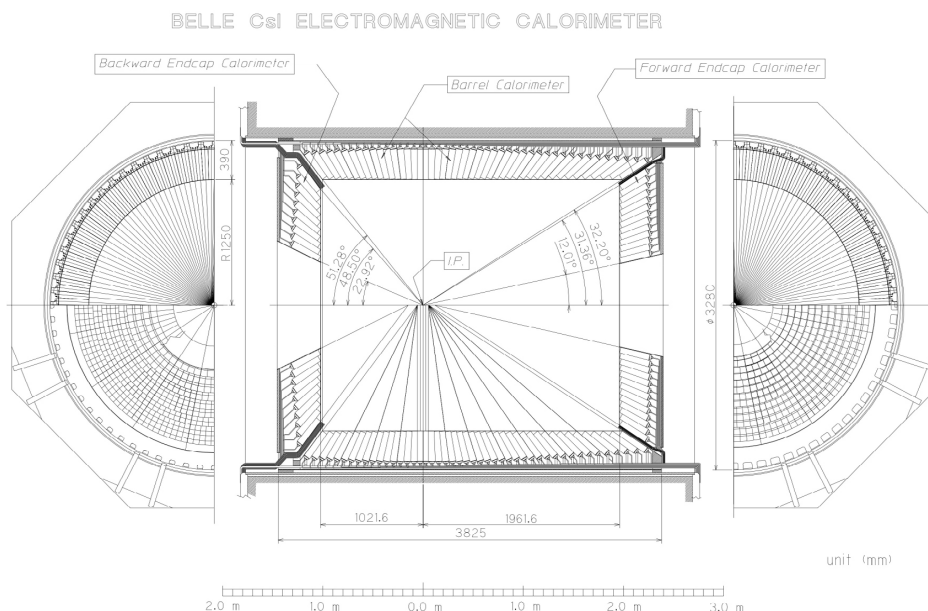


Figure 2.12: Schematic view of the ECL. Taken from [20].

ECL is made of 8736 crystals, arranged in a 3 m long barrel section with an inner

radius of 1.25 m, and two endcap discs located at 2 m (forward) and 1 m (backward) from the IP. This layout, shown in fig. 2.12, covers the θ range from 17° to 150° (like PXD, SVD and CDC), except for two $\approx 1^\circ$ gaps between the barrel and the endcaps.

Aside from efficiently detecting photons and precisely measuring their energy and angular coordinates, ECL is also used for electron identification, trigger signal generation, luminosity measurement and, together with KLM, K_L^0 detection.

The energy resolution of ECL is better than 5 % for photons above 20 MeV of energy.

2.3.7 KLM

KLM consists of several layers of active detector elements separated by iron plates, located outside the volume of the solenoid. The iron plates provide $3.9\lambda_i$ (where λ_i indicates an interaction length) of material, in addition to the $0.8\lambda_i$ of ECL, where a K_L^0 can shower hadronically; they also double as return yoke for the magnetic flux of the solenoid, and were reused from Belle.

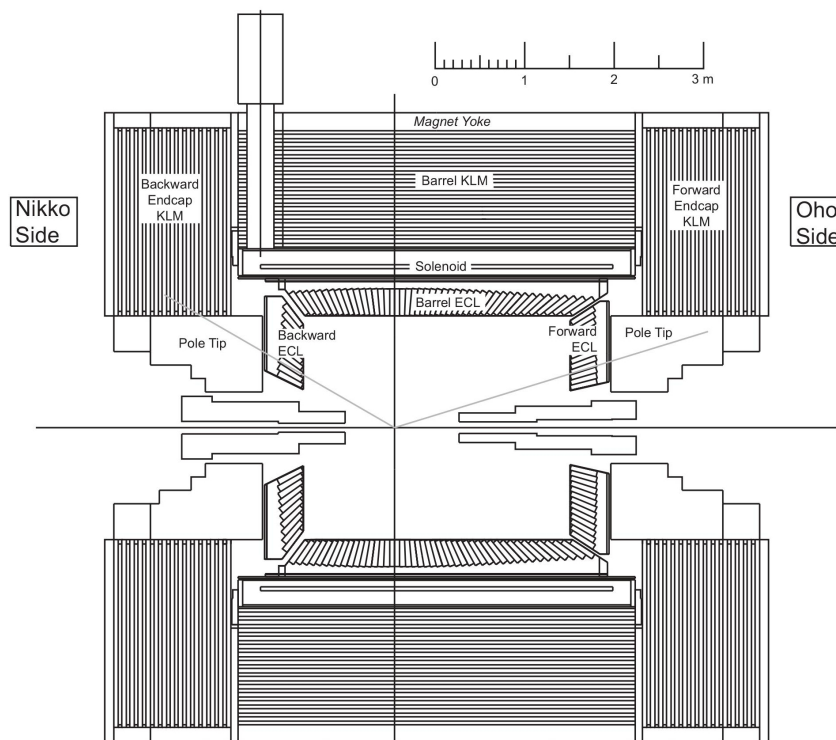


Figure 2.13: Schematic view of the KLM. The nominal acceptance is given by the gray lines. Taken from [18].

In the barrel region (see fig. 2.13) there are 15 layers of detector and 14 iron plates, while in the endcap regions there are 14 layers of detector and 14 iron plates. For the outermost active layers of the barrel region, resistive plate chambers (RPCs) from Belle were reused; however, for the two innermost layers of the barrel region and for the endcap regions, where the dead time of the RPCs would be too long to cope with the increased background rate, scintillator bars with silicon photomultipliers (SiPMs) were used. In the endcap regions, most of the background is due to the neutrons produced by radiative Bhabha scattering outside of the detector volume (see section 2.2.1).

RPCs are made by two high-resistivity glass electrodes separated by a 2 mm gap filled with a gas mixture (62% HFC-134a freon, 30% argon, 8% butane); a carbon-doped paint on the outer side of the glass allows to generate a uniform 4.3 kV/mm electric field in the gas gap. A thin insulator layer separates the glass from 5 cm wide copper strips, that are used to read the signal induced by charged particles when they ionise the gas in the gap; a layer of dielectric foam separates the copper strips from the external ground plane, forming a $50\ \Omega$ transmission line. Two RPCs are coupled by an insulator layer to form a superlayer: by using orthogonal copper strips, two-dimensional information can be retrieved. This is shown in fig. 2.14.

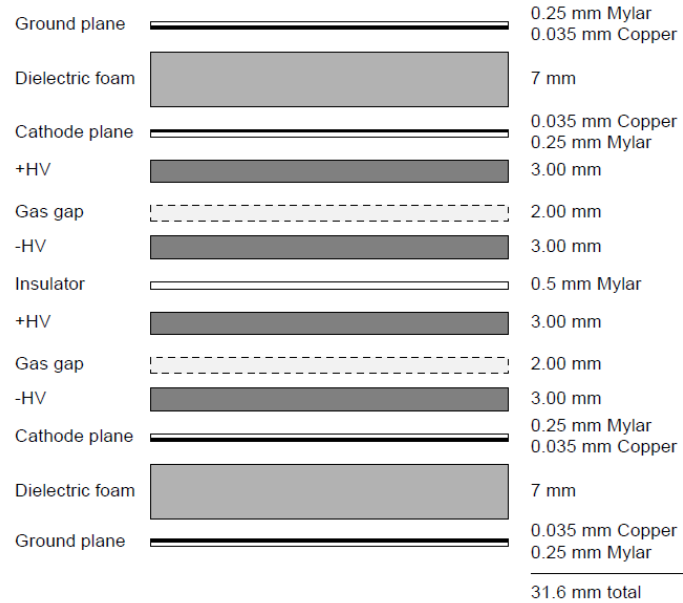


Figure 2.14: Schematic cross section of a KLM RPC superlayer [18].

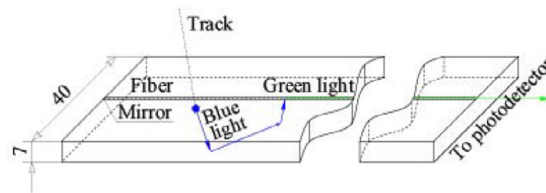


Figure 2.15: Schematic view of a KLM scintillator [20].

Scintillator bars with a cross section of 7–10 mm \times 40 mm are equipped with a groove in the center, where a wave-length-shifting optical fibre is placed to pick up the scintillation light and carry it to the SiPMs (see fig. 2.15). SiPMs have a good time resolution of ≈ 0.7 ns, allowing a precise measurement of the time of flight of K_L^0 mesons.

Charged particle tracks are extrapolated from CDC to KLM under the π and μ hypotheses: if a KLM hit is close enough to a track, it is associated with it. If the predicted range (outermost layer reached) for the track differs significantly from the observed range, the particle is classified as hadron.

The remaining hits are grouped in KLM clusters of 5° radius. ECL and KLM cluster are associated based on their proximity in angular coordinates; clusters crossed by a

charged particle track are assumed caused by the charged particle; a neutral particle is assumed if there are at least two clusters (either in ECL and KLM, or in different modules of ECL or KLM), and a K_L^0 is assumed over a photon if there is at least one cluster in KLM.

KLM covers the θ region from 20° to 155° . The μ detection efficiency is $\approx 89\%$ (for momenta above $1\text{ GeV}/c$), while the K_L^0 detection efficiency is $\approx 80\%$ (for momenta above $3\text{ GeV}/c$); the contamination from hadrons is only $\mathcal{O}(1\%)$.

2.3.8 Trigger system

The Belle II trigger system needs to apply efficient selections of physics-interesting events while rejecting background. In order to do this it must satisfy the following requirements:

- it must select interesting events from $\Upsilon(4S) \rightarrow B\bar{B}$ and from continuum with nearly 100% efficiency;
- it must have an average trigger rate below 30 kHz (limited by the maximum data acquisition rate);
- it must have a fixed latency within 5 μs (limited by the buffer depth of the sub-detectors' readout electronics) and a timing accuracy better than 10 ns.

Tab. 2.5 summarises the cross sections and trigger rates that are expected at design luminosity. Bhabha and $\gamma\gamma$ events are used to measure luminosity.

| Process | σ [nb] | Trigger rate [Hz] |
|--|---------------|-------------------|
| $\Upsilon(4S) \rightarrow B\bar{B}$ | 1.2 | 960 |
| Continuum $q\bar{q}$ | 2.8 | 2200 |
| $\mu^+\mu^-$ | 0.8 | 640 |
| $\tau^+\tau^-$ | 0.8 | 640 |
| Bhabha ($\theta \geq 17^\circ$) | 44 | 350* |
| $\gamma\gamma$ ($\theta \geq 17^\circ$) | 2.4 | 19* |
| Two-photon ($\theta \geq 17^\circ, p_T \geq 0.1\text{ GeV}/c$) | ~ 80 | $\sim 15\,000$ |
| Total | ~ 130 | $\sim 20\,000$ |

Table 2.5: Expected cross sections and trigger rates for different processes at the design luminosity of $8 \times 10^{35}\text{ cm}^{-2}\text{s}^{-1}$. Trigger rates with a * are prescaled by a factor 1/100 due to the large cross section. Taken from [18].

Hadronic events (from both $B\bar{B}$ and continuum) are characterised by a large track multiplicity, thus a trigger can select them by requiring a minimum number of tracks. Low-multiplicity events (e.g. τ decays, dark sector particles decays, etc.) are harder to discriminate from background, as they often contain only zero or two tracks; also, they often have topologies similar to Bhabha or $\gamma\gamma$ events, which are suppressed by the prescaling, causing a loss of trigger efficiency.

The Belle II trigger performs the selection in multiple steps, and can be divided in two parts: the level 1 (L1) trigger, which is hardware-based, and the high-level trigger (HLT), which is software-based and is implemented in the data acquisition (DAQ) system.

L1 trigger A summary of the L1 trigger pipeline is given here.

- Several sub-trigger systems collect and process information from one subdetector each:
 - the CDC sub-trigger consists of a 2D-trigger that uses track information in the (r, ϕ) plane, and of a 3D-trigger that uses the z information to discard background tracks that did not originate from the IP;
 - the ECL sub-trigger uses the total energy deposit to detect events with high electromagnetic energy deposit, and the cluster information to detect both hadronic events that produce large numbers of clusters, and Bhabha/ $\gamma\gamma$ events that have a back-to-back topology;
 - the TOP sub-trigger provides precise timing and hit topology information;
 - the KLM sub-trigger is used to select $\mu^+\mu^-$ events, and to measure the efficiency of other sub-triggers with respect to low-multiplicity events.
- The output of the sub-triggers is used by the global reconstruction logic (GRL) to perform a low-level reconstruction.
- The output of the GRL is used by the global decision logic (GDL), which sends the appropriate trigger signal if the event passes its selection criteria; it also applies the appropriate prescaling if needed.

The L1 trigger components are implemented using field programmable gate arrays (FPGAs), logical integrated circuits that can be reconfigured (“programmed”) in-place, without physically accessing them. This allows the L1 trigger to have a short and fixed latency (around $5\ \mu\text{s}$). The uncertainty on the L1 trigger timing is $\approx 10\ \text{ns}$, and is referred to as trigger jitter.

HLT The HLT uses the full event data from all subdetectors (except PXD) to fully reconstruct events that pass the L1 trigger selection; thanks to the full reconstruction, HLT can take decision based on the physics of the event. HLT uses the same offline reconstruction software used for performing analyses, and its selection process can be divided in two steps.

- The level 3 (L3) trigger applies a first cut on track multiplicity, vertex position and total ECL energy deposit; this is done after the first steps of the standard track and cluster reconstruction (based on CDC and ECL data only), and is aimed at reducing the average reconstruction time by discarding about 1/2 of the events as soon as enough information is available to take this decision.
- The physics-level selection is performed after the remaining steps of the standard reconstruction are completed, and uses the same selection criteria used for the *skims* (i.e. the pre-filtered datasets that are used as input for the various analyses); the fact that the same software and selections are used for offline analyses allows to avoid systematic uncertainties from the online selection.

After both steps, the number of events is reduced to about 1/8.

Until the HLT decision is available, PXD data (for events that pass the L1 trigger) is stored in the dedicated online data reduction system (ONSEN), a 5-seconds FPGA-based hardware buffer that also performs zero-suppression. Once an event passes the selection, HLT extrapolates the tracks found by CDC and SVD to the layers of PXD,

and defines regions of interest (ROIs) around the intercepts; ROIs are then passed to the ONSEN system, which proceeds to transmit only the hits within such regions to the DAQ system: this is necessary to limit the PXD data size to ≈ 100 kB/event.

2.3.9 Software framework

The Belle II Analysis Software Framework (BASF2) is used for almost every task of the experiment: data acquisition, Monte Carlo samples generation and simulation, particle reconstruction, physics analysis, and storage of all kinds of information, from the raw detector data to the high-level variables of the results of the analyses [21]; only the latest steps of the analyses, e.g. histogram plotting and fitting, are usually performed “offline” (i.e. without BASF2).

The core of BASF2 is written in C++ to minimise execution time and memory usage, but it also has a Python 3 interface to allow simpler user control. The software is organized in *modules*, pieces of software that execute a specific and configurable task (e.g. reconstruction of a particle from its daughters). The workflow for a specific task is configured in a Python script called *steering file*, which creates a *path*, i.e. a sequence of configured instances of modules, and repeats the sequence for each input event (either generated or read from a file or the detector). For each event, the modules output is written to a common *data store* so that subsequent modules can use it as input; specific modules exist to read/generate events and to write data to file.

Detector information (e.g. geometry data, configuration parameters, calibration constants, etc.) is stored in the *conditions database* in objects called *payloads*. Payloads may have different revisions (e.g. calibration constants may change over time), which are associated to specific runs so that the software always uses the appropriate configuration when processing an event.

BASF2 also uses third-party software such as ROOT [22] for data handling and storage, EvtGen [23] for generating $B\bar{B}$ events and GEANT4 [24] for simulating the interaction of particles with the detector.

More detailed information about simulation and reconstruction in BASF2 is provided in the relevant sections.

Chapter 3

SVD and future upgrades

In this chapter, a more in-depth description of SVD is given; an overview of some of the proposed VXD upgrades is then provided, focusing on those that are characterised later on in this thesis; finally, simulation and tracking in BASF2 are briefly described, as they are key ingredients of the upgrade characterisation.

3.1 Detailed description of SVD

Section 2.3.2 provides a quick overview of SVD. This section is a much more detailed description: first, the characteristics of the single sensors are described; then, the geometry of SVD is presented; finally, the diamond radiation sensors, used for protecting the detector from large beam losses and for measuring the dose rate, are described. A three-dimensional picture of SVD is shown in fig. 3.1.

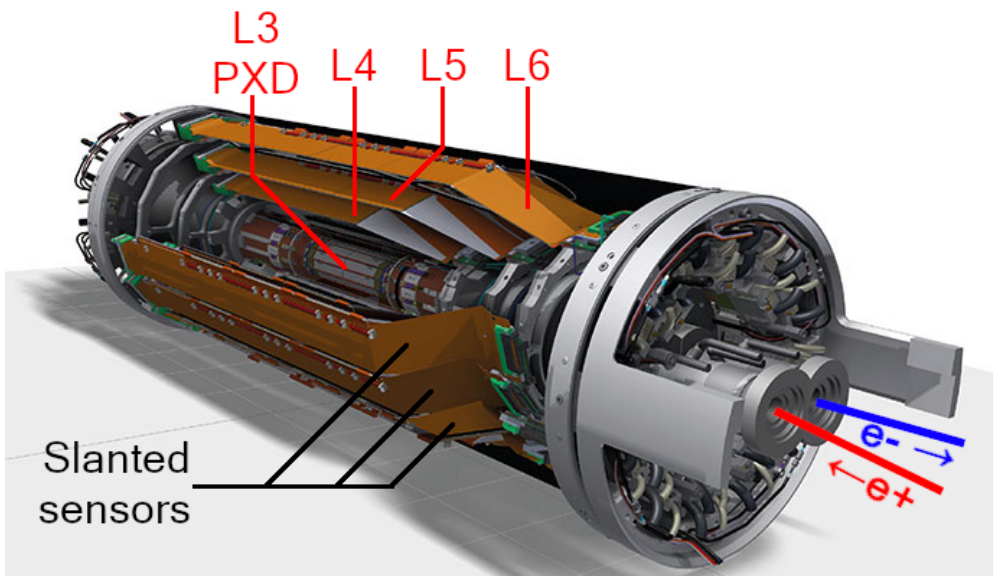


Figure 3.1: A pictorial 3D view of SVD, PXD and the beam pipe.

3.1.1 Sensors

In order to provide precise track information while keeping the material budget and the number of readout channels low, SVD uses sensors based on the double-sided silicon strip detector (DSSD) technology. SVD sensors are made of an n -type silicon substrate with p^+ strips implanted on one side, and orthogonal n^+ strips implanted on the other side (fig. 3.2). The sensitive or *active* volume of the sensors is the *depletion* or *space charge region* that develops at the p - n junction, which is also the volume where an electric field is present [25], as explained later; a reverse bias voltage of $\mathcal{O}(100\text{ V})$ is applied between p and n strips in order to extend this depletion region to the volume of the whole substrate. When a charged particle crosses the substrate, it generates electron-hole (eh) pairs; electrons and holes drift to the n and p strips, respectively, due to the electric field, inducing a current in the strips themselves; this can be measured by the readout electronics through AC-coupled connections, which are formed by aluminum strips placed above the p and n strips, and insulated from them by a layer of silicon oxide (SiO_2). To improve the resolution without increasing the number of readout channels, an intermediate floating strip is placed between two readout strips: the signal induced in the floating strip is shared between the neighbouring readout ones.

A p - n junction is an interface between two oppositely-doped semiconductors: since the p -doped silicon has an excess of holes and the n -doped silicon has an excess of electrons, the excess carriers of each part migrate to the other and recombine; opposite net charge densities form on the two sides, generating an electric field that, eventually, stops the migration; the region with the electric field is called depletion region, as it has almost no charge carrier, and is larger on the less-doped side (in SVD sensors, the substrate). In SVD sensors, the depletion region forms between the p strips and the n -type substrate; the reverse bias voltage allows further charge carriers to migrate from the edges of the depletion region, thus causing the depleted volume to expand until the whole substrate is depleted: at this point the only charge carriers in the substrate are the eh pairs generated by the charged particles, which allow their detection.

The SiO_2 layer contains fixed positive charges because they are trapped either during fabrication, or after being produced by radiation damage; these positive charges attract electrons forming an e^- *accumulation layer*, which effectively short-circuits the n strips. To avoid this, a p -type implant, called a p *stop*, is put between two n strips: p stops introduce p - n junctions that drive electrons away with their depletion regions, effectively insulating n strips (at least, when a sufficient bias voltage is applied and the substrate is fully depleted) [26].

Sensor types SVD uses three different types of sensors to cover the surface of its four layers:

- small rectangular sensors for the innermost layer (L3), produced by Hamamatsu Photonics (“HPK small” sensors);
- large rectangular sensors for the outermost layers (L456), also produced by Hamamatsu Photonics (“HPK large” sensors);
- trapezoidal sensors for the forward region of the outermost layers (L456), produced by Micron (“Micron” sensors).

Fig. 3.3 shows the sizes of each type of sensor, while the main characteristics are summarised in tab. 3.1.

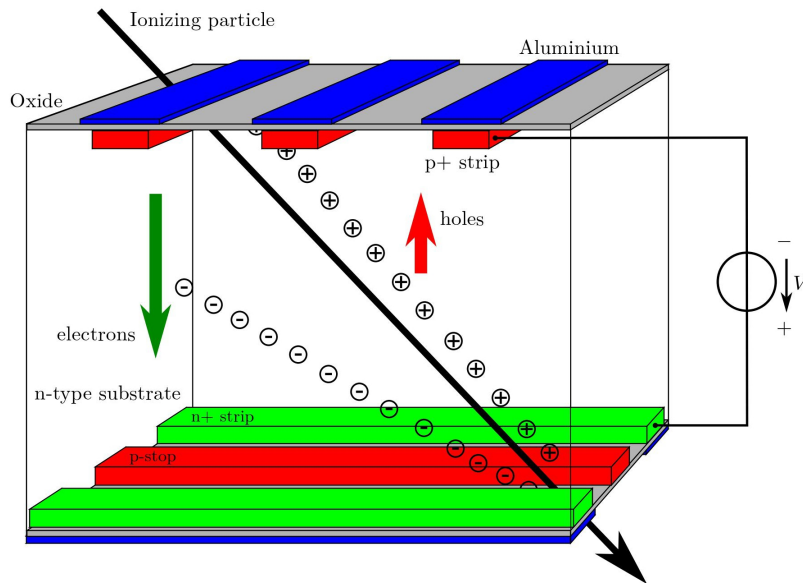


Figure 3.2: Schematic view of a DSSD sensor crossed by a charged particle. Taken from [26].

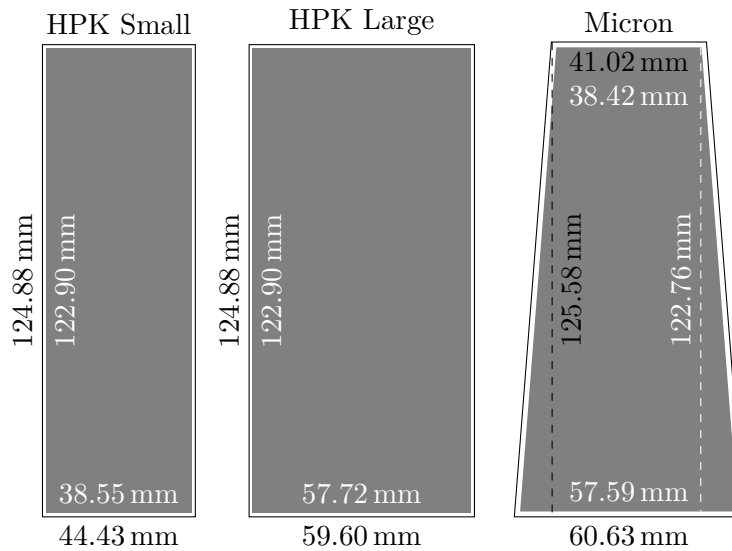


Figure 3.3: The dimensions of the three types of DSSD used in SVD and their active area (to scale).

The p strips allow to read the local u coordinate, which corresponds to ϕ at first order; the n strips allow to read the local v coordinate, which corresponds to z for HPK sensors, and to a linear combination of z and r for slanted Micron sensors (fig. 3.4 and 3.6).

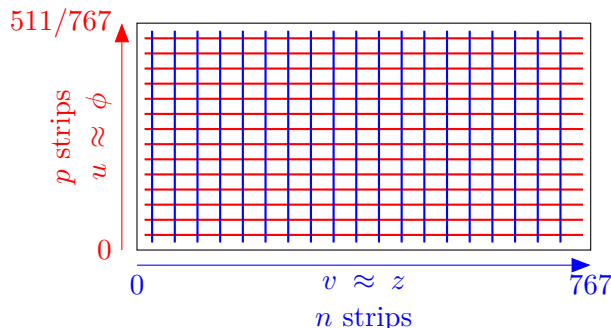


Figure 3.4: Local coordinates and strip numbering in SVD sensors.

| | HPK Small | HPK Large | Micron |
|--|-----------|-----------|----------------|
| N. readout $p/u/\phi$ strips | 768 | 768 | 768 |
| N. readout $n/v/z$ strips | 768 | 512 | 512 |
| $p/u/\phi$ readout pitch [μm] | 50 | 75 | 75 to 50 |
| $n/v/z$ readout pitch [μm] | 160 | 240 | 240 |
| Width [mm] | 124.88 | 124.88 | 125.58 |
| Height [mm] | 40.43 | 59.60 | 60.63 to 41.02 |
| Area [mm^2] | 5048.90 | 7442.85 | 6382.60 |
| Active area [mm^2] | 4737.80 | 7029.88 | 5890.00 |
| Thickness [μm] | 320 | 320 | 300 |
| Depletion voltage [V] | 40 to 60 | 40 to 60 | 20 to 40 |

Table 3.1: Summary table of the main features of the three types of DSSD used in SVD. All sensors have one intermediate floating strip between two readout strips [18, 15].

Readout electronics For the readout the APV25 chip, originally developed for the tracking detector of CMS, was chosen; it contains low-noise preamplifiers and shapers for 128 channels, and has a shaping time of 50 ns, crucial to minimise the hit occupancy due to the high particle rate from beam-induced background. L3 sensors (HPK small) need 12 chips, while L456 sensors (HPK large and Micron) only need 10.

For forward and backward sensors, the chips are mounted on readout boards called *hybrid sandwiches*, which are placed at one end of the sensor, outside its active area. For central sensors of L456, the chips are glued on flexible circuits called *origami*, which are placed on top of each sensor to minimise the length of the cable connected to the preamplifier input, as it determines the load capacitance which is the dominant source of noise; a 1 mm layer of Airex foam acts as thermal and electrical insulator between the sensor and the circuit. A planar fan-out connects the strips on the top side to the chips, while the strips on the bottom side use a flexible pitch adapter (similar to the origami) wrapped around the edge of the sensor (see fig. 3.5).

Having all the chips on one side of the sensors allows to use a single cooling pipe for the APV25 chips of each layer, minimising the material budget. A two-phase CO_2

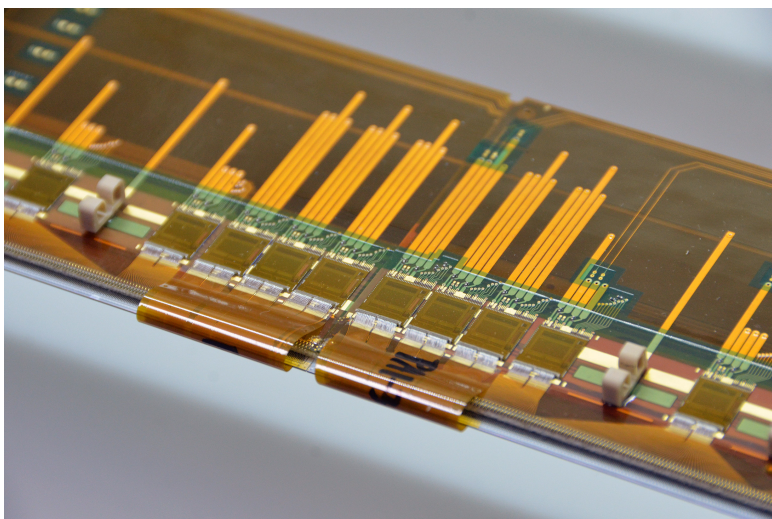


Figure 3.5: Detail showing the origami flexible circuit, with the p -side strip pitch adapters wrapped around the edge of the sensor [15].

cooling system is used with $100\ \mu\text{m}$ thick cooling pipes, limiting the average material budget per layer to about $0.7\%X_0$. L3 only has chips at its ends, thus it does not need the cooling pipe over the sensors, in the acceptance area [27].

The APV25 chips sample the signal waveform of each strip with a sampling frequency of $31.805\ \text{MHz}$ (every $t_s \approx 31.45\ \text{ns}$), obtained by dividing the accelerator RF ($508.887\ \text{MHz}$) by 16. Each channel stores the samples in a ring buffer with 192 cells, so each sample is stored for about $6\ \mu\text{s}$. Since the collisions are not synchronized to the APV25 clock, the samples stored do not correspond to the peak of the signal waveform, hence the chips must be operated in *multi-peak* mode: when an L1 trigger signal is received ($\approx 5\ \mu\text{s}$ after the event), external fast analog-to-digital converters (FADCs), synchronized with the APV25 clock, process six samples per channel per event, which are then used to reconstruct the peak amplitude and the hit time of the waveform. The 10 bit FADCs perform common-mode subtraction, pedestal subtraction, and zero suppression; the latter consists in recording only the hits with a minimum signal-to-noise ratio (SNR), which is set to 3.

The possibility to read only three samples instead of six, further reducing the acquisition window at least in some events with small trigger jitter, has been studied: in case the trigger rate or occupancy increase above a certain limit, this would allow to reduce the data size and the necessary bandwidth. The samples closer to the waveform peak would be chosen.

Strips with a SNR above 5 are considered *hits*; if there are adjacent strips with a SNR above 3, they are grouped with the hit forming a *cluster*. Each cluster is assigned a position in the sensor's local coordinate: clusters with a single strip are assigned the coordinate of the centre of the strip, while for clusters with multiple strips a weighted average is used (the deposited charge used as weight). The position and total deposited charge of each cluster is used for tracking; the cluster charge and track direction are then also used to estimate the energy loss dE/dx , used for particle identification [7, 18].

3.1.2 Geometry and layout

The four layers of SVD are organized in ladders, which are flat support frames for a row of 2 to 5 sensors, their readout electronics, and the cooling pipe. Each layer has a different ladder design and number of ladders.

- L3 has 7 planar ladders with two HPK small sensors; the readout electronics is placed at each end of the ladder, thus there is no cooling pipe in the acceptance region above the sensors.
- L4/L5/L6, respectively, have 10/12/16 ladders with two/three/four HPK large sensors and one Micron sensor; the latter is placed on the forward side, and is tilted towards the z axis by $11.9^\circ/17.2^\circ/21.1^\circ$ (thanks to its trapezoidal shape); the readout electronics for the backward and forward sensors is placed at each end of the ladders, while that for the central sensor is placed on the origami above the sensor itself, thus requiring a cooling pipe to pass in the acceptance region.

A schematic view of the layout is shown in fig. 3.6.

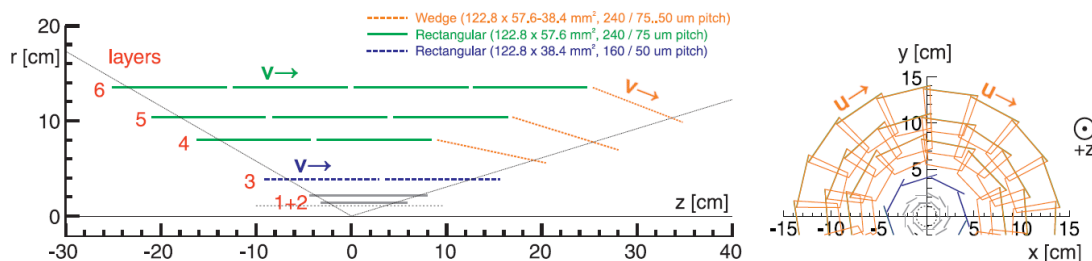


Figure 3.6: Schematic of the SVD layout. Local coordinates are shown for a few sensors.

Sensors are numbered $La.b.c$, where a is the layer number, b is the ladder number and c is the sensor number; ladders within each layer are numbered from 1, starting from the one closer to $\phi = 0$ and proceeding by increasing ϕ ; sensors within each ladder are numbered from 1, starting from the forward one and proceeding backwards.

Ladders L3.1 and L3.2 ($\phi = -18^\circ$ and 34° , respectively) are called *mid-plane ladders*, and are found to be exposed to a larger amount of radiation than the rest of L3 ($\approx 50\%$ more, details in chapter 4).

3.1.3 Diamond radiation detectors and beam-abort system

The radiation monitor and beam abort (RMBA) system is required to fulfil two tasks:

- issuing an immediate beam-abort signal to SuperKEKB when excessive beam losses, which may damage VXD sensors and electronics, are detected;
- constantly monitoring and recording the radiation doses in the VXD volume.

The measurement is performed with radiation sensors based on artificially grown diamonds, which are biased at 100 V; when a particle crosses the diamond's bulk, it generates eh pairs, which induce a current in the bias circuit: the current is proportional to the dose rate, with an average sensitivity of 35 mrad/s/nA. The sensitivity and pedestal vary significantly among diamonds, hence an extensive calibration was performed.

A total of 28 diamonds are placed on different points of the VXD support frame, as shown in fig. 3.7. A total of eight diamonds are placed on the final-focusing quadrupole magnets (QCS), four on the backward (BW) side and four on the forward (FW) side; twelve diamonds are placed on the support cones of the outer SVD layers (six BW, six FW); finally, eight diamonds are placed on the beam pipe (BP), close to the interaction point and the PXD support structure (four BW, four FW). The naming convention for these diamonds is also shown in fig. 3.7.

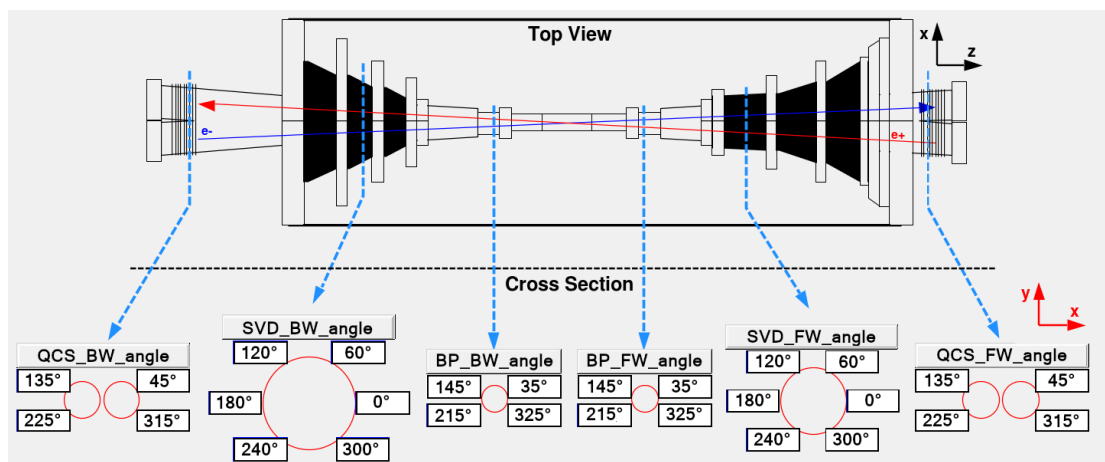


Figure 3.7: Schematic of the RMBA diamonds placement. The diamond names are shown, where “angle” must be replaced with the ϕ placement angle in degrees (also shown).

The diamonds are powered and read by seven diamond control units (DCUs), FPGA-based boards placed outside the detector. These are able to communicate with the slow-control network (responsible for data recording and online display) via an Ethernet interface, but are independent of it; they also send hardware abort signals to SuperKEKB, and receive abort confirmation signals from it.

The DCUs read the diamonds’ currents with 16 bit ADCs via a trans-impedance amplifier, at a sampling frequency of 50 MHz. Three ranges can be selected for current measurement: 36 nA, 9 μ A and 4.5 mA, roughly corresponding to 1.3 rad/s, 0.3 krad/s and 0.16 Mrad/s, respectively. The first range is suitable for precisely monitoring the typical, relatively small beam losses observed during operations; the last range is used for beam-abort, as it avoids saturation when large radiation spikes are delivered.

Running sums of 125 samples are stored at 400 kHz in a large data buffer; these sums are used as input for the programmable logic deciding whether to issue an abort signal; after an abort confirmation is received, sampling is stopped and the data buffer is recorded for post-abort analyses of the beam losses. Also running sums of 5×10^6 samples are produced at 10 Hz and sent to the slow-control network; slow-control software records these values after converting ADC units to dose-rate units and subtracting pedestals [15, 28, 29].

3.1.4 Environmental monitoring

Aside from radiation, two more VXD environment parameters are monitored: temperature and humidity.

Temperature is measured using fibre-optics sensors (FOS) and negative temperature coefficient (NTC) thermistors, placed on the cooling pipes at their inputs and outputs, and over some readout chips; if the temperature is found to be outside a certain range, an issue with the cooling system is assumed and an hardware signal is issued to the interlock system, stopping operations and turning off VXD power supplies to prevent damage.

Temperature sensors cannot, however, be used to measure or estimate the temperature of single SVD sensors; this makes it impossible to accurately evaluate certain effects, e.g. radiation damage annealing (more about this in chapter 4).

The residual humidity in the dry-nitrogen atmosphere of VXD is measured through a series of “sniffing pipes”. If humidity raises above a certain level, the frost point would reach the cooling pipe temperature, resulting in water condensing on the cooling pipes and the electronics; to avoid this situation, if humidity raises above a safety threshold an hardware signal is issued to the interlock system, stopping operations and turning off the CO₂ cooling system to increase the temperature.

The hardware interlock system of VXD is independent of slow-control, as it must be able to perform a fast but orderly shutdown of PXD and SVD at any time [15].

3.2 Proposed VXD upgrade: VTX

Since the beginning of operations in 2019, Belle II has shown good performance; despite this, large backgrounds are present, and projections show that several subdetectors will limit the beam currents in the future (e.g. the drift chamber, due to discharges and high occupancy, and the TOP, due to radiation damage of its photomultipliers), unless background is further reduced. While PXD and SVD are not the most critical subdetectors, simulations show that they would approach their occupancy limit (3 %) at nominal luminosity (more about this in section 4.4). In addition, in a few cases accidental beam losses have caused localised damage in the PXD sensors and readout electronics, implying the possibility of progressive performance deterioration from radiation bursts.

Since a long shutdown (about nine months) is planned around 2026 for accelerator improvements, several upgrade proposals are under study for the various subdetectors: this thesis presents a benchmark study for one the proposed upgrades of the VXD, called VTX.

VTX should replace the current VXD (both PXD and SVD) with a five-layer (or more, see section 3.2.2) monolithic pixel detector based on the commercial, fast and precise CMOS pixel technology; this should bring several advantages:

- better background tolerance, thanks to the smaller occupancy resulting from the smaller sensor element area (much smaller than that of SVD) and the shorter integration time (much shorter than that of PXD);
- low readout bandwidth, tanks to on-chip sparsification (CMOS pixel technology allows to fabricate part of the readout electronics directly on the sensors); this also results in a smaller material budget from data cables;
- availability of all layers (including the innermost ones) as HLT inputs, resulting in increased track finding efficiency, particularly at low transverse momentum (down to $\approx 50 \text{ MeV}/c$); in addition, it may be possible to incorporate VTX sensors in the L1 trigger decision.

- possibility to achieve final resolution already at HLT level (currently, HLT never uses the PXD data);
- simpler operation, with no need for gated mode or data reduction (ROI selection) like for PXD;
- unified control system for the whole vertex detector;
- fewer services and simpler detector integration, allowing to further reduce material budget and also to make room for extra shielding in the interaction region and final-focus QCS magnets region;
- simplified tracking chain, with the possibility to use the more natural inside-out tracking;
- improved track and vertex resolution, thanks to the smaller pitch of the pixels and the thinner ($\approx 100 \mu\text{m}$) sensors (especially relevant for the outer layers);
- improved ECL resolution, thanks to the reduction of cables and, consequently, electromagnetic showers.

The following sections provide an overview of the CMOS sensors that should be used for the upgrade, and of the proposed geometrical layouts [30].

3.2.1 The upgraded sensors

In order to provide all the aforementioned advantages, the VTX proposal uses depleted monolithic active pixel sensors (DMAPS). Several sensors have been studied as a base for the optimized Belle II pixel sensor (OBELIX), however the TJ-MONOPIX, produced by Tower Jazz and studied for the ATLAS tracker upgrade, seems the most suitable [31].

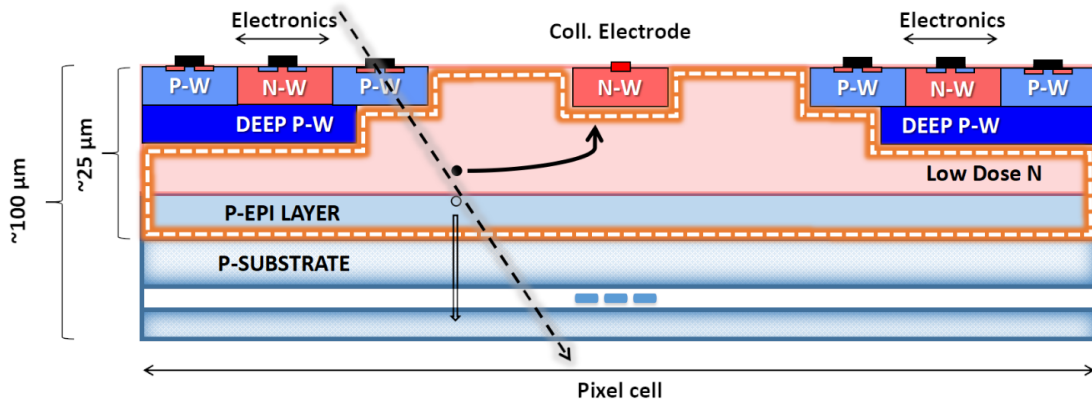


Figure 3.8: Schematic of the TJ-MONOPIX pixel (not to scale). The dashed line indicates the depleted volume. Taken from [31].

A schematic of a pixel is shown in fig. 3.8. The technology employed, similar to that of the standard integrated circuit fabrication, allows thin sensors ($\approx 100 \mu\text{m}$, possibly even less) that include complex circuitry also above the pixels, simplifying the readout implementation. The epitaxial layer ($\approx 20 \mu\text{m}$), which constitutes the majority of the sensitive volume, can be fully depleted, allowing a sizeable charge collection.

The possibility to implement the readout electronics in the sensor die itself, and above the pixels, allows to have fast sensors, with a time resolution of $\mathcal{O}(25\text{ ns})$, that perform in-place zero suppression with a discriminator; also the analog reading can be performed by the discriminator by measuring the time over threshold (ToT). Finally, the data serialization can be performed by in-sensor circuitry outside of the pixel matrix, thus reducing the necessary external electronics to power supplies and cables only.

The TJ-MONOPIX2 prototype has a sensitive area of $16.9\text{ mm} \times 16.9\text{ mm}$, covered by $33\text{ }\mu\text{m} \times 33\text{ }\mu\text{m}$ pixels; it provides hit timestamps with a 25 ns resolution, and has a ToT resolution of 7 bit. Its readout system should be able to efficiently operate with an hit rate of 100 MHz/cm^2 , a factor ~ 5 higher than that expected in L1 of PXD (see section 4.4). The technology and previous prototypes were proven to be able to withstand an equivalent neutron fluence in excess of 10^{15} cm^{-2} . The OBELIX chip is currently under design, with the goal of optimising it for the Belle II application.

3.2.2 The proposed layouts

The base layout of the VTX proposal includes five planar layers, with the innermost L1 at the same radius of PXD's L1, and the outermost L5 at about the same radius of SVD's L6. The two innermost layers (L12) would be made of a light support frame only, relying on dry airflow for cooling; the outermost layers (L345) would, instead, require a more robust carbon fibre support structure and pipes for water cooling. Fig. 3.9 shows a provisional schematic for this layout.

The completely planer ladders allow simpler integration of the outer layers with respect to the lamp-shaped SVD outer layers. Also, the replacement of CO_2 cooling with water cooling would contribute to simplifying operations.

Also other layouts were proposed: six layers with the same radii as the current VXD; seven layers; five layers plus two discs in the forward region (between the three outermost layers, see fig. 3.10). The radii of the layers are reported in tab. 3.2.

| Layout | Radii [mm] | | | | | | |
|--------------|------------|----|----|----|-----|-----|-----|
| | L1 | L2 | L3 | L4 | L5 | L6 | L7 |
| Current VXD | 14 | 22 | 39 | 80 | 104 | 135 | – |
| 5-layers VTX | 14 | 22 | 39 | 89 | 140 | – | – |
| 6-layers VTX | 14 | 22 | 39 | 80 | 104 | 135 | – |
| 7-layers VTX | 14 | 22 | 35 | 60 | 90 | 115 | 135 |

Table 3.2: Radii of the VTX layers in the proposed layouts.

3.3 VXD and VTX simulation

A realistic simulation is a key ingredient for an experiment like Belle II: it is necessary to produce theoretical predictions to be compared with experimental data, but also to validate reconstruction software functionalities (tracking efficiency, uncertainty estimation, ...), to extrapolate backgrounds in future operation conditions, to train machine-learning based algorithms, and also to optimise the detector layout during design. BASF2 includes all the tools needed to perform an accurate simulation of the experiment [1].

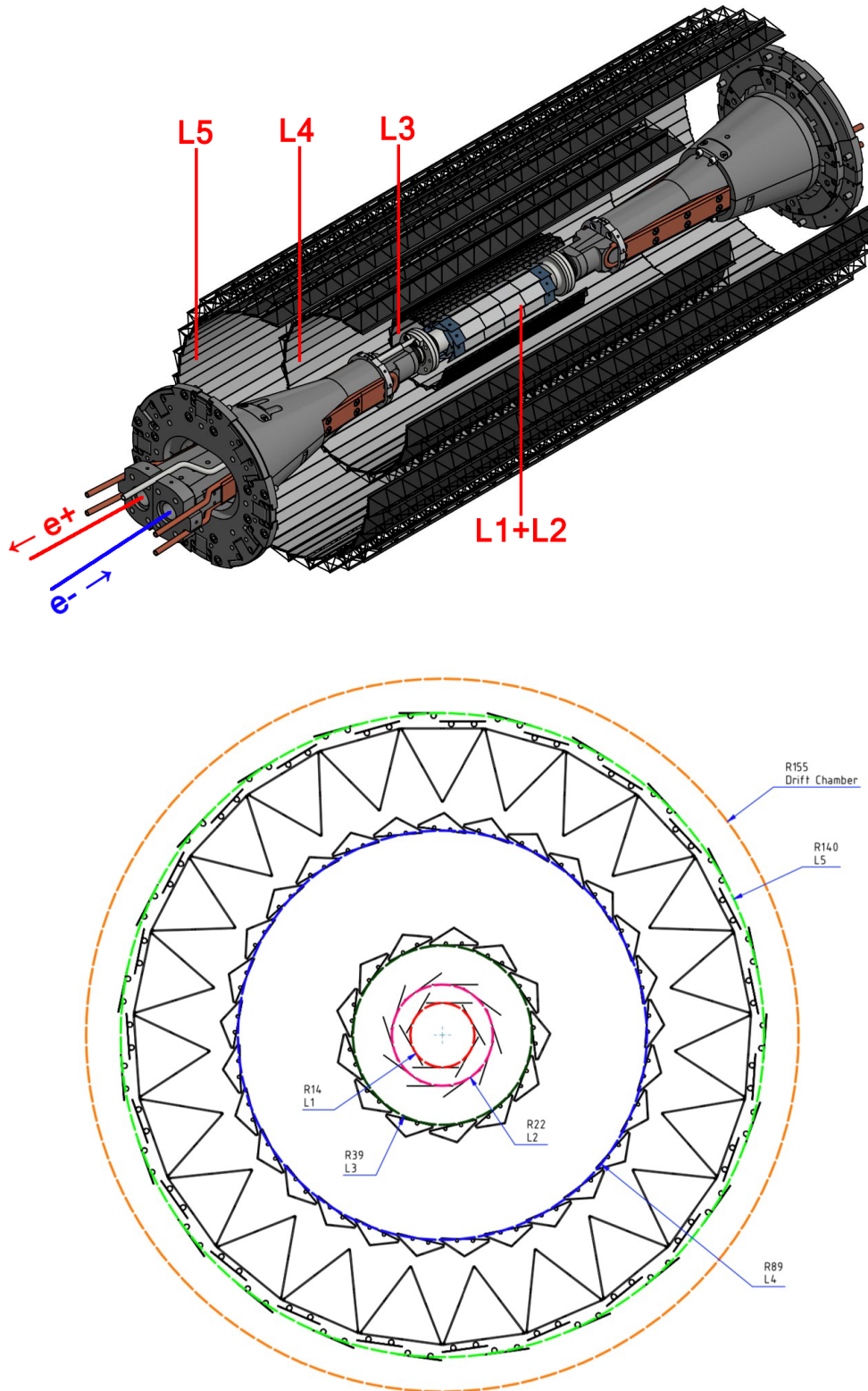


Figure 3.9: Simplified schematics of the 5-layer VTX layout: 3D view (above) and front view (below).

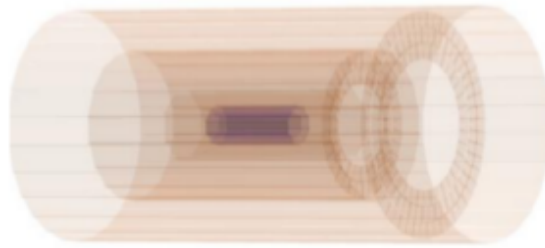


Figure 3.10: Simplified 3D schematic of the 5-layer-plus-discs VTX layout.

Event simulation The e^+e^- events at the interaction point (IP) are produced by a number of different *event generators*: for instance, EvtGen [23] is used for $B\bar{B}$ events, while PYTHIA [32] is used for the continuum production of light quark pairs; other generators are used for τ pair, μ pair, Bhabha scattering and two-photon events, allowing to achieve the best accuracy for each. The output of the generators is used to create a list of Monte Carlo particles (MCParticles), each having its own identity, production vertex, momentum, mother-daughter relationships, etc.

MCParticles are the inputs for later simulation steps; they are also used after reconstruction and analysis for MC truth matching, i.e. to validate the reconstructed event, allowing to study, test and optimise the reconstruction process, the strategy used to reject physics background, etc.

Detector simulation After generating the particles in the event, the response of the detector must be simulated. To this end, the Belle II detector is modelled using the GEANT4 toolkit [24], with a detailed description of both active and passive material of the apparatus (sensors, support structures, services, etc.), as well as an accurate map of the magnetic field. MCParticles are propagated in the magnetic field, and their interactions with the detector material are simulated; GEANT4 also simulates the decay of long-lived particles, such as charged pions and K_S^0 , when it happens inside the detector.

The final step is the simulation of the response of the sensors and their readout electronics, producing raw detector data as similar as possible to the data obtained from the real detector. In this way, simulated and real events pass through the same reconstruction chain, avoiding biases. Accurate models of the detector's physics and electronics are used, although some simplification is necessary to achieve an acceptable processing time.

Each subdetector has its own response-simulating BASF2 module: here an outline of those used for PXD, SVD and VTX is given.

- For all three subdetectors, the energy deposited by the charged particles in the sensitive volume of the detector, provided by GEANT4, is used to generate electrons and holes.
- The drift of the charge carriers through silicon, thanks to the electric and magnetic fields, is simulated, taking into account Lorentz shift and diffusion effects.
- At this point, the response induced in the cells (strips or pixels) is computed:
 - for SVD, the signal induced in each strip is calculated;

- for PXD and VTX, the electrons accumulated in each charge-collecting electrode is calculated.
- The raw cell signal is then computed, taking into account noise, charge sharing with neighbouring cells, and the readout electronics (both analog effects, such as capacitive couplings, and effects of the conversion to digital).

This process is referred to as *digitization*, and produces as output a list of hits for each subdetector. Several parameters of the digitizer modules need to be tuned, often using experimental data and calibration results [15, 30].

Machine background Beam-induced background is simulated separately from the e^+e^- events: luminosity-dependent backgrounds (e.g. Bhabha scattering, two-photon processes) can be simulated within BASF2 with the aforementioned tools; instead, single-beam background (e.g. Touschek and beam-gas scattering, synchrotron radiation) can be simulated using a dedicated software by the accelerator group, SAD [33]. In either case, MCParticles are produced, and then their interaction with the detector is simulated with GEANT4 and the digitizers, like for event-generated particles. No simulation of the injection background is available at present.

The background hits are produced in extensive and systematic MC campaigns, and stored in *overlay files* for later use. The overlay files are then loaded during event simulation, and the background hits are overlaid to those of the e^+e^- events; the overlay hits can also be taken from experimental data, using a random trigger. The advantage of using overlay files is that the background simulation is performed only once for all event simulations, and also undergoes validation of dedicated experts.

3.4 Tracking with VXD and VTX

A brief summary of BASF2 tracking algorithms is given in this section, with the main purpose of comparing the current setup with the one proposed with VTX. Due to the differences between the tracking subdetectors, each of them employs ad-hoc algorithms; this forces to add an algorithm to merge tracks in the end.

In the current setup, CDC is the main tracking device. First, the CDC “standalone” algorithm finds tracks using only CDC hits; then, these CDC tracks are enriched with SVD clusters to improve their resolution. Afterwards, the SVD standalone algorithm finds tracks using only the remaining SVD clusters (those that were not “attached” to a CDC track). At this point, all the tracks are merged, and they are enriched with PXD hits to achieve final resolution. This is shown in fig. 3.11 [7].

With VTX, the procedure is as follows. The CDC standalone algorithm finds tracks using CDC hits; these CDC tracks are then enriched with VTX hits. Independently of this, the VTX standalone algorithm finds tracks using VTX hits; these VTX tracks are then enriched with CDC hits. At this point the tracks are merged, achieving final resolution without further steps. This is shown in fig. 3.12 [30].

Notice that VTX allows to use also the two innermost layers for track finding, while the two layers of PXD are only used to improve tracks that are found in the outer tracking subdetectors: this means that VTX should be able to find some low-transverse-momentum tracks that VXD cannot find (because they spiral in the magnetic field without reaching SVD), thus it is expected to have a higher track finding efficiency.

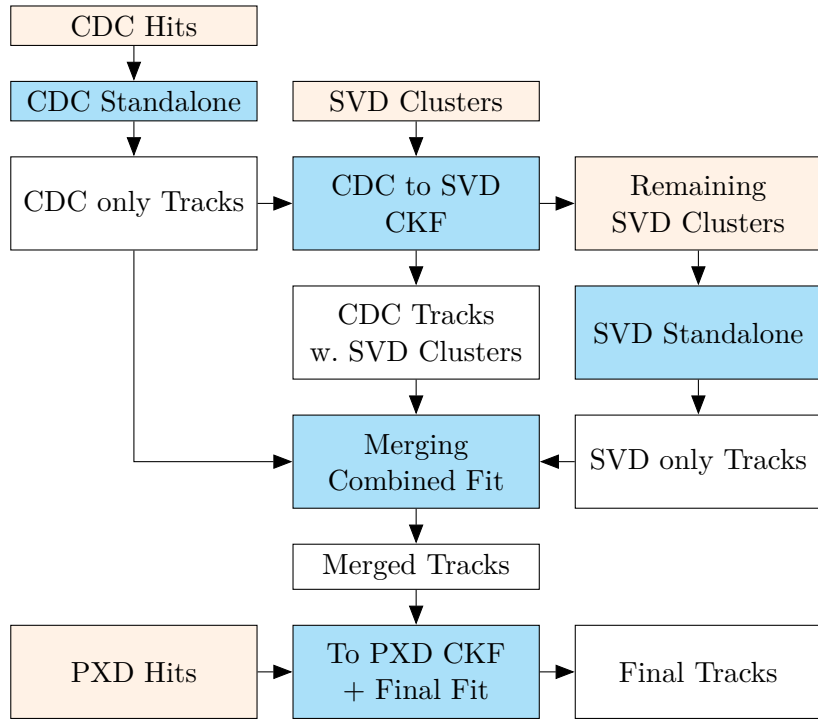


Figure 3.11: Overview of the steps of track reconstruction at Belle II.

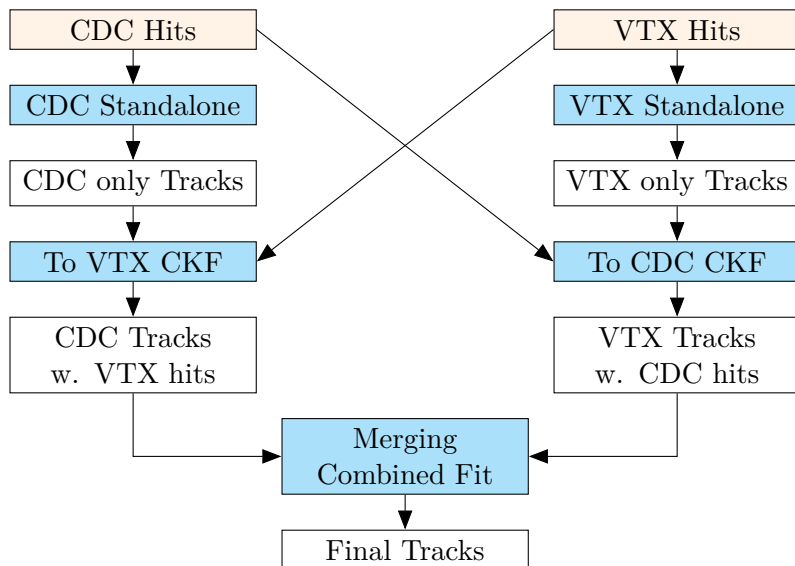


Figure 3.12: Overview of the steps of track reconstruction with VTX.

It is also worth mentioning, however, that both the version of BASF2 with VTX and the VTX sensors are still under development: for this reason, the tracking algorithms have not been tuned like those of VXD yet; this is expected to result in a higher rate of bad tracks (i.e. with incorrectly reconstructed parameters), clone tracks (i.e. more than one track for a single particle) and fake tracks (i.e. tracks that do not correspond to any particle).

Chapter 4

Radiation damage in SVD

In this chapter a study of the radiation damage in SVD sensors, and its effects on operation and performance, is presented. Section 4.1 summarises the radiation damage mechanisms in semiconductor detectors, and their expected effects on SVD; section 4.2 explains the method used to estimate the radiation dose absorbed by SVD sensors and presents the results obtained; section 4.3 present the analysis of the radiation's effects on sensors' properties such as depletion voltage, noise and leakage current; finally, section 4.4 summarises the possible effects of radiation damage and beam-induced backgrounds on detector performance.

4.1 Radiation damage in semiconductor detectors

This section summarises the mechanisms by which radiation damages semiconductor detectors: first, the mechanisms that are relevant for SVD sensors are described; then, the effects expected within SVD's operating life are presented.

4.1.1 Bulk damage mechanisms

In the *bulk* of the sensors (i.e. the substrate), ionising energy losses produce eh pairs, which do not contribute to silicon damage as they can drift and recombine without issues; bulk damage is, instead, caused by non-ionizing energy losses, which consist in the displacement of atoms from their position in the crystal lattice. These defects introduce new energy levels in the band gap of the silicon, altering the electrical properties of the sensor. Depending on their position with respect to the valence and conductance energy bands, these new states can act as (see fig. 4.1):

- donor or acceptor levels, altering the effective doping concentration and, consequently, the depletion voltage;
- trapping levels, reducing the charge collection efficiency;
- generation and recombination centers, affecting the leakage current.

The threshold energy for displacement in silicon is ≈ 25 eV. Massive particles can displace atoms via elastic scattering, or by starting a nuclear reaction; photons can displace atoms by producing recoil electrons, or by starting a nuclear reaction. The displacement produces a *Frenkel pair*, which is made of two point defects: an *interstitial* (the displaced atom) and a *vacancy* (the free lattice point left behind).

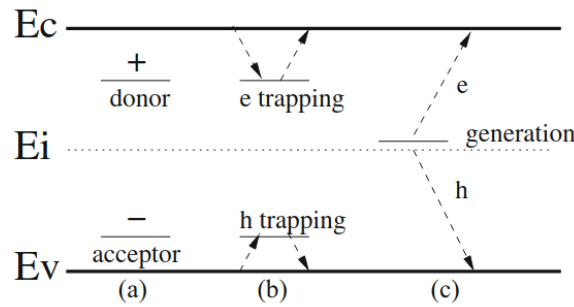


Figure 4.1: Consequences of deep energy levels on the operation of semiconductor detectors: charged defects alter the space charge and, therefore, the electric field (a); defects can trap and de-trap free carriers (b); defects act as generation and recombination centers (c) [34].

An atom that receives a recoil energy larger than the threshold will move in the bulk until it loses all of its energy, both by ionization and by displacing other atoms; if the energy is sufficient, at the end of the path the atom will displace several other atoms in a small volume, producing a *cluster defect*.

Above ≈ 150 K, point defects are mobile: if an interstitial and a vacancy meet they can recombine, annihilating each other. This effect is called *annealing*, and reduces the radiation damage over time. *Reverse annealing* effects have also been observed at high temperature, where the damage increases with a time scale longer than that of the beneficial annealing; these are interpreted as a slow diffusion of defects that can form more complex structures, thus producing additional energy levels which further contribute to the damage [35, 36].

However, a point defect may also reach an impurity or dopant atom and interact with it, changing the properties of the energy state, hence forming a permanent defect; this is the origin of radiation damage effects.

The NIEL hypothesis Both the maximum elastic recoil energy and the cross section of other available processes depend on the type and energy of the incoming radiation particle: comparison of the effects of different radiation fields is, therefore, complicated.

The non-ionizing energy loss (NIEL) hypothesis provides a model for this: the base assumption is that any effect of displacement damage scales linearly with the recoil energy that produces the displacing collision. The *displacement damage cross section* is a function $D(E)$ that provides the average recoil energy released by a particle of energy E per unit particle fluence, taking into account all possible interactions and the distribution of the energy lost to displacement; fig. 4.2 shows it for different particles.

If the spectrum of a radiation field is known, $D(E)$ can be integrated over it, obtaining the average recoil energy per particle fluence Φ . Usually, this integral is normalized to the one obtained with 1 MeV monochromatic neutrons, $D_n(1 \text{ MeV}) = 95 \text{ MeV mb}$, obtaining the hardness factor κ , and the *equivalent 1 MeV neutron fluence* $\Phi_{\text{eq}} = \kappa\Phi$, which is used to compare the effects of different radiation fields.

Effects on the sensor The effects on sensor performance are summarised here.

- Leakage current. A small current always flows through the reverse biased sensors, even when no particles are crossing it: this is called *leakage current*, and is due to

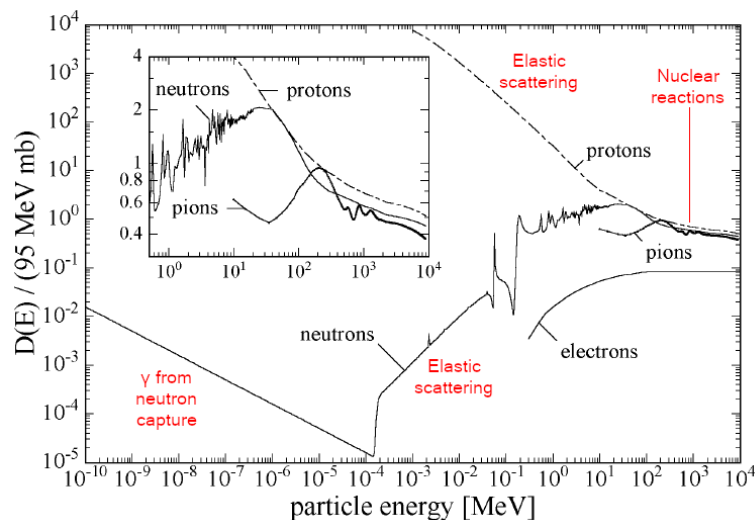


Figure 4.2: The displacement damage cross section for different particles, as a function of their kinetic energy. The main process responsible for displacement is indicated. Taken from [35].

the minority charge carriers, and the thermal generation of eh pairs. The presence of accessible states in the band gap of the silicon, such as those produced by defects, reduces the threshold necessary to produce eh pairs, thus increasing the rate of thermal pair generation and, consequently, the leakage current. Under the NIEL hypothesis, the total increase in leakage current is expected to be proportional to the equivalent neutron fluence and the volume of the sensor [35].

- Effective doping concentration and depletion voltage. The combination of displacement defects with the dopant atoms can modify the effects of the latter in a complex way, altering the concentration of the charge carriers: as a consequence, the *effective doping concentration* N_{eff} , and the depletion voltage which depends on it, change as a function of the equivalent 1 MeV neutron fluence Φ_{eq} , according to the NIEL hypothesis. An example of this is shown in fig. 4.3 for an n -type substrate test structure [35]. This can be explained in the following way: the displacement defects can deactivate some donor atoms (i.e. a vacancy-donor complex is not able to provide a free electron) with a rate proportional to the density of donor dopant, i.e. $dN/d\Phi_{\text{eq}} = -cN(\Phi_{\text{eq}})$, resulting in an exponential decay of N ; also, acceptor-like defects (e.g. di-vacancy complexes) are introduced, resulting in a linear increase of the density of acceptors. The resulting effective donor dopant concentration is therefore expected to be $N_{\text{eff}} = N(0)e^{-c\Phi_{\text{eq}}} - \beta\Phi_{\text{eq}}$. The effect on the full depletion voltage of the sensors is initially a reduction until type inversion is reached at Φ_{eq} of $\mathcal{O}(10^{12} \text{ cm}^{-2})$, depending on the material; after that, the depletion voltage raises again.
- Trapping and charge collection efficiency. Electrons and holes generated by the charged particles drift in the electric field towards the electrodes (*charge collection*). If they are captured (*trapped*) by a deep defect, and only re-emitted after longer than the shaping time of the readout electronics, a smaller charge will be detected (*charge collection deficiency*).

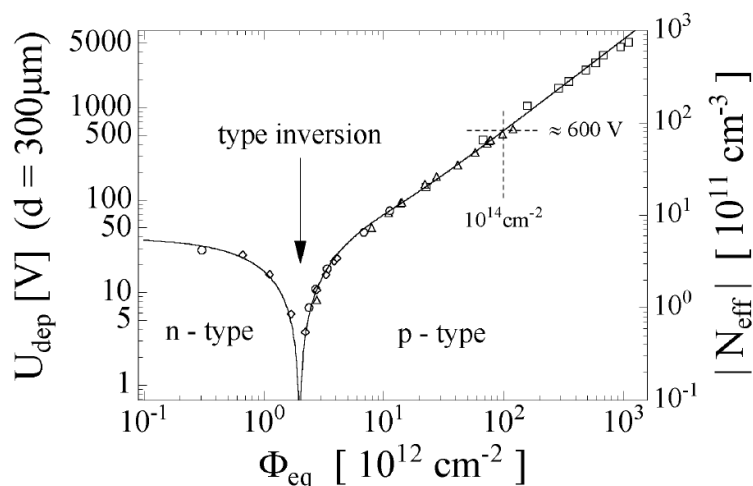


Figure 4.3: The depletion voltage U_{dep} and effective doping concentration N_{eff} dependence on the equivalent neutron fluence Φ_{eq} . Taken from [35].

4.1.2 Surface damage mechanisms

In this section the mechanisms through which radiation damages the surface oxide (SiO_2) and the SiO_2 -Si interface are outlined. Unlike in the silicon substrate, ionising energy losses are the main source of damage in the surface.

When an eh pair is generated through ionization, it is possible that the electron and hole recombine, but they may also drift in opposite directions due to the electric field present; depending on the direction of the electric field, the hole may reach the SiO_2 -Si interface, where it can recombine with oxygen vacancies (which are common at the interface), thus remaining trapped. This results in a positive charge stuck in the oxide (*oxide charge*), which adds to those already present (e.g. trapped during fabrication).

A hole may also react with an hydrogenated oxygen vacancy, freeing a proton which can move to the interface and break silicon bonds, producing point defects that may provide accessible levels inside the band gap of the silicon [37].

Effects on the sensor The effects on sensor performance are summarised here.

- Interstrip capacitance and noise. The increase in positive oxide charge due to surface damage can increase the interstrip capacitance, which is the dominant source of noise on the APV25 preamplifiers. The interstrip capacitance scales with the ratio of the width of the implant over the pitch. On the n side, the effective width of the strips includes not only the width of the n^+ implants, but also that of the electron accumulation layer, which is due to the fixed oxide charge; therefore, an increase in the oxide charge leads to an increase of the interstrip capacitance and, consequently, of the strip noise. On the p side, higher fixed oxide charge has the effect of altering the electric field at the p - n junction, resulting again in higher interstrip capacitance and, consequently, strip noise [36]. The magnitude of the effect strongly depends both on the details of the sensor design and on the initial amount of fixed oxide charge. There is a limit to the charge that can be trapped in the oxide, hence a saturation is expected (at around 100 krad) [38].

- Leakage current. The energy states due to point defects at the SiO₂-Si interface can act as generation centers, thus contributing to the leakage current as it happens in the bulk. Due to the e^- accumulation layer, only a small fraction of the surface area of the sensor is depleted (even at full reverse bias) and can contribute to surface-generated leakage current. For this reason the total leakage current is typically dominated by thermal generation effects in the bulk, especially after significant bulk damage.

4.1.3 Radiation damage in SVD

The simulations of the expected beam-induced background give, at the design luminosity of $8 \times 10^{35} \text{ cm}^{-2}\text{s}^{-1}$, an expected average background level in L3 sensor of about 1–3% strip occupancy, 0.1–0.3 Mrad/year integrated dose, and $0.2\text{--}0.6 \times 10^{12} \text{ cm}^{-2}/\text{year}$ equivalent neutron fluence [39]. These ranges correspond to the values from the initial Monte Carlo (MC) simulation, and from a more refined estimate that uses experimental background measures to re-scale the initial predictions.

Considering these predictions and some safety margin, the requirement set on radiation hardness for SVD sensors and electronics (assuming 10 years of operations) is 10 Mrad integrated dose and 10^{13} cm^{-2} equivalent neutron fluence. The APV25 is known to withstand over 100 Mrad, hence no issue is expected with the readout chips.

Radiation hardness of DSSD sensors up to this level was proven in the past: for instance, the BaBar silicon vertex tracker (SVT) sensors, which were produced by Micron with a design similar to that of SVD sensors and were exposed to a similar radiation field to the one expected in SVD, were successfully operated for several years, reaching an integrated dose of 4.5 Mrad [40]. Also, they were irradiated in dedicated campaigns above bulk type inversion (reached at about 3 Mrad of integrated dose and 10^{13} cm^{-2} of equivalent neutron fluence), and operated successfully up to 9 Mrad [40, 41].

Extrapolating the observations by BaBar, significant changes in the depletion voltage of SVD sensors could also be expected over the lifetime of the Belle II experiment; hence, the depletion voltage should be monitored. In addition, BaBar observed an increase in leakage current of $\approx 1 \mu\text{A}/\text{cm}^2/\text{Mrad}$ at 20 °C; the projected effect on SVD sensors is not expected to affect noise performance (through shot noise) significantly, thanks to the small APV25 shaping time, but it should be monitored as well. Finally, while oxide charge effects are not expected to degrade performance significantly, the saturation point is not well-known and must be measured on data.

In conclusion, monitoring the integrated dose in SVD and its effects on properties such as depletion voltage, leakage current and noise is fundamental to ensure robust operation of the detector.

4.2 Estimating the dose in SVD

The radiation dose absorbed by SVD can be estimated directly from SVD raw data by exploiting the deposited energy measurement (which is originally intend for particle identification): section 4.2.1 presents this method for the estimate. It must also be noted that the occupancy has a strong correlation to the dose rate, thus allowing for a simpler way of estimating the dose from data, as described in section 4.2.2.

However, any estimate of the dose relying on data can only estimate the dose absorbed while data is being recorded: since this is not always the case, a different method must be used. The diamond-based radiation monitoring sensors, described in

section 3.1.3, are active and record data whenever the beams are running; section 4.2.3 presents a method for estimating the dose rate by exploiting its correlation to the diamond detectors' readings. Finally, the results yielded by this method are presented in section 4.2.4, together with an explanation of the bias corrections adopted.

4.2.1 Dose estimate from data using cluster charge

The average dose rate d (i.e. the deposited energy per unit mass per unit time) in SVD can be calculated for each event as

$$d = \frac{E}{m_{\text{active}} \cdot \Delta t} = \frac{qE_{eh}}{\rho_{\text{Si}} A_{\text{active}} s \cdot \frac{n_{\text{samp}} - 1}{f_{\text{samp}}}} \quad (4.1)$$

where E is the deposited energy, computed by multiplying the collect charge q (in eh pairs, assuming no charge is lost) by the eh pair generation energy in silicon E_{eh} ; m_{active} is the mass of the active portion of the sensor, computed by multiplying the density of silicon ρ_{Si} by the active area A_{active} and thickness s of the sensor; Δt is the event integration time, which is the time span between the first and the last digitized samples, hence it is computed as number of samples n_{samp} minus one divided by the sampling frequency f_{samp} .

Silicon constants and sensor dimensions are known by construction; sampling and timing information is recorded in raw data on a per-event basis; the total collected charge can be computed (again, from raw data) by summing the charge of each cluster, thus allowing to achieve any degree of granularity: per-layer granularity is used in this analysis, with the exception of L3-mid-plane sensors. With double-sided sensors the collected charge is measured twice: n strips measure the signal from electrons, while p strips measure the signal from holes; the two measures should be equal in principle, but n strips are actually losing $\mathcal{O}(20\%)$ of the signal due to the wide pitch and the presence of a floating strip [15]: for this reason, in this study only p -side variables are considered for the dose.

Since the dose rate d is computed on a per-event basis, the selection of events is crucial and may introduce a bias; in order to correctly estimate the average d , one should use a random sampling of all collisions, where the probability to select each collision is the same and is independent of the properties of the resulting event: this is called a *Poisson trigger*, since the resulting number of triggered events follows a Poisson distribution. In addition, during continuous injection operation the “trigger injection veto” mechanism is used (see section 2.2.1), which discards events with very high background occupancy, produced by the newly injected bunch. These events could saturate the readout bandwidth, and are also not useful for physics analysis; however, their removal could introduce a negative bias in the estimate of the integrated SVD dose: for this reason, data taken without the injection veto should be used for this analysis.

Fig. 4.4 shows the computed dose rate vs time, averaged over 2 s intervals: averaging over such a short time without large statistical fluctuations is only possible during background-study runs, where only the Poisson trigger without injection veto is used at a 10 kHz rate. Note that during normal data taking (“physics runs”) this trigger is used at only 2 Hz due to bandwidth and data size limitations. The charge loss of v/n strips is visible for L456, but not for L3 due to the smaller n -side pitch. It is also evident that the dose rate is higher while injection is ongoing, due to the higher background from the injected bunch, with positron (LER) injection having a larger effect; the injection is performed with a repetition rate of 6.25 Hz, 12.5 Hz or 25 Hz when the beam

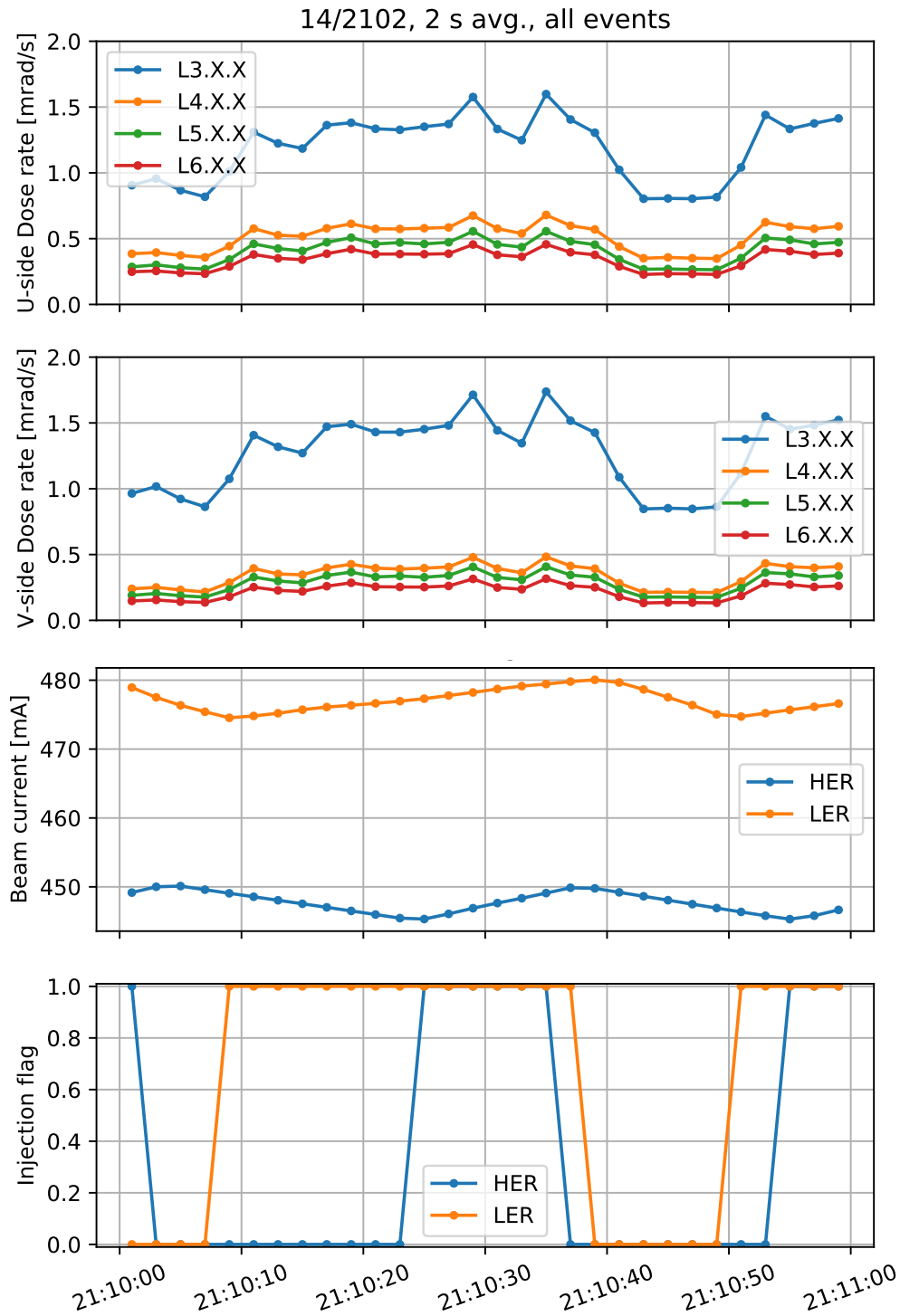


Figure 4.4: Dose rates (computed from clusters) averaged over each layer, beam currents and injection status recorded in one minute of experiment 14, run 2102 (on 16 December 2020). Variables are averaged every 2 s. Only Poisson trigger without injection veto was used in this background-study run.

current drops below 99% of the intended value, stops once this value is reached, and is performed independently for the HER and LER.

4.2.2 Correlation between dose and occupancy in SVD

The occupancy o , defined as the fraction of readout channels hit during an event, is proportional to the number of particles crossing the sensor during said event; since the dose rate is proportional to the energy deposited by these particles, dose and occupancy are expected to be proportional, with a slope that scales (at first order) with the area of the sensor.

$$\begin{aligned} d &= \frac{E}{\rho_{\text{Si}} \cdot A \cdot s \cdot \Delta t} \propto N_{\text{particles}} \cdot \frac{\langle E_{\text{particle}} \rangle}{A} \\ o &= \frac{N_{\text{hits}}}{N_{\text{strips}}} \propto N_{\text{particles}} \cdot \langle \text{cluster size} \rangle \\ &\Rightarrow d \propto \frac{o}{A} \end{aligned}$$

Specifically, in this study, the SVD strips with a signal-to-noise ratio above 5 are considered “hits” when computing the occupancy. Because of the aforementioned charge loss of the n strips, only u/p -side occupancy is considered for dose studies.

Computing occupancy is much simpler and faster than cluster charge, as it can be performed on raw data without running the clustering algorithm: being able to correlate the dose rate to the occupancy would therefore be convenient.

Fig. 4.5 shows a fit of the dose rate vs occupancy (averaged over each layer) with a line, for several runs of experiment 16;

$$d = f \cdot o \tag{4.2}$$

the two variables are indeed proportional to each other, with the ratio of the slopes scaling approximately as expected.

$$\frac{f_{\text{L3}}}{f_{\text{L4}}} \sim \frac{f_{\text{L3}}}{f_{\text{L5}}} \sim \frac{f_{\text{L3}}}{f_{\text{L6}}} \sim 1.5$$

Note that the average cluster size might be different among the layers due to the different pitches and track incident angles, possibly explaining the difference between the measured ratio and the ratio of the sensors areas. This proportionality is expected to be constant assuming that the average energy deposited per hit (in each layer) and the background distribution are stable over time.

The fitted slopes f are shown in tab. 4.1, and are used in this analysis to convert between occupancy and dose.

| Layer | Slope [mrad/s/%] | Layer | Slope [mrad/s/%] |
|-------|-------------------|-------|-------------------|
| L3 | 10.95 ± 0.01 | L5 | 7.073 ± 0.006 |
| L4 | 7.087 ± 0.008 | L6 | 6.794 ± 0.006 |

Table 4.1: Occupancy to dose rate conversion factors f for the SVD layers, fitted in experiment 16, runs 942, 981, 983, 1011, 1012 and 1013.

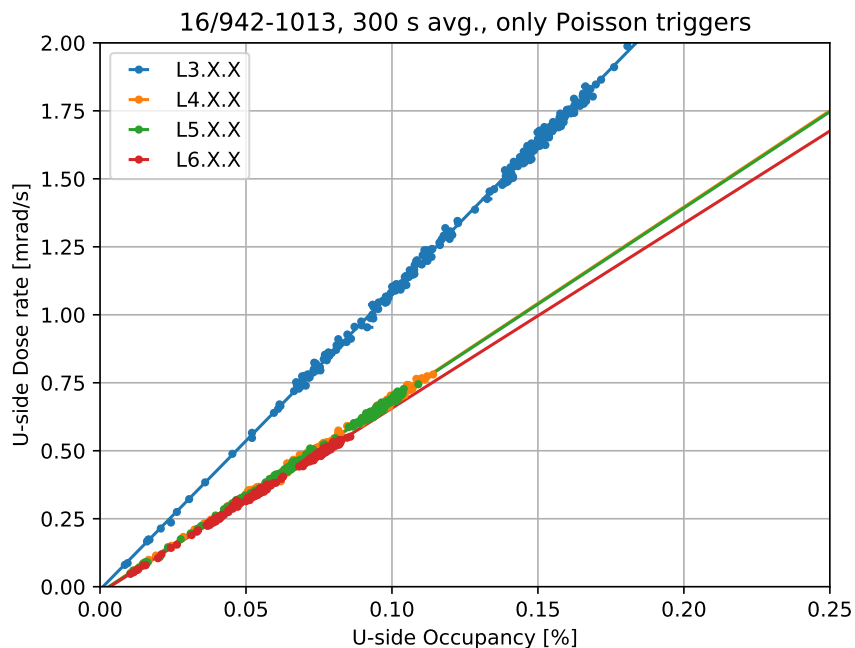


Figure 4.5: Dose rate (from clusters) vs occupancy, averaged over each layer and every 300 s, in experiment 16, runs 942, 981, 983, 1011, 1012 and 1013; these are physics runs, but only Poisson trigger without injection veto events are considered. A fit with a line is also shown.

4.2.3 SVD dose estimate from diamond dose

In order to estimate the dose also when SVD data is not being recorded, a method relying on a different measure must be used. The diamond sensors of the radiation monitor and beam abort system are necessarily active whenever the beams are running; since their data is recorded continuously, and they show a good correlation with SVD occupancy, they can be used to estimate the occupancy and, from that, the dose rate even when SVD is not recording data.

For this study, the BP_BW_325 and BP_FW_325 diamonds, located on the beam pipe, were chosen for multiple reasons:

- they are located close to L3, hence a strong correlation with the dose in L3 sensors (the innermost and most irradiated ones) is expected;
- their readout is configured with the smallest current range, thus allowing precise measurements;
- one is placed backward (BW), hence it is expected to be more sensitive to LER background, while the other is placed forward (FW), hence it is expected to be more sensitive to HER background, thus allowing a simple yet robust estimate despite the variability of beam conditions.

Simplicity is one of the main goals of this study, hence a linear correlation function is chosen to express the SVD occupancy o in terms of the diamond dose rates

$$o = C_0 + C_1 d_{\text{bw}} + C_2 d_{\text{fw}} \quad (4.3)$$

where d_{bw} and d_{fw} are the dose rates in the two diamonds, and the correlation coefficients C_i are measured from data as shown below; a different set of C_i is used for each layer, and also L3-mid-plane sensors (L3.1.X and L3.2.X) have their own set of C_i , different from the rest of L3. The offset C_0 is used to account for occupancy due to noise hits, present even without beams and radiation.

The estimated occupancy can then be converted to dose rate using the f factors from the previous section (see eq. 4.2)

$$d = f \cdot o = f(C_1 d_{\text{bw}} + C_2 d_{\text{fw}}) \quad (4.4)$$

where d is the SVD dose rate and f is the occupancy-to-dose-rate conversion factor from the previous section; notice how C_0 does not appear in this formula, as it models the occupancy that is not due to radiation.

Eq. 4.4 is then used to estimate the SVD dose rate even when SVD is not recording data, using the always-available diamond dose rates. Being a linear formula, it is also used to estimate the integrated dose in SVD from the integrated dose in the diamonds.

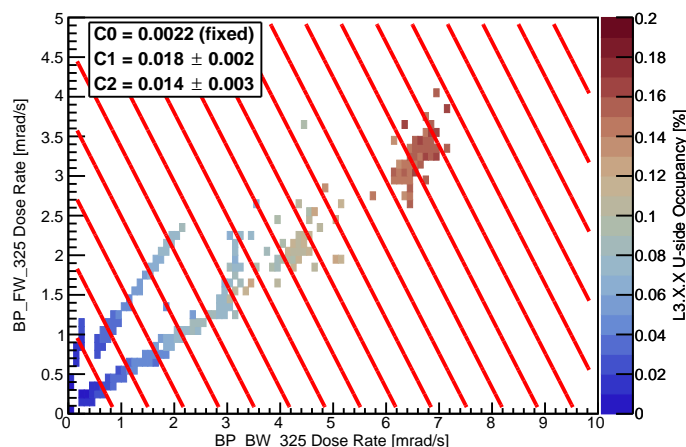


Figure 4.6: Fit of the correlation coefficients for L3 using experiment 12, runs 3759 to 3785 (background studies, decay, 10 s averages) and experiment 16, runs 904 to 1013 (physics, Poisson trigger without injection veto only, 300 s averages). The red lines are the contour of the fit function.

The correlation coefficients C_i needed for the analysis have been measured on data, using eq. 4.3 as a fitting function to extract them. An example fit results for L3 is shown in fig. 4.6. The fit is performed simultaneously on physics runs, where both beams have similar currents, and on background-study runs, which include single-beam runs as well; this allows to disentangle the contributions of the two diamonds. The C_0 coefficient, due to noise only, is fitted separately on no-beam runs. The physics runs are taken from experiment 16 (March 2021), and only Poisson trigger without injection veto events are considered. The background-study runs, instead, are taken from experiment 12 (May 2020), when similar accelerator parameters were used. Since the Poisson trigger without injection veto was not available at the time of these background-study runs, only data without injection (“decay runs”) is used to avoid the bias from the injection veto.

The results of the fits are shown in tab. 4.2. Fig. 4.7 compares the measured occupancies for L3 with the ones predicted from the diamonds using eq. 4.3 and the fitted coefficients, also showing the beam currents for reference: depending on the beam conditions, differences between predicted and measured occupancy up to 30% are visible,

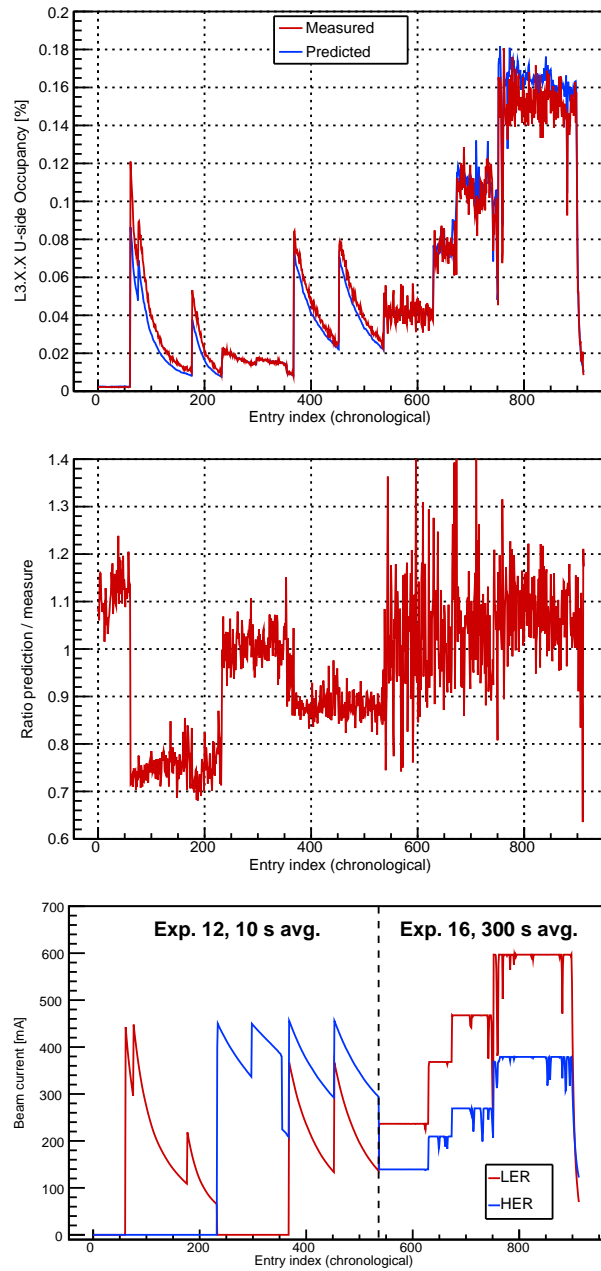


Figure 4.7: Above: L3 occupancy measured on data (“measured”) and estimated from diamonds (“predicted”); middle: ratio of occupancy from diamonds over occupancy measured on data; below: beam currents, for reference. Displaying the runs used for fitting the C_i coefficients: experiment 12, runs 3759 to 3785 (background studies, decay, 10s averages) and experiment 16, runs 904 to 1013 (physics, Poisson trigger without injection veto only, 300 s averages).

hence an accuracy better than this cannot be expected; large fluctuations are visible for experiment 16, which are due to the much lower statistics of the Poisson trigger without injection veto during physics runs.

| Layer | C_0 [%] | C_1 [%/(mrad/s)] | C_2 [%/(mrad/s)] |
|--------|---------------------|--------------------|--------------------|
| L3 mid | 0.0021 ± 0.0004 | 0.022 ± 0.003 | 0.019 ± 0.003 |
| L3 | 0.0022 ± 0.0004 | 0.018 ± 0.002 | 0.014 ± 0.003 |
| L4 | 0.011 ± 0.002 | 0.010 ± 0.002 | 0.006 ± 0.003 |
| L5 | 0.007 ± 0.001 | 0.011 ± 0.001 | 0.004 ± 0.002 |
| L6 | 0.010 ± 0.002 | 0.008 ± 0.001 | 0.002 ± 0.002 |

Table 4.2: The correlation coefficients resulting from the fits.

Fig. 4.8, instead, compares predicted and measured L3 occupancies on data from some experiment 17 runs, using again the coefficients extracted from experiments 12 and 16: the fact that the fluctuations are again of $\mathcal{O}(30\%)$ proves the robustness of the method.

This method was already used in the past to evaluate the SVD dose from the diamond data [15, 42], but two main improvements are introduced in this work.

- Use of events from the Poisson trigger without injection veto (available only since March 2021). In the past the same dose analysis was performed using events from the physics trigger (with injection veto) to measure the correlation coefficients, and introducing an empirical correction factor to compensate for the negative bias (i.e. lower average occupancy) due to the injection veto; the correction factor was measured on a single special run where the injection veto was not applied to the physics trigger. When the new Poisson trigger without injection veto became available, this new analysis proved that the old correlation coefficients, and consequently the dose, were largely overestimated; this was due to a positive bias (i.e. larger average occupancy) introduced by the physics trigger. With the old analysis, the total integrated dose resulted $\sim \times 3$ larger than the values presented in this thesis.
- The correlation coefficients in the new analysis are extracted with an independent fit for each layer and for the mid plane of L3; in the previous analysis, the fit was performed for the mid plane of L3, and then empirical factors were used to scale the correlation coefficients to the various layers. In addition, the C_0 coefficient, taking into account occupancy from noise hits, was not present in the old analysis.

4.2.4 Results

The latest estimates of total integrated dose in SVD are shown in fig. 4.9: almost 70 krad for L3-mid-plane sensors, about 55 krad for the rest of L3, and around 15 krad for the outer layers.

These are computed by integrating the dose rates of the diamonds since the beginning of the experiment and using eq. 4.4, or rather

$$D = f(C_1 D_{\text{bw}} + C_2 D_{\text{fw}})k \quad (4.5)$$

where D is the integrated dose in SVD, while D_{bw} and D_{fw} are the integrated doses in the diamonds. An empirical factor $k = 1.2$ was applied to account for the effect of

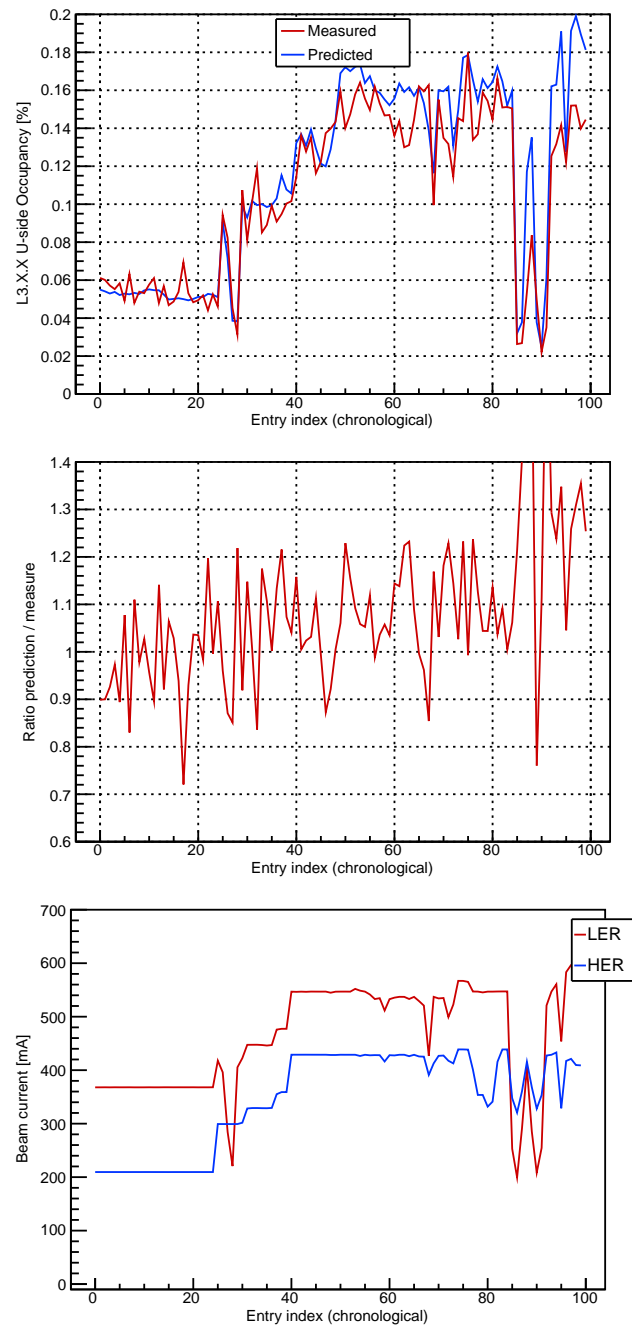


Figure 4.8: Above: L3 occupancy measured on data (“measured”) and estimated from diamonds (“predicted”); middle: ratio of occupancy from diamonds over occupancy measured on data; below: beam currents, for reference. Displaying runs 60 to 146 of experiment 17; the coefficients used are the ones in tab. 4.2, fitted on selected runs of experiments 12 and 16.

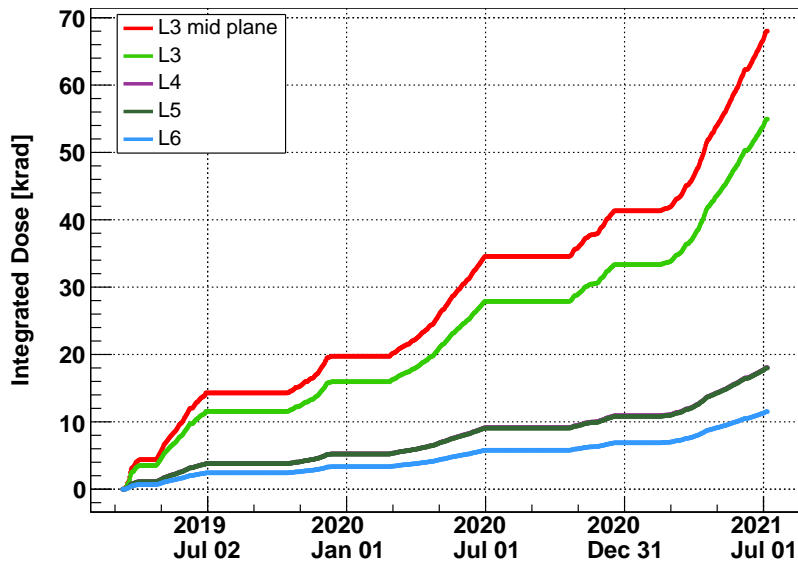


Figure 4.9: Latest estimate of the total integrated dose in SVD.

the *events-of-doom-buster* (EODB) module: this is a BASF2 module that rejects events with an SVD or CDC occupancy above a fixed threshold to prevent HLT servers from running out of memory during track reconstruction. The empirical correction factor for the EODB module was obtained from background-study runs where EODB was excluded from the DAQ workflow (when only the Poisson trigger is used, HLT does not need to perform event reconstruction).

Besides the EODB module, other sources of bias are still present in this estimate of the integrated dose, for which the appropriate correction factors are not known; they are summarised here.

- This estimate assumes that the same correlation coefficients were valid since the beginning of data taking, while they could have been different in the past due to the different beam conditions. The bias introduced could in principle be measured by extracting the correlation coefficients also from past data; however, the occupancy would need to be measured on Poisson trigger without injection veto events, and this trigger line was not available until March 2021. In order to monitor the evolution of these coefficients in the future, a BASF2 module was developed to monitor the ratio of the occupancy predicted from the diamonds over the occupancy measured on Poisson-trigger events; the module is executed online during data taking, and reports results averaged over 10^3 s (≈ 17 min) and over each run (see fig. 4.10).
- The effect of the EODB module is not constantly monitored, and the few measurements of its correction factor show fluctuations that may affect the dose estimate by $\mathcal{O}(10\%)$; also, there are no studies for this before December 2020.
- After an injection, the readings of the two diamonds systematically saturate; unless the fraction of dose lost due to the saturation is constant over time, this introduces an additional bias.

Considering the uncertainties on the coefficients from the fit, the observed fluctuations of the occupancy prediction, and the observed fluctuations of the EODB correction factor,

the uncertainty on the integrated dose is of $\mathcal{O}(50\%)$; this estimate does not include the (unknown) effects of the different beam conditions in the past, and of the saturation of the diamonds due to the injection. Still, it is enough to evaluate the evolution of sensor properties with the increasing dose, as shown in the following section.

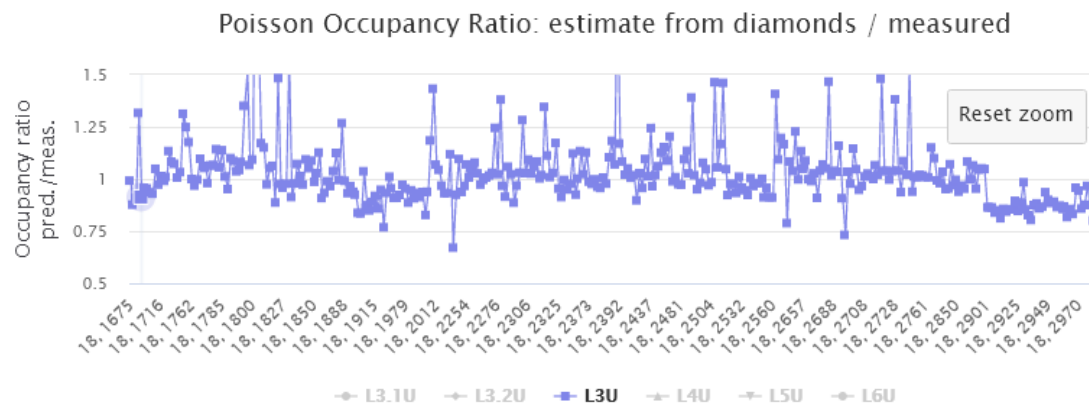


Figure 4.10: A plot of the ratio of the L3 occupancy estimated from the diamonds over that measured on Poisson-trigger events, for several experiment 18 runs. Each point shows the average over one run. The plot is produced by the online monitoring module mentioned in the text, and by the quality-monitoring system *MiraBelle*. Fluctuations are typically of $\mathcal{O}(25\%)$.

4.3 Radiation damage effects on SVD

In this section, the evolution of the depletion voltage, noise and leakage current of the sensors is described: expected changes, possible impact on performance and measured values are shown.

4.3.1 Depletion voltage

SVD DSSD sensors need to be fully depleted to be operable (otherwise n side strips would not be insulated): the bias voltage used during operation is 100 V, well above the 20 V to 60 V [15] depletion voltages of the different sensors. However, bulk damage can change and heavily increase the depletion voltage by altering the effective doping concentration of the sensors.

The expected change in bias voltage is shown in fig. 4.3 as a function of the equivalent neutron fluence Φ_{eq} : at the current estimated dose (≈ 70 krad for the mid plane of L3) $\Phi_{\text{eq}} \approx 10^{11} \text{ cm}^{-2}$, and no significant change is expected. However, it is important to monitor the evolution of the depletion voltage, and compare it to the expectation so as to spot significant deviations. In addition, the equivalent neutron fluence is estimated using a dose-to-fluence ratio extracted from MC simulations, which contributes to the uncertainty.

Estimate from noise vs bias voltage The method used to measure the depletion voltage exploits the fact that the n strips are short circuited unless the bulk is fully

depleted: this means that the capacitive load on the APV25 preamplifier inputs is higher before the depletion (because the strips are in parallel), and rapidly drops when the depletion is reached. Higher capacitive load implies higher noise, so measuring the noise vs the bias voltage allows to identify the depletion voltage, which corresponds to the sudden drop of the n -side strip noise.

This method has the advantage that it does not require the use of beam time, at the expense of physics data taking, as in other methods based on the study of the collected cluster charge (which scales with the depleted volume) as a function of the bias voltage [43]. The full set of calibrations required takes ~ 12 h and can be performed during relatively short stops of machine operations or during summer shutdowns.

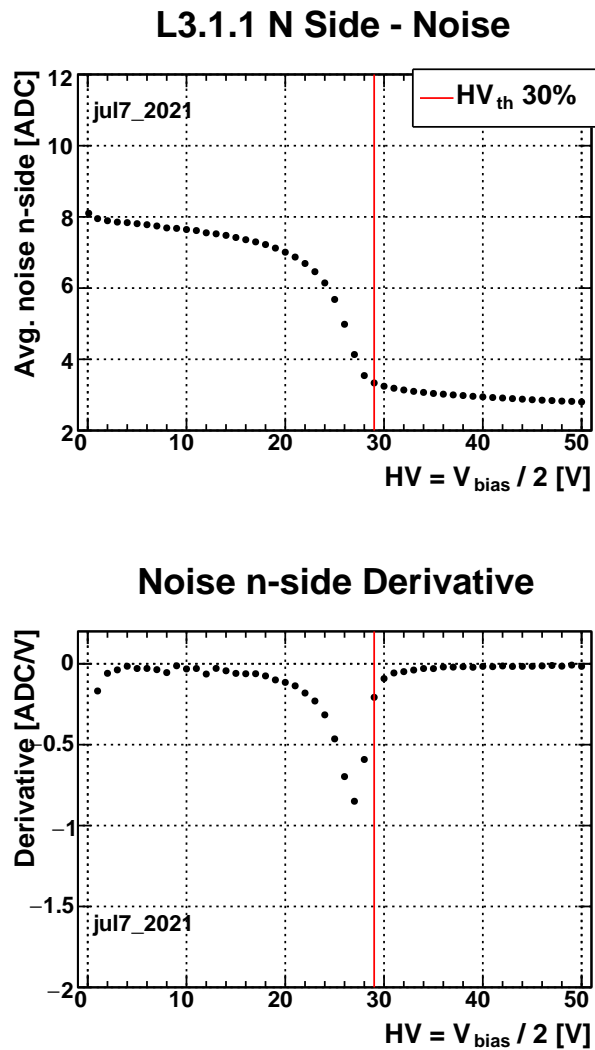


Figure 4.11: Average n -side strip noise vs bias voltage for sensor L3.1.1, measured on July 7, 2021.

Fig. 4.11 shows a measurement of n -side noise vs bias voltage for one SVD sensor: when the depletion voltage is reached, the noise drops suddenly. An automatic algorithm was made to detect the depletion voltage of each sensor: the noise vs bias

voltage derivative is approximated by computing the incremental ratio of two successive measurements; the peak of the derivative is found; the first point after the peak which has a derivative below 30% of the peak (in absolute value) is identified as depletion voltage. Since the goal is spotting significant changes, an accurate measurement is not necessary: a simple algorithm is, therefore, sufficient. The 30% threshold was chosen empirically to exclude the points in the plateau (which still have a small negative derivative). The voltage identified this way corresponds (within a few V) to the depletion voltage measured during sensor tests before the installation in the detector (using capacitance-vs-bias-voltage or strip-insulation-vs-bias-voltage measurements directly on the sensors).

Results Fig. 4.12 shows the distribution of the depletion voltage for the three sensor types: as expected [15], micron sensors have depletion voltages between 20 V and 40 V, while HPK sensors (both large and small) have depletion voltages between 40 V and 60 V.

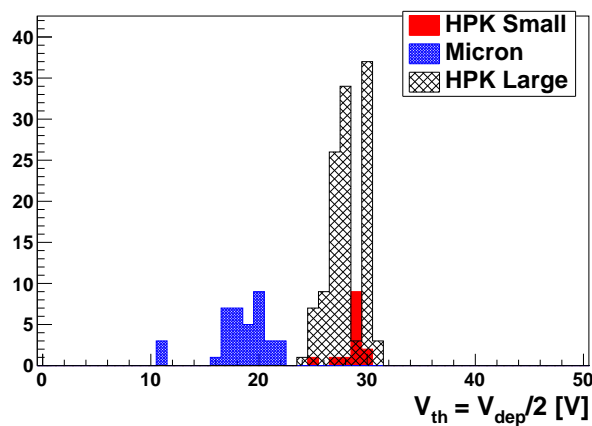


Figure 4.12: Depletion voltage distribution as of July 7, 2021.

Also, between July 2020 and July 2021, no significant changes were found among the depletion voltages measured by the algorithm, as expected. Fig. 4.13 shows the noise vs bias voltage for one SVD sensor in different dates: the only differences that can be found are slight shifts in noise magnitude, without any significant effect on the depletion voltage; the sensor shown is one of those that present the greatest changes. The increase of noise observed in later measurements is related to the surface damage due to the integrated dose, as explained in section 4.1.2 and in the next section. The first measurement was performed in July 2020, after ~ 30 krad of integrated dose and less than 10^{11} cm^{-2} of equivalent neutron fluence in L3 sensors: no changes in depletion voltage, with respect to the measurements performed before the installation, were expected at that point.

4.3.2 Noise

In order to reduce data size and make it possible to reconstruct clusters, only strips with a signal-to-noise ratio above 3 are recorded; thus, an increase in noise may lead to performance deterioration. The total noise in strip detectors has several components; those that are expected to increase with radiation damage are that from the capacitive

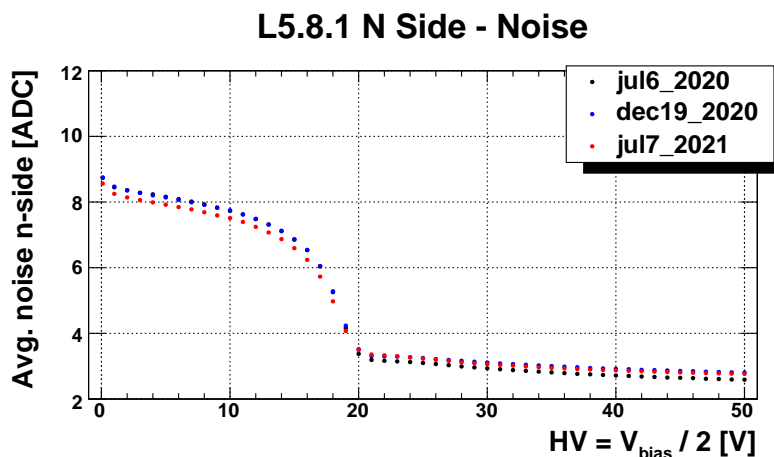


Figure 4.13: Average n -side strip noise vs bias voltage for sensor L5.8.1 in different dates.

load of the preamplifiers and that from strip leakage current, given by the following equations as equivalent noise charge (ENC, i.e. the noise of the circuit, after filtering, translated in charge units and referred to the input node, so that it can be directly compared with the measured charge)

$$\text{ENC}_C = a + bC, \quad \text{ENC}_{\text{leak}} = \frac{e}{2} \sqrt{\frac{I_{\text{leak}} \tau_{\text{shaping}}}{e}} \quad (4.6)$$

where C is the total capacitive load on the preamplifier (roughly interstrip plus back-plane capacitance), a and b are constants that depend on the readout chip, e is Euler's number, e is the elementary charge and I_{leak} is the strip leakage current (corresponding to the electrode area associated with the readout pitch) [4, 26]. The short shaping time $\tau_{\text{shaping}} = 50$ ns of the APV25 chips strongly suppresses the leakage current term, so that the noise in SVD is dominated by the capacitive term.

The interstrip capacitance is expected to increase with irradiation as a consequence of the increase of oxide charge, thus increasing C and the noise; also the leakage current is expected to increase, producing small changes in the noise. The increase of oxide charge is expected to saturate at ≈ 100 krad, although the capacitance may saturate even before that point.

An accurate knowledge of the noise is necessary to correctly select hits based on the signal-to-noise ratio, hence strip noise measurements are relatively frequent. This also allows to monitor the evolution of noise with time.

Results The average noise of the various SVD sensors at the beginning of data taking is shown in tab. 4.3. Noise was expected to be higher in p -side strips than in n -side strips, because the former are longer and have smaller pitch ($C_{\text{interstrip}} \propto l/d$ at first order, where l is the strip length and d is the distance between the strips, i.e. the pitch). Also the different pitch adapters that connect the strips to the readout chips contribute to the load capacitance, resulting in different noise for sensors of the same type but mounted in different positions on the ladder, due to the different pitch adapter length (visible in the table for HPK large sensors).

Fig. 4.14 shows the evolution of the noise with the estimated integrated dose. In HPK small sensors the expected saturation of the noise is visible both on p side (at

≈ 70 krad) and n side (at only ≈ 10 krad). In HPK large sensors the n side saturation is visible (again at ≈ 10 krad), while p side saturation has not been reached yet (because a much smaller dose has been absorbed by the outer layers). Micron sensors, instead, present no significant change in noise, as if the oxide charge was already at saturation right after fabrication, or the design was less sensitive to changes in the oxide charge and consequent changes in the interstrip capacitance.

| Sensor type | Position | p/u ENC [e^-] | n/v ENC [e^-] |
|---------------------------|---------------|---------------------|---------------------|
| HPK small | L3 | 930 | 630 |
| HPK large without origami | L456 backward | 790 | 680 |
| HPK large with origami | L456 middle | 958 | 510 |
| Micron trapezoidal | L456 forward | 740 | 640 |

Table 4.3: Average noise (ENC) measured for each SVD sensor at the beginning of data taking in 2019. Taken from [15].

4.3.3 Leakage current

It is important to monitor the evolution of the leakage current with irradiation in order to confirm that it follows the expectations, and also to extrapolate the possible effects on noise contribution, although the short shaping time of the APV25 chips suppresses these effects with respect to those of the capacitive load of the preamplifiers. The increase of leakage current from bulk damage is expected to be proportional to the equivalent neutron fluence; therefore, as long as the radiation field composition does not change too much, the increase of leakage current can be expected to be roughly proportional to the integrated dose.

Like noise, also leakage current is measured relatively frequently, allowing to perform studies of its evolution with time.

Results The evolution of the leakage current for one L3 sensor is shown in fig. 4.15. In the time plot a pattern can be seen, which is related to machine operations and shutdowns. When beams are operated, the current increases roughly linearly. Instead, after the shutdown periods (summer and Jan–Feb), current can be slightly lower (due to annealing effects, since cooling is off during summer), or show some slight increase, likely due to turn-on effects (probably due to charges slowly drifting in the dry VXD atmosphere, currents are slightly higher at first, then decrease as power supply is kept turned on for a few days, but these effects are not completely understood).

In the first half of 2020 a relatively long non-linear behaviour is visible: this was caused by changes in L3 sensor temperature due to PXD temporarily adopting a different power setting. Such effects cannot be accurately evaluated, however, because the exact temperature of SVD sensors is not well known: the temperature sensors in VXD are located close to the readout chips and the cooling pipes, as they are meant to monitor the cooling system operations, and while they proved a stable temperature (between 5 °C and 30 °C) is maintained, they do not allow to measure the real SVD sensor temperature. This makes it impossible to evaluate annealing effects accurately, as they depend on the sensor temperature.

The evolution of the leakage current with the dose (also shown in fig. 4.15) seems to be well approximated by a linear model, as expected. A fit with a line is performed for each of the 172 sensors, and the resulting slopes (per unit active area of the sensor) are

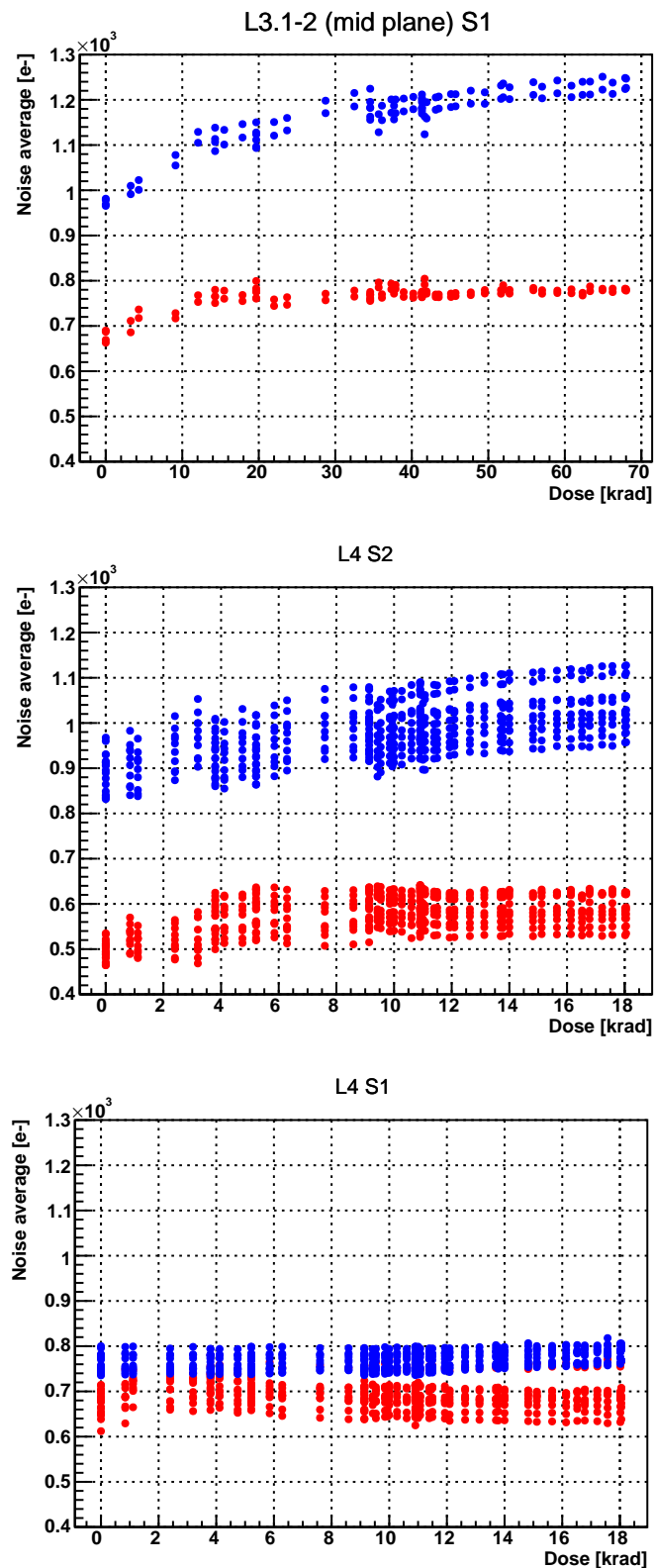


Figure 4.14: Average strip noise vs dose (*p* side in blue and higher, *n* side in red and lower) for different groups of SVD sensors: HPK small in L3 mid plane (above), HPK large in L4 (middle), and Micron in L4 (below).

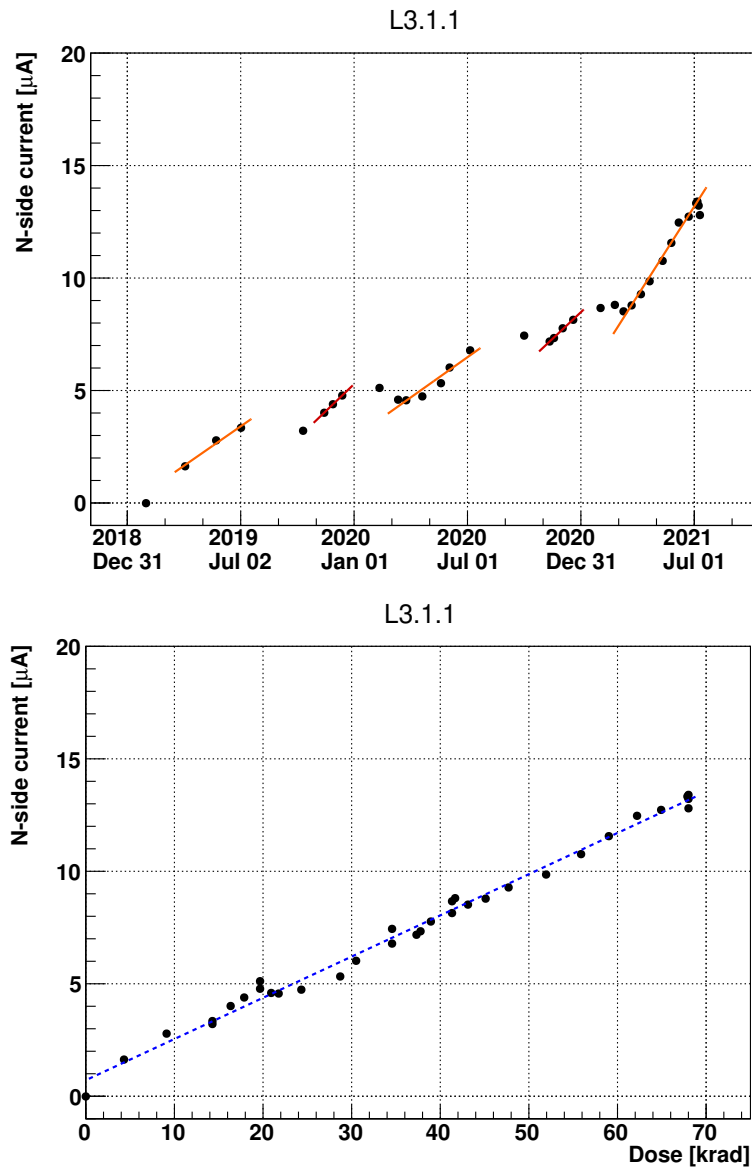


Figure 4.15: Evolution of the leakage current with time (above, lines indicate the run periods) and dose (below, line is a linear fit) for one SVD sensor in the mid plane of L3 (one of those that absorbed the highest dose).

shown in fig. 4.16: all slopes are found to be of $\mathcal{O}(1 \mu\text{A}/\text{cm}^2/\text{Mrad})$, which is similar to what was found by BaBar. This is to be expected since the radiation fields of BaBar and Belle II have similar compositions, originating from the background components of e^+e^- machines, leading to similar ratios between total dose and NIEL [15]. The spread of the distributions is due to temperature and dose differences among the sensors: the average dose of the layer is used for all of the sensors, with the exception of L3-mid-plane sensors, but differences may exist across the layer; in particular, Micron slanted sensors are closer to the IP and may absorb a larger dose, resulting in larger computed slopes as in the histograms.

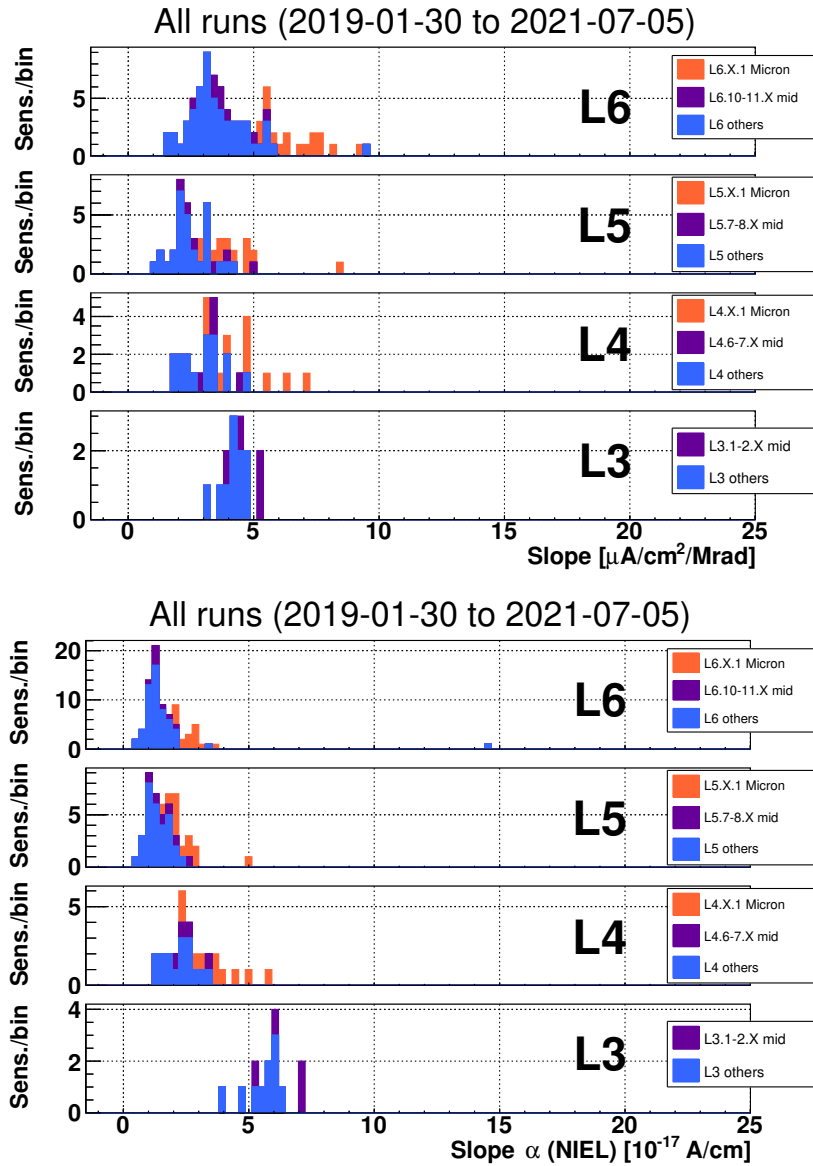


Figure 4.16: Distributions of the leakage current slopes (stack plots).

The dose can be converted to equivalent neutron fluence by using appropriate factors, which can be obtained from Monte Carlo simulations; the factors for the layers of SVD are shown in tab. 4.4. The NIEL hypothesis predicts that the increase in leakage current

is given by

$$\Delta I = \alpha \Phi_{\text{eq}} V \quad (4.7)$$

where V is the volume of the sensor and α is an empirical factor that depends on the annealing conditions; at 20 °C it is found to be $\approx 8 \times 10^{-17}$ A/cm right after the irradiation, and to saturate at $\approx 2 \times 10^{-17}$ A/cm after annealing has taken place [35]. The results in the histogram are of the expected order of magnitude; note that the annealing contribution is unknown for SVD sensors, since their temperature is not well known, and α also scales with the temperature as the leakage current, increasing by a factor 2 every $\Delta T \approx 8$ °C. The higher α obtained for L3 (with respect to the other layers) is likely due to the higher temperature of L3 sensors, which have no cooling pipes running on the ladders (since all APV25 chips are outside the active region) and are very close to PXD ladders (whose temperature is monitored and is 26–30 °C); for comparison, the temperature of L456 sensors should be 5–15 °C (although this is measured on the cooling pipes close to the APV25 chips, and not on the sensors themselves).

| Layer | [$10^9 \text{ cm}^{-2} \text{ krad}^{-1}$] | Layer | [$10^9 \text{ cm}^{-2} \text{ krad}^{-1}$] |
|-------|--|-------|--|
| L3 | 2.33 | L5 | 5.83 |
| L4 | 4.19 | L6 | 8.40 |

Table 4.4: Dose to equivalent neutron fluence conversion factors extracted from MC simulations [44].

With the measured slopes, the increase of leakage current per strip in L3 mid-plane sensors will not affect significantly the total strip noise, even after 10 years of operation at design luminosity (which should correspond to ~ 3 Mrad); the noise contribution from leakage current will become comparable to present noise levels at about 10 Mrad.

4.4 Background effects outlook

The evolution of the depletion voltage, the noise and the leakage current with the increasing integrated dose has been studied, and the results are reasonably in agreement with the expectations. Although great uncertainties are present, this indicates that the projections presented in section 4.1.3 are valid: the SVD sensors should be able to withstand about 10 Mrad of dose and $30 \times 10^{12} \text{ cm}^{-2}$ of 1 MeV equivalent neutron fluence; after that, performance is expected to degrade, mainly due to the noise increase [15].

An integrated dose of 55 krad, corresponding to an equivalent neutron fluence of $\approx 0.13 \times 10^{12} \text{ cm}^{-2}$, was accumulated on average in L3 sensors in the first 2.5 years of operation, with gradually increasing beam currents and luminosity. MC simulations, re-scaled using background studies on data from year 2020, indicate that an integrated dose of ≈ 0.3 Mrad/year and an equivalent neutron fluence of $\approx 0.6 \times 10^{12} \text{ cm}^{-2}$ /year are to be expected at design luminosity (i.e. $8 \times 10^{35} \text{ cm}^{-2} \text{ s}^{-1}$) [15]. Even considering this and 10 years of operations at design luminosity, an integrated dose of ~ 3 Mrad is expected, leaving a safety factor of ~ 3 with respect to DSSD sensor limits (and 10 times as much with respect to APV25 limits). Hence, radiation damage is not expected to be an issue for SVD performance and operations, although having a larger safety factor would be preferable, considering the large uncertainties affecting the extrapolations.

On the other hand, with higher levels of beam-induced backgrounds, the higher instantaneous occupancy (i.e. the occupancy in a single event) due to background hits

could become a critical issue. With an occupancy above 3% (corresponding to an hit rate of ~ 3 MHz/cm² in L3), tracking performance is expected to degrade significantly. Currently the occupancy is rather small ($< 0.4\%$), but the aforementioned MC simulation with re-scaling predict that L3 occupancy will approach this 3% limit at design luminosity (see fig. 4.17); considering the large uncertainties affecting these projections, having a safety margin is necessary. Strategies to mitigate background levels are under study; these include improving collimators and the beam pipe in the interaction region to reduce background hits, using the three-samples readout mode to reduce the necessary readout bandwidth, and using the hit time information to reject background hits. A preliminary estimate indicates that the hit time cut should allow to increase the occupancy limit to $\sim 6\%$, leading to a safety factor of 2; yet, considering the extrapolation uncertainties, having a larger safety margin would be preferable [15].

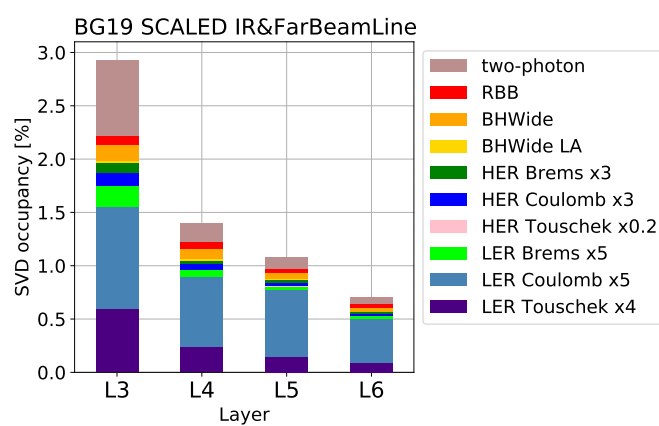


Figure 4.17: Extrapolation of the occupancy in each SVD layer at design conditions (i.e. luminosity of 8×10^{35} cm⁻²s⁻¹), after re-scaling MC simulations using background studies on data recorded in 2020. Different contributions are shown for luminosity-dependent (two-photon processes, radiative Bhabha scattering) and single-beam (*bremstrahlung*, Coulomb beam-gas scattering, Touschek effect) backgrounds (see section 2.2.1). Taken from [15].

Besides this, the possibility of an upgrade to a more background-tolerant detector is under study. A long shutdown period (about nine months) is planned around 2026 to install accelerator upgrades that are necessary to reach design luminosity; targeting this time for the upgraded detector installation, several options have been proposed and are being studied for the replacement of SVD.

Proposals to replace the whole VXD (e.g. the VTX proposal, presented in section 3.2) are also under study: PXD is, in fact, in a situation similar to that of SVD. Extrapolations indicate that PXD occupancy will be $\sim 1\%$ (corresponding to an hit rate of ~ 20 MHz/cm²) at nominal luminosity, which leaves a safety factor of ~ 3 with respect to PXD's 3% occupancy limit. However, unlike for SVD, this is a hardware limit due to the available readout bandwidth, and thus cannot be increased. Also in this case a larger safety factor would be strongly preferable [45].

It should also be considered that a detector which is more robust against backgrounds can ease the machine running at high luminosity, thus increasing overall efficiency and data sample.

Chapter 5

Upgrade benchmark study

In order to evaluate the improvements of an upgrade, one option is to simulate a specific analysis and compare relevant parameters, such as efficiency or resolution of key variables, between the current and the upgraded detectors. In this chapter, this approach is used to evaluate the improvements provided by one of the proposed VTX layouts, the 5-layer layout (see section 3.2); the goal is to provide information for the choice and optimization of the upgrade layout.

$B \rightarrow DX$ reconstruction is important for many Belle II analyses, and it depends critically on the quality of tracking and vertexing in the experiment. Therefore, to evaluate the VTX design, the channel $B^0 \rightarrow D^{*-} \mu^+ \nu_\mu \rightarrow (D^0 \pi) \mu \nu$, with the $D^0 \rightarrow K \pi$ or $\rightarrow K 3\pi$, was chosen for this study. The characteristics of the channel and the reasons behind this choice are detailed in section 5.1. Section 5.2 describes the event generation and the detector simulation, while section 5.3 describes the event reconstruction and candidate selection. Finally, section 5.4 presents the results obtained.

5.1 Channel choice and characteristics

The analysed decay chain is illustrated below, including the indices used to distinguish the pions in the event

$$\begin{aligned} B^0 &\rightarrow D^{*-} \mu^+ \nu_\mu \\ D^{*-} &\rightarrow \bar{D}^0 \pi_{\text{soft}}^+ \\ \bar{D}^0 &\rightarrow \begin{cases} K^+ \pi^- \\ K^+ \pi_1^- \pi_2^- \pi_3^+ \end{cases} \end{aligned} \tag{5.1}$$

where $p_T(\pi_1) > p_T(\pi_2)$. The same names are also used for the conjugate process.

The decay chain is schematically pictured in fig. 5.1, and its main features are detailed below.

- The B^0 is produced from the $\Upsilon(4S)$ resonance at the interaction point (IP) with a small momentum in the centre-of-mass (CM) frame; in the laboratory frame, it decays after flying for a finite, detectable length of $\approx 130 \mu\text{m}$ on average. The ν is undetected, preventing a full reconstruction of the B^0 ; the μ , however, can be used to reconstruct its decay vertex.
- The flight length of the D^* is of $\mathcal{O}(1 \text{ pm})$, and can be neglected; this allows to geometrically constrain the D^* production vertex (i.e. the B^0 decay vertex) and

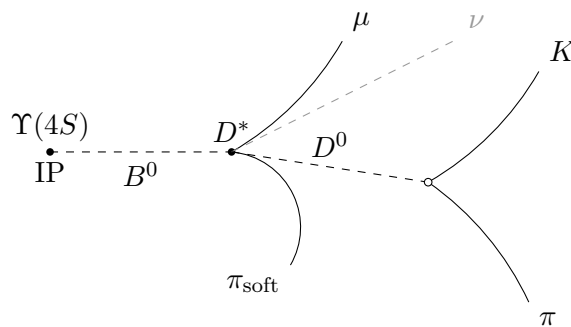


Figure 5.1: Schematic display (not to scale) of a typical $K\pi$ event.

the D^* decay vertex (i.e. the D^0 production vertex) as if they were the same. The decay process of the D^* has a small Q value of ≈ 5.9 MeV, thus the pion typically has a low momentum (hence the name π_{soft}), which can lead to a degradation of tracking efficiency and resolution.

- The D^0 has a finite, detectable flight length of ≈ 100 μm on average; in the selected channels ($K\pi$ and $K3\pi$) it can be completely reconstructed, allowing to resolve its decay vertex. Note that, although the lifetime of the D^0 is ~ 3.5 times shorter than that of the B^0 , the flight lengths of the two particles are similar because of the boost that the D^0 receives from the Q value of the decay chain.

The reconstruction of this decay chain presents several challenges, forcing to heavily rely on the vertex detector and, thus, providing a realistic benchmark for the upgrade.

- In Belle II the position of the IP is well known ($\sigma_x \approx 20$ μm and $\sigma_y \approx 0.2$ μm , while the z resolution is much worse), allowing to set a strong geometric constraint on the first vertex of the decay chain; however, with the unknown flight length of the B^0 , the effectiveness of such constraint on the D^0 production vertex is strongly reduced, forcing the analysis to rely more on the vertex detector.
- The low-momentum π_{soft} tends to spiral in the magnetic field and barely reach the first layers of the vertex detector, thus making its track reconstruction efficiency low and the resolution on its parameters worse than for the other particles; this, in turn, degrades the resolution of the D^0 production vertex.
- The negligible D^* flight length, with the subsequent geometric constraint, allows to recover resolution on the D^0 production vertex by using the μ from the B^0 decay; this, however, increases the complexity of the analysis and the combinatorial background.

Having only charged particles in the final state, the reconstruction of this channel relies almost solely on the tracking detectors; also, the required vertex resolution can only be achieved with the innermost vertex detector(s), thus making it an ideal choice for a VTX benchmark. Moreover, this channel is used in several physics analyses, such as D^0 lifetime measurements [46], but also $\mathcal{R}(D^*)$ measurements [47], allowing to evaluate the projected improvements of VTX in a realistic situation.

Given all this, a list of key variables that impact the analyses' results can be compiled.

- Track finding efficiency, impacting the reconstruction of the final-state particles, in particular of the π_{soft} .

- Impact parameters resolution of the final-state particles, as they are amongst the main outputs of the vertex detector and affect the vertex resolution.
- B^0 reconstruction efficiency, as it impacts the statistics available for analyses.
- Resolution of the D^0 production and decay vertices, as they depend almost only on the vertex detector; also the resolution of the D^0 flight length, which is a key parameter for the D^0 lifetime measurement (although that measurement is performed with prompt D^* produced at the interaction vertex to better exploit the small IP size).

These variables are extracted from the simulations, and the results from VTX are compared with those from VXD to evaluate the performance improvement.

5.2 Event generation and simulation

Event generation and detector response simulation with BASF2 are discussed in section 3.3. Two different strategies can be used for simulating events of the selected channel:

1. generating generic $B^0\bar{B}^0$ events, using all the known decay channels with their branching ratios (BRs), including the selected one;
2. generating only signal events, where only one B^0 decays generically, while the other only decays through the selected channel (with the appropriate ratio between $K\pi$ and $K3\pi$ probabilities).

The first strategy allows to evaluate the effects of physics background on the results; however, the total branching fraction of the selected channel is $\approx 0.4\%$ [4], hence the second strategy could provide the same amount of signal events using $\times 250$ less CPU time. As the physics background is expected to affect the B^0 reconstruction efficiency, the first strategy must be used to obtain reliable results in this sense; however, the lack of physics background of the second strategy should not affect the results concerning vertex resolution or tracking efficiency and resolution.

In this thesis the second strategy was adopted for feasibility reasons, therefore it must be taken into account that the considerations concerning the B^0 reconstruction efficiency may not hold with physics background. While physics background is not considered, beam-induced background is taken into account: it is simulated for nominal conditions and luminosity (i.e. $8 \times 10^{35} \text{ cm}^{-2}\text{s}^{-1}$) and overlaid on the generated events.

The same program is used to perform event generation and simulation both in the current VXD and in the 5-layer VTX, the only differences being the vertex detector geometry and digitizers; also, the same *seed* is used for the random number generator of BASF2, ensuring that exactly the same events are generated. This is necessary to ensure the reliability of the comparison between the results obtained with VXD and VTX.

5.3 Event reconstruction

The reconstruction of the events is performed with BASF2. Like for event generation and simulation, the same program is used both for the current VXD and the 5-layer

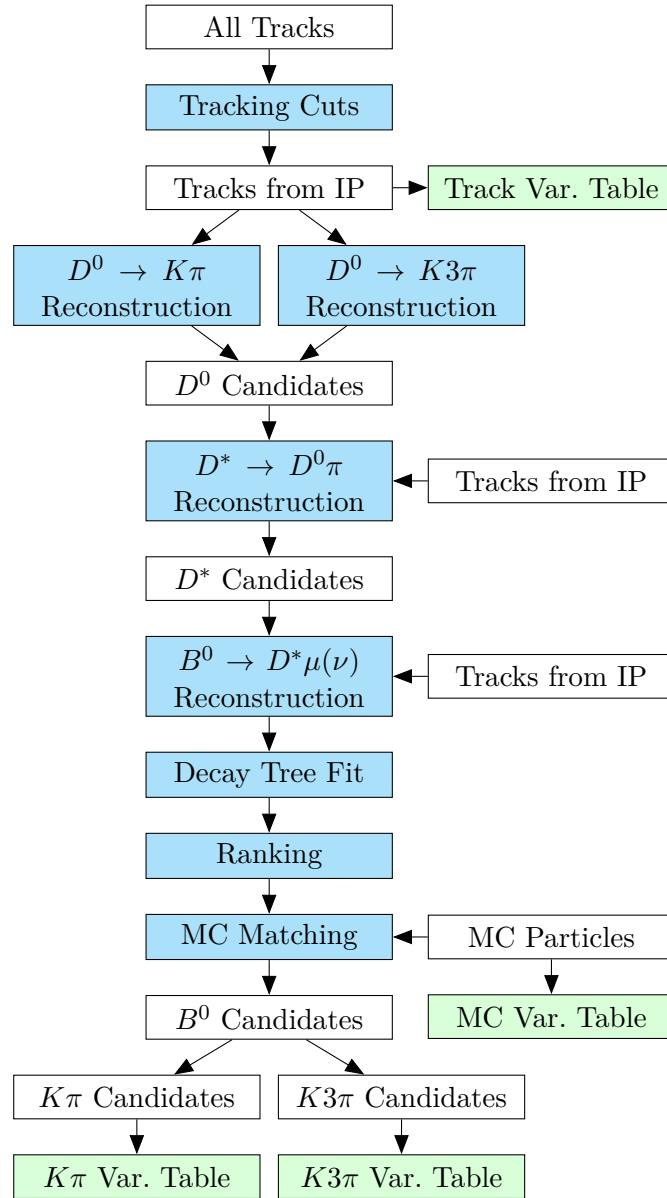


Figure 5.2: Overview of the event reconstruction for the benchmark.

VTX, so that the results obtained in the two cases can be directly compared; the only relevant differences lay in the track reconstruction algorithm (see section 3.4).

The steps of the reconstruction program are outlined in fig. 5.2. After tracks are reconstructed from raw data by the BASF2 algorithm, only those that are relevant for the benchmark are selected using the following cuts.

- Since all of the decays are expected to take place within $\mathcal{O}(1\text{ mm})$ from the IP, the tracks are required to pass close to it; specifically, it is required that $d_0 < 2\text{ cm}$ and $|z_0| < 2\text{ cm}$, where d_0 is the distance between track and IP in the $r\phi$ plane, while z_0 is the distance along the z axis. This requirement is relatively loose, accommodating for tracks with large reconstruction uncertainties; if physics background was present, a tighter cut would probably allow to reduce the number of incorrectly-reconstructed candidates.
- Each track is required to have at least one associated hit from the vertex detector (PXD or SVD, or VTX); this is a common quality cut, although typically also a minimum number of hits from CDC is required, at least for high-transverse-momentum tracks; here the cut on CDC hits is not relevant.
- Particle identification (PID) information could introduce a bias that is difficult to evaluate, hence no PID cut is used. Note, however, that this greatly increases the number of track combinations for the candidates (combinatorial background). Typically, PID is used in the last steps of the analysis.

The decay chain reconstruction can be performed at this point. D^0 candidates are produced by combining pairs of tracks, under the hypothesis of a K and a π , and quartets of tracks, under the hypothesis of a K and three π s. Note that BASF2 only considers physical combinations of tracks, i.e. no track is used twice in the same candidate, the charge must have the right sign and the tracks must cross at a common vertex within the uncertainties; also, the script requires $|\delta M_{D^0}| = |M_{D^0}^{\text{reco}} - M_{D^0}^{\text{PDG}}| < 0.1\text{ GeV}/c^2$.

At this point, D^* candidates are produced by making physical combinations of D^0 candidates with one track, under the π hypothesis; the program requires that $|\delta M_{D^*}| < 0.1\text{ GeV}/c^2$, that $|\delta \Delta M| < 5\text{ MeV}/c^2$ (where $\Delta M = M_{D^*} - M_{D^0}$) and that $p_{D^*}^{\text{CM}} < 2.5\text{ GeV}/c$ (from conservation of momentum). Note that also these cuts are relatively loose.

Finally, B^0 candidates are produced by making physical combinations of D^* candidates with one track, under the μ hypothesis; no requirement can be used on the B^0 mass because of the undetected ν , however all the vertices of the whole decay tree are fitted at once using TreeFitter [48, 49], and candidates are required to have a chi-squared probability of the fit $p_{\chi^2} > 10^{-3}$. The fit uses the constraints that the B^0 is produced at the IP, and that the D^* decays in place (i.e. its production and decay vertices are the same point). The fit also updates the values of reconstructed masses, momenta, etc. using the information from the fitted vertices.

The B^0 candidates in each event are then given a rank, i.e. a number from 1 (best) to the number of candidates in the event (worst), for each of the following variables:

- $|\delta M_{D^0}|$ (sorted in ascending order);
- $|\delta M_{D^*}|$ (sorted in ascending order);
- p_{χ^2} (sorted in descending order);

- $M_{B^0}^{\text{reco}}$ (sorted in descending order).

These ranks can be used later to perform best-candidate selection (BCS). The rank on $M_{B^0}^{\text{reco}}$ is found to be particularly effective at rejecting candidates where the wrong track is used for the μ ; this is useful for comparing B^0 reconstruction efficiencies, as shown in section 5.4.2, but would probably become unnecessary if PID information was used.

The particles in the candidates are then associated to the “true” Monte Carlo (MC) particles, allowing to determine whether the reconstruction is correct, and the errors on the estimated variables. BASF2 considers a candidate to be “good” or “signal” if it is able to associate each reconstructed or tracked particle with a MC particle, and the relevant variables (track parameters, mass, momentum, identity, etc.) are correct within the estimated uncertainty; candidates with missing particles, incorrectly reconstructed particles or fake particles (i.e. that cannot be associated to any MC particle) are considered “bad”, although an exception is made for the ν and the B^0 variables that depend on it.

At this point, interesting variables are saved in a table with one B^0 candidate per row; the variables include:

- the classification of the candidate (good or bad) and its ranks;
- masses and momenta of each particle: reconstructed values with their estimated uncertainty, true MC values, residuals (see eq. 5.3) and pulls (see eq. 5.4);
- track and impact parameters for each final-state particle: reconstructed and true MC values, residuals and pulls;
- vertex coordinates and flight length for the composite particles (i.e. D^0 , D^* and B^0): reconstructed and true MC values, residuals and pulls.

There are two different tables for B^0 candidates with $D^0 \rightarrow K\pi$ and $\rightarrow K3\pi$, as it is more practical to study them separately.

Also, two tables are made with one MC B^0 per row (one for $K\pi$, one for $K3\pi$), as they are necessary to compute efficiencies (both global and in bins of specific variables), and one table is made with one tracked particle per row, as it is necessary to study tracking efficiency and resolution. The particles are put in these last tables independently of their usage in the candidates.

5.4 Results

10 000 signal-only events were simulated and reconstructed both with the current VXD and with VTX; as mentioned in section 5.2, exactly the same events are used in both cases.

In this section the resulting improvements in key aspects of the analysis are presented: section 5.4.1 shows the increase of track finding efficiency, which affects the event reconstruction efficiency (i.e. the B^0 reconstruction efficiency) as described in section 5.4.2; section 5.4.3 shows the improvements in terms of impact parameters resolution of the particles used in the B^0 reconstruction; finally section 5.4.4 presents the improvements in terms of vertex resolution and, for the D^0 , flight length resolution.

5.4.1 Tracking efficiency

Fig. 5.3 shows the distribution of the number of tracks per event in the simulations with the two detectors. Tracks are classified as “good” if they are matched to an actual (MC) particle and the track parameters are reconstructed correctly (within the estimated uncertainty), “bad” if they are matched to a MCParticle but the parameters are incorrectly reconstructed, and “fake” if they are not matched to any MCParticle. Good and bad tracks are classified as “clones” if there is (at least) another track that is matched to the same MCParticle.

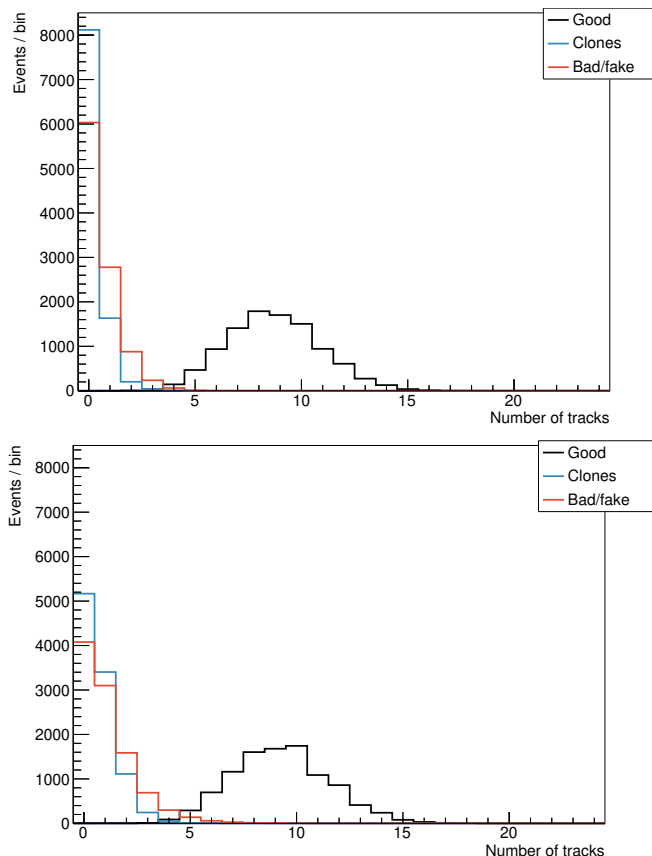


Figure 5.3: Distribution of the number of tracks per event in the simulation (current VXD above, VTX below).

VTX is able to find a larger number of tracks than VXD: tab. 5.1 shows that this amounts to $\sim 10\%$ more good tracks, at the cost of higher (approximately double) clone and bad/fake rates. It is to be noted, however, that unlike the tracking algorithm for VXD, the one for VTX has not yet been optimized to reject bad, fake and clone tracks, as mentioned in section 3.3; it is thus reasonable to assume that the clone and bad/fake rates can be reduced. While applying additional cuts to exclude clone, bad and fake tracks may have a negative impact on the finding efficiency and reduce the number of good tracks found, fig. 5.4 suggests that most of the newly found tracks are actually from low-transverse-momentum particles (i.e. with $p_T \lesssim 0.1 \text{ GeV}/c$) that are undetectable for VXD because it cannot use the two PXD layers for track finding.

| | VXD | VTX |
|----------|----------------|----------------|
| | [tracks/event] | [tracks/event] |
| Good | 8.65 | 9.25 |
| Clone | 0.22 | 0.67 |
| Bad/fake | 0.55 | 1.10 |

Table 5.1: Average number of tracks found per event in the simulation.

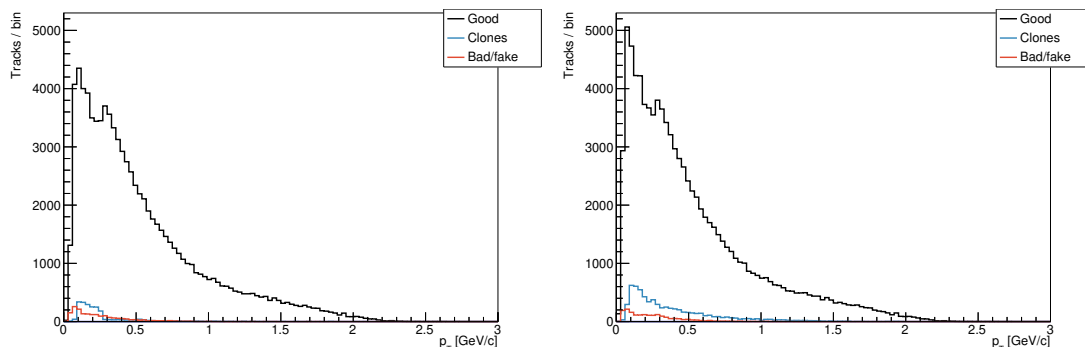


Figure 5.4: Transverse momentum distribution of the tracks in the simulation (current VXD on the left, VTX on the right). The true (MC) transverse momentum is used.

5.4.2 Reconstruction efficiency

As the μ track is necessary to maximise the D^0 production vertex resolution, the B^0 reconstruction efficiency is taken into account. The following equations define the key parameters: efficiency and purity

$$\text{efficiency} = \frac{N_{\text{signal}}}{N_{\text{MC}}}, \quad \text{purity} = \frac{N_{\text{signal}}}{N_{\text{signal}} + N_{\text{bad}}} \quad (5.2)$$

where N_{MC} refers to the number of generated signal particles, while N_{signal} and N_{bad} refers to reconstructed candidates. As the fraction of background events affects the resolution of the physical analysis, efficiency comparisons only make sense if the samples compared have similar purities. As no physics background events were simulated, the main source of background in this analysis is the combinatorial background, i.e. candidates reconstructed from the wrong combination of tracks. This means that an increase in efficiency found by this analysis may not be the same that would be found with physics background; still, the possibility of VTX to track particles with very low transverse momentum, which are beyond the possibilities of the current VXD, suggests that VTX should be capable of a higher B^0 reconstruction efficiency.

Tab. 5.2 reports the number of MC B^0 s and reconstructed candidates for the two detector layouts. While for the $K\pi$ channel the VXD and VTX samples have similar purities, this is not true for the $K3\pi$ channel, hence candidate selection must be modified in order to compare the results.

One variable on which no cut was applied is the reconstructed mass of the B^0 : this has a very wide, non-peaking distribution due to the undetectable neutrino, as shown in fig. 5.5. It appears, however, that in bad candidates M_{B^0} tends to have be smaller than in signal candidates; this suggests that using the rank on M_{B^0} to perform a best-candidate selection (i.e. for each event, only the candidate with the highest M_{B^0} is considered) might improve the sample purity: the results of such a selection are shown

| | $K\pi$ | | $K3\pi$ | |
|-----------------------------|--------|------|---------|---------|
| | VXD | VTX | VXD | VTX |
| MC signal B^0 s | 3276 | | 6752 | |
| Signal candidates | 1084 | 1931 | 1340 | 3360 |
| Bad candidates | 3187 | 7017 | 53 733 | 218 117 |
| Signal candidates per event | 0.33 | 0.59 | 0.20 | 0.50 |
| Bad candidates per event | 0.97 | 2.1 | 8.0 | 32 |
| Efficiency | 33 % | 59 % | 20 % | 50 % |
| Purity | 25 % | 22 % | 2.4 % | 1.5 % |

Table 5.2: Summary of the number of candidates reconstructed from the simulation. No best-candidate selection is applied. Efficiency and purity are defined by eq. 5.2.

in fig. 5.6. Since in this analysis particle identification information is not used (to avoid introducing a bias which might be complicated to evaluate), it is likely that many of these bad candidates simply use the wrong track for the μ ; hence, using particle identification could probably outperform the best-candidate selection described. The other ranks (see section 5.3) have been tested as well, but the one on M_{B^0} has the best performance.

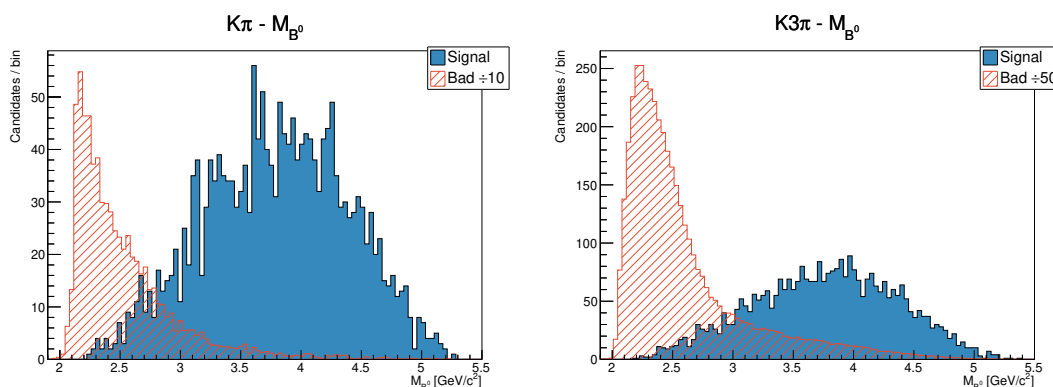


Figure 5.5: Distribution of the B^0 mass reconstructed by VTX in the $K\pi$ (left) and $K3\pi$ (right) channels. No best-candidate selection is applied. Notice the scaling factor applied to bad candidates to make the signal candidates distribution visible.

Tab. 5.3 reports the number of MC B^0 s and reconstructed candidates for the two detector layouts after applying the best-candidate selection on M_{B^0} . With fairly similar purities of the VXD and VTX samples it is now possible to compare the B^0 reconstruction efficiencies: VTX is 50 % to 70 % more efficient than VXD. Fig. 5.7 compares the efficiencies as a function of the transverse momentum of the π_{soft} : while a larger improvement at low p_T is visible, it appears that the overall increase in efficiency depends only in part on the better π_{soft} reconstruction efficiency at low momentum.

5.4.3 Impact parameters resolution

The impact parameters d_0 and z_0 (i.e. the distances of the point of closest approach of a track to the IP in the $r\phi$ plane and along the z axis, respectively) of the final-state particles are important for the determination of the vertices, hence their resolution is a key parameter for the vertex detector. In this analysis the resolution of the impact parameters of each final-state particle (μ , π_{soft} , K , etc.) is evaluated separately.

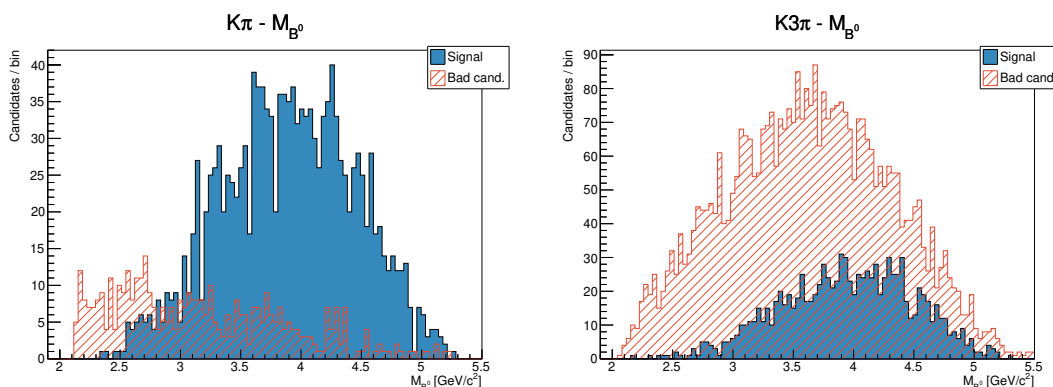


Figure 5.6: Distribution of the B^0 mass reconstructed by VTX in the $K\pi$ (left) and $K3\pi$ (right) channels. Best-candidate selection on M_{B^0} is applied. Notice that no scaling factor is applied to bad candidates in this case.

| | $K\pi$ | | $K3\pi$ | |
|-----------------------------|--------|------|---------|------|
| | VXD | VTX | VXD | VTX |
| MC signal B^0 s | 3276 | | 6752 | |
| Signal candidates | 954 | 1443 | 581 | 1037 |
| Bad candidates | 381 | 426 | 2267 | 3901 |
| Signal candidates per event | 0.29 | 0.44 | 0.086 | 0.15 |
| Bad candidates per event | 0.12 | 0.13 | 0.34 | 0.58 |
| Efficiency | 29 % | 44 % | 8.6 % | 15 % |
| Purity | 71 % | 77 % | 20 % | 21 % |

Table 5.3: Summary of the number of candidates reconstructed from the simulation. Best-candidate selection on M_{B^0} is applied. Efficiency and purity are defined by eq. 5.2.

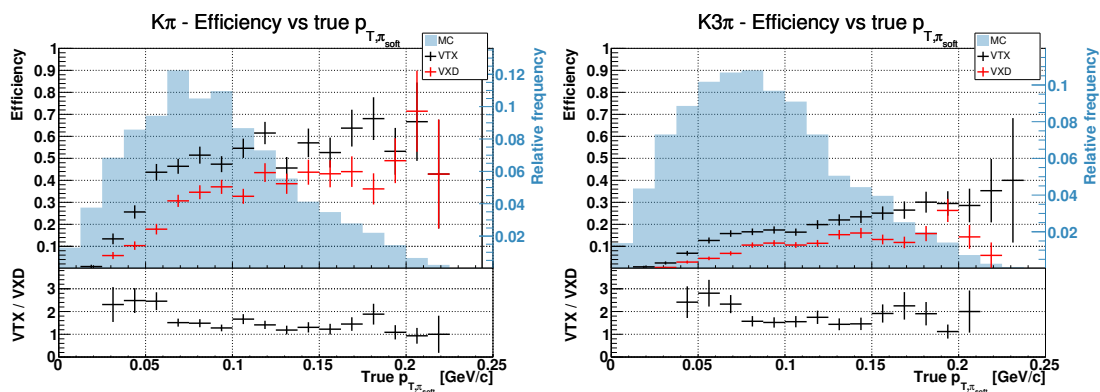


Figure 5.7: Comparison of the B^0 reconstruction efficiencies of VXD and VTX, in the $K\pi$ (left) and $K3\pi$ (right) channels, vs the transverse momentum of the π_{soft} . Best-candidate selection on M_{B^0} is applied. The relative distribution of the MC particles is reported in blue, for reference.

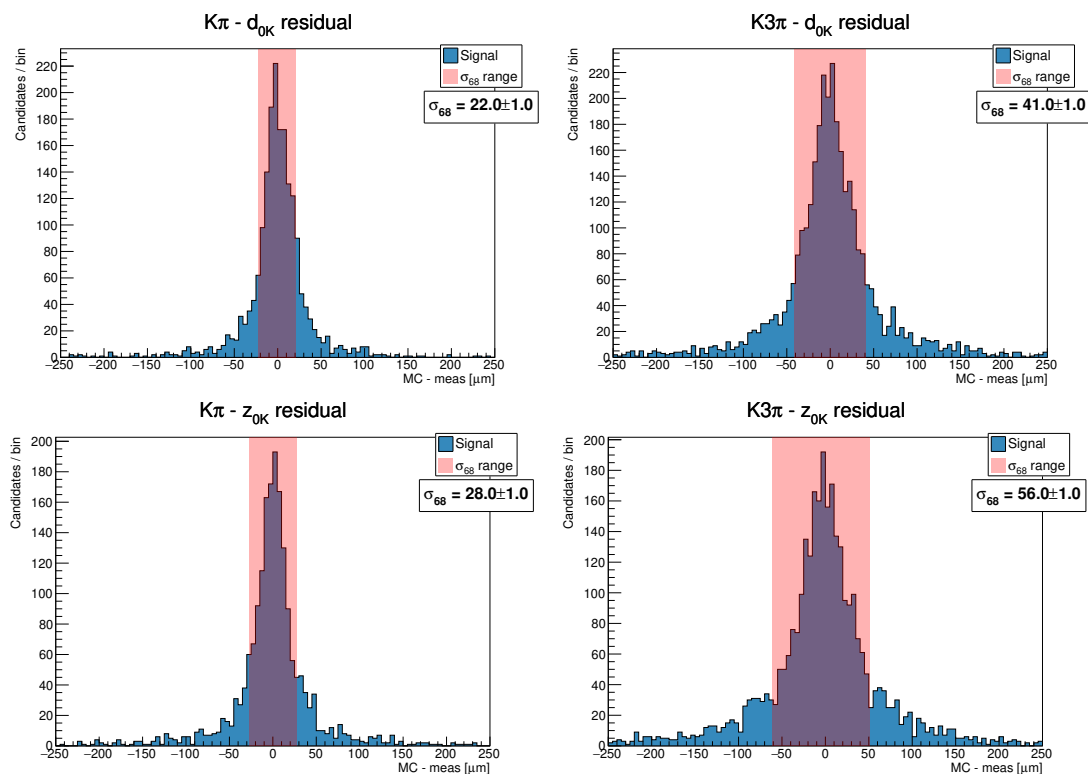


Figure 5.8: Distributions of d_0 (top) and z_0 (bottom) residuals for the K in the $K\pi$ (left) and $K3\pi$ (right) channels, using VTX.

The resolution on a variable x can be defined as the width of the distribution of the variable's residuals, which are given by

$$\text{residual}_x = x_{\text{MC}} - x_{\text{measured}} \quad (5.3)$$

Example residual distributions (those of the K) are shown in fig. 5.8 and 5.9; z_0 and d_0 distribution for the various particles all have similar features. An attempt was made to fit the distributions with a gaussian function, however this proved that non-gaussian tails are present; while a more complex model function (e.g. double gaussian) could be tried for the fit, the approach adopted in this analysis is using the σ_{68} statistic, also used in several SVD resolution analyses. σ_{68} is defined as the width of the interval that contains 68% of the entries, and has half of the remaining entries (i.e. 16%) on its left and the other half on its right. In this analysis, σ_{68} is computed on a fine-binned histogram for practical reasons; the width of the bins is assumed as uncertainty. Only signal candidates are considered; no best-candidate selection is used, as it does not appear to produce any difference except from reducing the available statistics (an example of this is shown in fig. 5.10).

The resulting resolutions are summarised in tab. 5.4. For both detectors, resolutions range from $\mathcal{O}(10\mu\text{m})$ to $\mathcal{O}(1\text{mm})$, depending on the particle. As expected, particles that have a greater transverse momentum on average also have a better resolution (the larger number of detector layers crossed and the resulting larger number of hits are beneficial to the tracking): the π_{soft} has the worst one, while the μ has the best one; also π_1 has a better resolution than π_2 (the two have the same charge, and BASF2 does

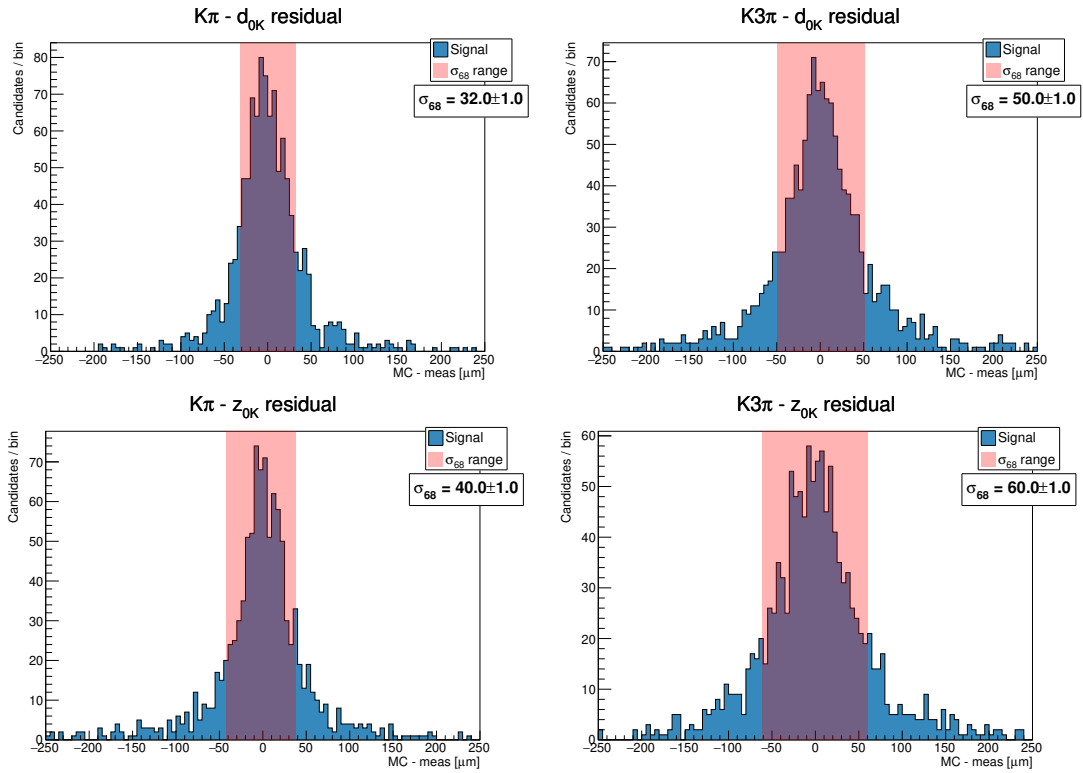


Figure 5.9: Distributions of d_0 (top) and z_0 (bottom) residuals for the K in the $K\pi$ (left) and $K3\pi$ (right) channels, using VXD.

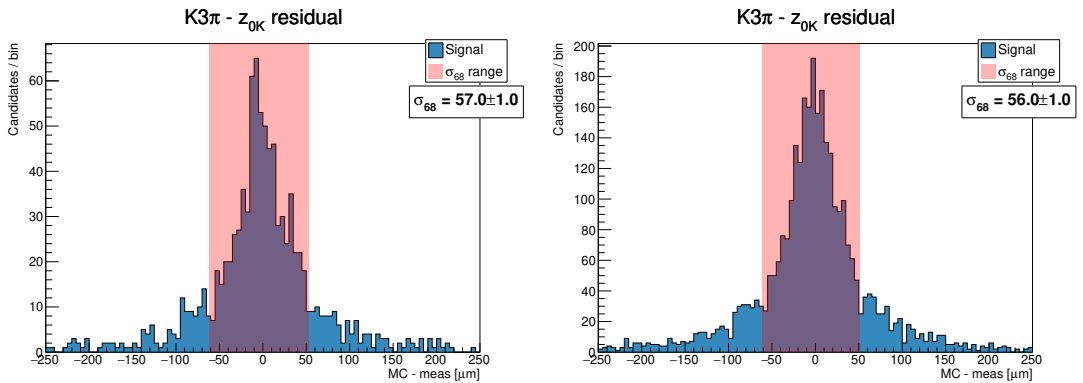


Figure 5.10: Comparison of the z_0 residual distribution for the K in the $K3\pi$ channel with (left) and without (right) best-candidate selection, using VTX.

| | | VXD res. | VTX res. | VTX/VXD ratio | |
|---------------------|---------------------|-------------------|-------------------|-----------------|-----------------|
| | | [μm] | [μm] | | |
| $K\pi$ | K | d_0 | 32 ± 1 | 22 ± 1 | 0.67 ± 0.05 |
| | | z_0 | 40 ± 1 | 28 ± 1 | 0.69 ± 0.04 |
| | μ | d_0 | 23 ± 1 | 16 ± 1 | 0.67 ± 0.07 |
| | | z_0 | 28 ± 1 | 19 ± 1 | 0.68 ± 0.06 |
| | π | d_0 | 27 ± 1 | 21 ± 1 | 0.79 ± 0.07 |
| | | z_0 | 37 ± 1 | 25 ± 1 | 0.66 ± 0.04 |
| π_{soft} | d_0 | 460 ± 10 | 260 ± 10 | 0.57 ± 0.03 | |
| | z_0 | 600 ± 20 | 340 ± 20 | 0.55 ± 0.05 | |
| $K3\pi$ | K | d_0 | 51 ± 1 | 41 ± 1 | 0.81 ± 0.04 |
| | | z_0 | 61 ± 1 | 56 ± 1 | 0.93 ± 0.03 |
| | μ | d_0 | 23 ± 1 | 16 ± 1 | 0.69 ± 0.08 |
| | | z_0 | 29 ± 1 | 20 ± 1 | 0.68 ± 0.06 |
| | π_1 | d_0 | 41 ± 1 | 32 ± 1 | 0.77 ± 0.04 |
| | | z_0 | 51 ± 1 | 40 ± 1 | 0.79 ± 0.04 |
| | π_2 | d_0 | 102 ± 1 | 86 ± 1 | 0.84 ± 0.02 |
| | | z_0 | 135 ± 1 | 110 ± 1 | 0.81 ± 0.01 |
| | π_3 | d_0 | 66 ± 1 | 50 ± 1 | 0.75 ± 0.03 |
| | | z_0 | 80 ± 1 | 66 ± 1 | 0.82 ± 0.02 |
| | π_{soft} | d_0 | 370 ± 10 | 240 ± 10 | 0.65 ± 0.04 |
| | | z_0 | 440 ± 20 | 320 ± 20 | 0.73 ± 0.08 |

Table 5.4: Summary of the impact parameters resolution for the final state particles.

not adopt any particular sorting order, but to ensure results comparability they are sorted by transverse momentum by the analysis program, as mentioned in section 5.1).

Regardless of the resolutions of individual particles, VTX appears to improve resolution with respect to VXD by $\sim 25\%$ on average.

It is also important to verify that the uncertainties on the reconstructed parameters are correctly estimated: this can be done by using the pull distributions. The pull of a variable x is defined as

$$\text{pull}_x = \frac{x_{\text{MC}} - x_{\text{measured}}}{\sigma_x} = \frac{\text{residual}_x}{\sigma_x} \quad (5.4)$$

where σ_x is the estimated uncertainty on the measure. If the uncertainties are correctly estimated, the distribution of the pull should be gaussian with $\sigma = 1$. The pull distributions of the impact parameters are fitted with a gaussian function, and are all found to be in good agreement with this model, and to have a $\sigma \approx 1$. Fig. 5.11 shows this for some pull distributions (those of the K reconstructed with VTX) as an example.

5.4.4 Vertex and flight length resolution

Vertex and flight length resolution is evaluated in the same way as impact parameters resolution, as presented in the previous section: the resolution is given by the σ_{68} of the residuals distribution, computed on a fine-binned histogram filled with signal candidates without using any best-candidate selection. Vertex resolution is evaluated with the resolution of the vertex cartesian coordinates; as the cartesian coordinates are typically correlated, the resolution on the D^0 flight length cannot be inferred in an immediate

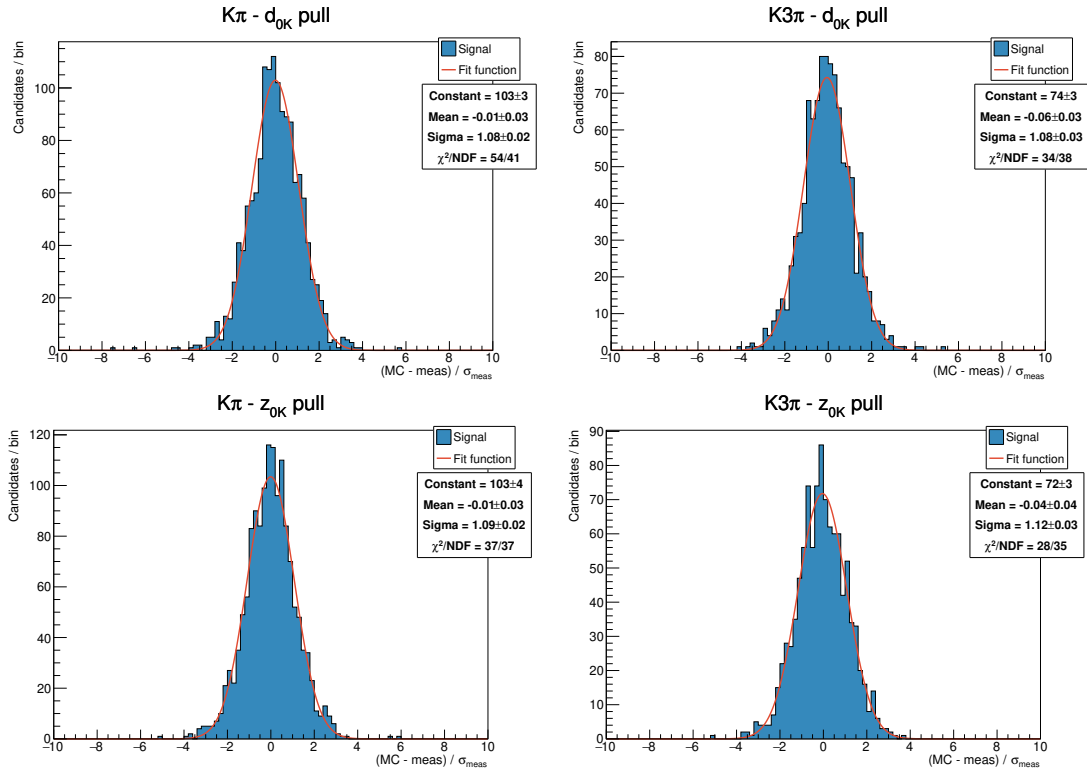


Figure 5.11: Distributions of d_0 (top) and z_0 (bottom) pulls for the K in the $K\pi$ (left) and $K3\pi$ (right) channels, using VTX. Pulls are fitted with a gaussian function.

manner, hence it is shown separately. An example residual distribution (that of the D^0 flight length) is shown in fig. 5.12.

Tab. 5.5 summarises the vertex and flight length resolutions for the various particles in the two channels, and for the two detectors. The current VXD has a vertex resolution of 25–30 μm and a D^0 flight length resolution of $\approx 55 \mu\text{m}$, while VTX has a vertex resolution of 20–25 μm and a D^0 flight length resolution of $\approx 45 \mu\text{m}$. VTX appears to improve the vertex and flight length resolution by $\sim 20\%$.

This benchmark study proves not only that VTX has a good performance, but also that it is able to improve the tracking and vertexing capabilities of the experiment in a significant manner. As these are key features in virtually all physics analyses, it follows that VTX may have a large positive impact on the results of Belle II. Also, this benchmark forms a basis for further optimization of the VTX layout and design.

| | | VXD res. | VTX res. | VTX/VXD ratio |
|---------|---------------------|-------------------|-------------------|-----------------|
| | | [μm] | [μm] | |
| B^0 | x_{decay} | 24 ± 1 | 17 ± 1 | 0.71 ± 0.07 |
| | y_{decay} | 23 ± 1 | 18 ± 1 | 0.78 ± 0.08 |
| | z_{decay} | 24 ± 1 | 17 ± 1 | 0.71 ± 0.07 |
| $K\pi$ | x_{decay} | 27 ± 1 | 20 ± 1 | 0.72 ± 0.06 |
| | y_{decay} | 25 ± 1 | 20 ± 1 | 0.80 ± 0.07 |
| | z_{decay} | 26 ± 1 | 18 ± 1 | 0.71 ± 0.07 |
| | l_{flight} | 56 ± 2 | 44 ± 2 | 0.77 ± 0.06 |
| B^0 | x_{decay} | 24 ± 1 | 20 ± 1 | 0.83 ± 0.08 |
| | y_{decay} | 25 ± 1 | 20 ± 1 | 0.80 ± 0.07 |
| | z_{decay} | 25 ± 1 | 19 ± 1 | 0.76 ± 0.07 |
| $K3\pi$ | x_{decay} | 27 ± 1 | 23 ± 1 | 0.85 ± 0.07 |
| | y_{decay} | 28 ± 1 | 22 ± 1 | 0.80 ± 0.07 |
| | z_{decay} | 28 ± 1 | 21 ± 1 | 0.75 ± 0.06 |
| | l_{flight} | 56 ± 2 | 46 ± 2 | 0.82 ± 0.07 |

Table 5.5: Summary of the impact parameters resolution for the final state particles. The D^* decays in place, at the decay vertex of the B^0 , which is thus also the production vertex of the D^0 .

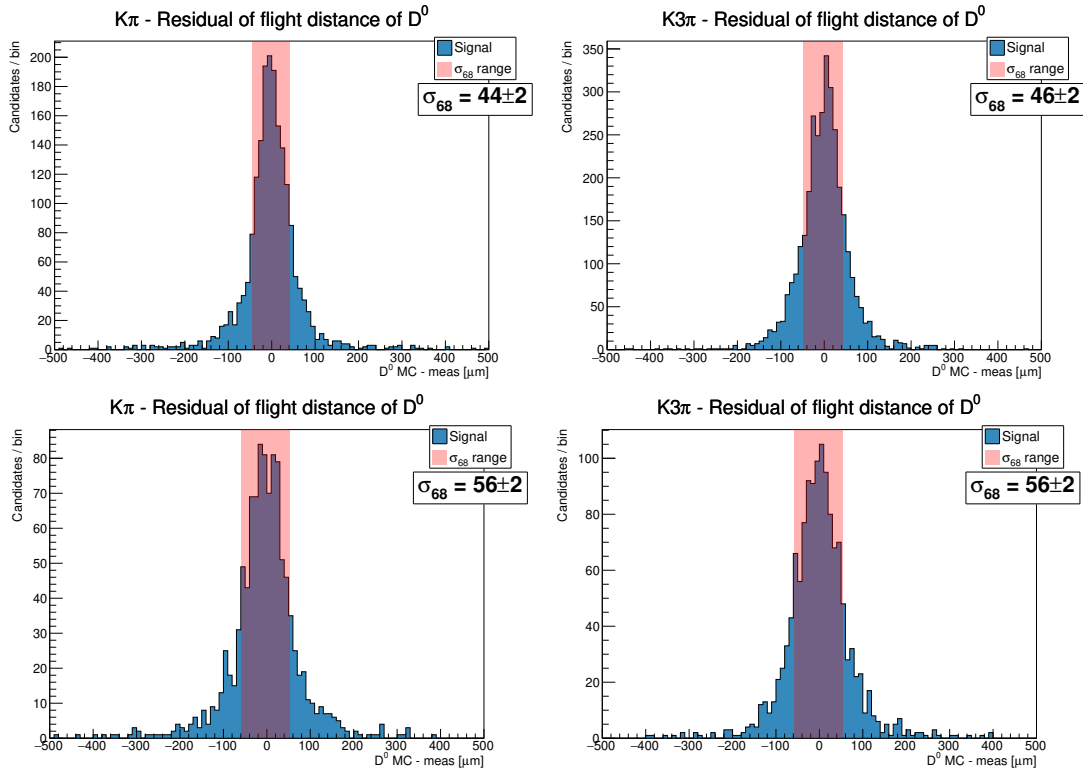


Figure 5.12: Distributions of residuals of the D^0 flight length in the $K\pi$ (left) and $K3\pi$ (right) channels, using VTX (top) and VXD (bottom).

Chapter 6

Conclusions

This thesis presents a systematic study of the radiation damage in SVD in the first 2.5 years of operations of the experiment. Online tools for consistently monitoring radiation-damage-sensitive parameters (i.e. depletion voltage, leakage current and strip noise) on all 172 SVD sensors were developed. Furthermore, an improved method for estimating the dose in SVD was developed, which introduces corrections for several sources of bias, leading to a re-evaluation of the total integrated dose in L3 by a factor $\sim 1/3$ with respect to the previous study; the new method also provides more accurate results for the outermost SVD layers.

In these first 2.5 years of operations, working with beam currents and luminosity much lower than the design ones, a dose of ≈ 70 krad was absorbed by L3 mid-plane sensors (the ones that are subject to the largest amount of radiation). The evolution of the radiation-sensitive parameters as a function of the total integrated dose was studied, and reasonable agreement with the expectations was found. Furthermore, such studies allow to extrapolate radiation damage effects and their impact on performance in the future, which is of paramount importance for SVD operations and for future upgrade design.

Although the presently expected background level at design luminosity is acceptable, higher safety margins would be desirable to account for the large uncertainties on these extrapolations. For this reason, several upgrade proposals for the vertex detector are under study: this thesis presents a study of the performance improvements of a specific upgrade proposal, VTX, based on monolithic depleted CMOS pixel sensors. For this purpose, a specific channel is simulated, $B^0 \rightarrow (D^0\pi)_{D^*}\mu\nu$ with $D^0 \rightarrow K\pi, K\pi\pi\pi$: such channel is also used in several physics analyses, thus providing realistic benchmark conditions.

Due to its different design, VTX is expected to have a higher track finding efficiency; in particular, due to the fact that VTX allows to exploit the two innermost layers for track finding (unlike PXD, whose layers are only used to maximise the resolution of tracks found by SVD or CDC), VTX is expected to perform better with low-transverse-momentum tracks. The simulation results confirm this expectation, showing that VTX is able to reconstruct tracks down to 50 MeV/c, while the VXD efficiency drops to zero at around 75 MeV/c. This higher track finding efficiency results in a higher B^0 reconstruction efficiency, up to 70 % better, although this result was computed without taking any physics background into account, hence the improvement in an actual analysis might be smaller.

Also, the all-pixel design with smaller pitch of VTX is expected to provide an im-

provement in track and vertex resolution. The simulation indeed shows that the impact parameters resolution improves by $\mathcal{O}(25\%)$, and that the vertex position resolution and the D^0 flight length resolution improve by $\sim 20\%$. As the vertex resolution is instrumental for reducing combinatorial background, and the flight length resolution is a key variable for lifetime and time-dependent CP violation studies, such a resolution improvement could have a large positive impact on physics results.

This work demonstrates the good performance of the VTX detector, and forms a basis for further optimization of its design.

Bibliography

- [1] E. Kou et al. The Belle II Physics Book. *Progress of Theoretical and Experimental Physics*, 2019(12), Dec 2019. Cited on pages 1, 7, 11, 17 and 39.
- [2] W. N. Cottingham and D. A. Greenwood. *An Introduction to the Standard Model of Particle Physics*. Cambridge University Press, 2nd edition, 2007. Cited on page 3.
- [3] Nicola Cabibbo. Unitary Symmetry and Leptonic Decays. *Phys. Rev. Lett.*, 10:531–533, 1963. Cited on page 4.
- [4] P.A. Zyla et al. Review of Particle Physics. *PTEP*, 2020(8):083C01, 2020. Cited on pages 4, 6, 62 and 71.
- [5] Y. Grossman and P. Tanedo. Just a Taste: Lectures on Flavor Physics. *Anticipating the Next Discoveries in Particle Physics*, May 2018. Cited on page 4.
- [6] J. Charles et al. CP violation and the CKM matrix: assessing the impact of the asymmetric B factories. *The European Physical Journal C*, 41(1):1–131, May 2005. Updated results and plots available at <http://ckmfitter.in2p3.fr/>. Cited on page 6.
- [7] V. Bertacchi et al. Track finding at Belle II. *Computer Physics Communications*, 259:107610, Feb 2021. Cited on pages 10, 21, 34 and 42.
- [8] A. J. Bevan et al. The Physics of the B Factories. *The European Physical Journal C*, 74(11), Nov 2014. Cited on page 11.
- [9] K. Akai, K. Furukawa, and H. Koiso. SuperKEKB collider. *Nucl. Instrum. Meth. A*, 907:188–199, Nov 2018. Cited on page 11.
- [10] Y. Ohnishi et al. Accelerator design at SuperKEKB. *PTEP*, 2013:03A011, 2013. Cited on pages 11, 13 and 15.
- [11] SuperB Collaboration. SuperB Technical Design Report, 2013. Cited on page 12.
- [12] T. Abe et al. Achievements of KEKB. *Progress of Theoretical and Experimental Physics*, 2013(3), 03 2013. Cited on page 13.
- [13] Y. Ohnishi. Overview of 2020c and 2021a/b Run. In *The 25th KEKB Accelerator Review Committee*, Sep 2021. Restricted access. Cited on page 13.
- [14] P. M. Lewis et al. First measurements of beam backgrounds at SuperKEKB. *Nucl. Instrum. Meth. A*, 914:69–144, Jan 2019. Cited on page 14.

- [15] The Belle II SVD Collaboration. The Design, Construction, Operation and Performance of the Belle II Silicon Vertex Detector. In preparation, to be submitted to the Journal of Instrumentation. Cited on pages 14, 33, 34, 36, 37, 42, 50, 56, 59, 61, 63, 66, 67 and 68.
- [16] M. Aiba. Injection: Electron beams. *CERN Yellow Rep. School Proc.*, 5:121, 2018. Cited on pages 15 and 16.
- [17] T. Hara, T. Kuhr, and Y. Ushiroda. Belle II Coordinate System and Guideline of Belle II Numbering Scheme, Aug 2011. Technical note. Cited on page 18.
- [18] T. Abe et al. Belle II Technical Design Report, 2010. Cited on pages 20, 22, 24, 25, 26, 27, 33 and 34.
- [19] M. J. French et al. Design and results from the APV25, a deep sub-micron CMOS front-end chip for the CMS tracker. *Nucl. Instrum. Meth. A*, 466:359–365, 2001. Cited on page 21.
- [20] I. Adachi et al. Detectors for extreme luminosity: Belle II. *Nucl. Instrum. Meth. A*, 907:46–59, 2018. Cited on pages 22, 24 and 26.
- [21] T. Kuhr et al. The Belle II Core Software. *Computing and Software for Big Science*, 3(1), Nov 2018. Cited on page 29.
- [22] R. Brun and F. Rademakers. ROOT: An object oriented data analysis framework. *Nucl. Instrum. Meth. A*, 389:81–86, 1997. See also <https://root.cern/>. Cited on page 29.
- [23] D. J. Lange. The EvtGen particle decay simulation package. *Nucl. Instrum. Meth. A*, 462(1):152–155, 2001. See also <https://evtgen.hepforge.org/>. Cited on pages 29 and 41.
- [24] S. Agostinelli et al. GEANT4 – a simulation toolkit. *Nucl. Instrum. Meth. A*, 506:250–303, 2003. See also <https://geant4.web.cern.ch/>. Cited on pages 29 and 41.
- [25] R. S. Muller, T. I. Kamins, M. Chan, and P. K. Ko. *Device electronics for integrated circuits*, volume 2. Wiley, Jan 1986. Cited on page 31.
- [26] Manfred Valentan. *The Silicon Vertex Detector for b-tagging at Belle II*. PhD thesis, Vienna, Tech. U., Atominst., 2013. Cited on pages 31, 32 and 62.
- [27] K. Adamczyk et al. The Belle II silicon vertex detector assembly and mechanics. *Nucl. Instrum. Meth. A*, 845:38–42, 2017. Cited on page 34.
- [28] S. Bacher et al. Performance of the diamond-based beam-loss monitor system of Belle II. *Nucl. Instrum. Meth. A*, 997:165157, 2021. Cited on page 36.
- [29] G. Bassi et al. Calibration of diamond detectors for dosimetry in beam-loss monitoring. *Nucl. Instrum. Meth. A*, 1004:165383, 2021. Cited on page 36.
- [30] O. Alonso et al. Proposal of an all-layer monolithic pixel vertex detector for the Belle II upgrade. Internal note, restricted access. Cited on pages 38 and 42.

- [31] I. Caicedo et al. The Monopix chips: depleted monolithic active pixel sensors with a column-drain read-out architecture for the ATLAS Inner Tracker upgrade. *Journal of Instrumentation*, 14(06):C06006–C06006, Jun 2019. Cited on page 38.
- [32] T. Sjöstrand et al. An introduction to PYTHIA 8.2. *Computer Physics Communications*, 191:159–177, Jun 2015. See also <https://pythia.org/>. Cited on page 41.
- [33] K. Oide et al. Strategic Accelerator Design (SAD). See <https://acc-physics.kek.jp/SAD/>. Cited on page 42.
- [34] G. Kramberger. *Particle Physics Reference Library: Volume 2: Detectors for Particles and Radiation*, chapter 21, pages 965–1034. Springer International Publishing, 2020. Cited on page 46.
- [35] M. Moll. *Radiation damage in silicon particle detectors: Microscopic defects and macroscopic properties*. PhD thesis, Hamburg U., 1999. Cited on pages 46, 47, 48 and 67.
- [36] P. Riedler. *Radiation Damage Effects and Performance of Silicon Strip Detectors using LHC Readout Electronics*. PhD thesis, Vienna U., 1998. Cited on pages 46 and 48.
- [37] J. Zhang et al. Investigation of X-ray induced radiation damage at the Si-SiO₂ interface of silicon sensors for the European XFEL. *Journal of Instrumentation*, 7(12):C12012–C12012, Dec 2012. Cited on page 48.
- [38] H.F.-W. Sadrozinski et al. Total dose dependence of oxide charge, interstrip capacitance and breakdown behavior of sLHC prototype silicon strip detectors and test structures of the SMART collaboration. *Nucl. Instrum. Meth. A*, 579(2):769–774, 2007. Proceedings of the 6th "Hiroshima" Symposium on the Development and Application of Semiconductor Detectors. Cited on page 48.
- [39] H. Tanigawa et al. Beam background study for the belle ii silicon vertex detector. *Nucl. Instrum. Meth. A*, 982:164580, 2020. Cited on page 49.
- [40] The BaBar Collaboration. The BaBar detector: Upgrades, operation and performance. *Nucl. Instrum. Meth. A*, 729:615–701, 2013. Cited on page 49.
- [41] S. Bettarini et al. Measurement of the charge collection efficiency after heavy non-uniform irradiation in BABAR silicon detectors. *IEEE Transactions on Nuclear Science*, 52(4):1054–1060, 2005. Cited on page 49.
- [42] G. Rizzo et al. The Belle II Silicon Vertex Detector: Performance and Operational Experience in the First Year of Data Taking. *JPS Conf. Proc.*, 34:010003, 2021. Cited on page 56.
- [43] R Aaij et al. Performance of the LHCb Vertex Locator. *Journal of Instrumentation*, 9(09):P09007–P09007, Sep 2014. Cited on page 60.
- [44] Z. Wang. SVD beam background study. In *39th Belle II General Meeting*. The Belle II Collaboration, Jun 2021. Restricted access. Cited on page 67.

- [45] K. Nakamura. Upgrade of the Belle II Inner Detector, Sep 2021. Presented at VERTEX2021 workshop, proceedings to be published in Proceedings of Science. Cited on page 68.
- [46] The Belle II collaboration. Precise measurement of the D^0 and D^+ lifetimes at Belle II, 2021. Submitted to Phys. Rev. Lett. arXiv:2108.03216. Cited on page 70.
- [47] G. Caria et al. Measurement of $\mathcal{R}(D)$ and $\mathcal{R}(D^*)$ with a semileptonic tagging method. *Phys. Rev. Lett.*, 124(16):161803, 2020. Cited on page 70.
- [48] J.-F. Krohn, F. Tenchini, et al. Global decay chain vertex fitting at Belle II. *Nucl. Instrum. Meth. A*, 976:164269, 2020. Cited on page 73.
- [49] W. D. Hulsbergen. Decay chain fitting with a Kalman filter. *Nucl. Instrum. Meth. A*, 552(3):566–575, 2005. Cited on page 73.